ABSTRACT

Investigation of Hadronic Resonances with STAR

Sevil Salur
Yale University
May 2006

Strongly interacting, high density matter is produced in heavy ion collisions at the Relativistic Heavy Ion Collider (RHIC). Hadronic resonances, due to their short lifetimes, can be used to investigate the freeze-out mechanisms after hadronization. The production of the strange baryonic resonance $\Sigma^*(1385)$ is investigated for the first time in heavy ion collisions and, through comparison with other resonances, the evolution of the fireball is investigated.

The data used for the analyses in this thesis were taken with the Solenoidal Tracker at RHIC (STAR) detector. Measurements of $\Sigma^*(1385)$, through the hadronic decay channel $\Sigma^*(1385)^{\pm} \rightarrow \Lambda + \pi^{\pm}$, in the 0-5% most central Au+Au and minimum bias p+p and d+Au collisions are presented. The invariant mass spectra of the $\Sigma^*(1385)$ are reconstructed using a combinatorial technique, and a mixed-event technique is applied to estimate the uncorrelated background. The corrected $\mathrm{p_T}$ spectra, inverse slope parameters, and yields of the $\Sigma(1385)^{\pm}$ and their antiparticles are measured and compared. The $\langle \mathrm{p_T} \rangle$ measurements of the $\Sigma^*(1385)$ is compared to those of other heavy particles to investigate effects of radial flow and particle production mechanisms. The $\Sigma^*(1385)$ $/\Lambda$ ratio, along with other resonance to stable particle ratios, suggests that a regeneration mechanism recovers signal loss due to re-scattering in the final state in Au+Au collisions. The nuclear modification factors, R_{dAu} and R_{AA} for $\Sigma^*(1385)$ are studied in comparison to those stable particles.

It has been hypothesized that pentaquarks, consisting of various combinations of five light u, d, and s quarks, may be produced in the high density collisions occurring at RHIC. Simulation studies and improved resonance identification techniques are used to search for pentaquarks.

Investigation of Hadronic Resonances with STAR

A Dissertation
Presented to the Faculty of the Graduate School
of
Yale University
in Candidacy for the Degree of
Doctor of Philosophy

By
Sevil Salur

Dissertation Director: Professor John Harris

May 2006

Acknowledgements

This research would not have been possible without the tireless efforts of the hundreds of physicists who built RHIC and STAR before I even became a part of this collective effort. That is why I have to start by thanking the whole STAR Collaboration and the RHIC community for allowing me this opportunity to do research in this extremely exciting time.

I would like to thank John Harris. Words cannot describe how grateful I am to him. Thank you for your tremendous support and for all the opportunities you have given me, including the ones to travel and present my research. I have to extend my heartfelt thanks to Helen Caines for all of her help, but especially for her patience. You never complained about my questions and were always helpful.

Valuable discussions with Ludovic Gaudichet, Patricia Fachini, Jingguo Ma, Christina Markert, An Tai, Haibin Zhang, and Zhangbu Xu helped me in my understanding of resonances. Christina also introduced me to resonances. If it weren't for her, the title of this thesis could have been different. I have to thank Paul Sorenson who showed me the basis of the mixed-event technique, which ended up being very essential for the analysis of resonances.

Thanks to Eric Hjort for patiently helping me with my embedding questions and for processing my requests so fast that I was able to show so many new results during the meetings. Discussions within the strangeness working group and our weekly phone meetings benefitted me a lot. I especially have to thank Olga Barannikova, Lee Barnby, Rene Bellwied, Gene Van Buren, Magali Estienne, Julien Faivre, Camelia Mironov, Sonia Kabana, Hui Long, Frank Simon and Jun Takashi.

Theoretical input from discussions with Jorg Aichelin, Steffen Bass, Johann Rafelski, Giorgio Torrieri and Spencer Wheaton was essential. Also thank you for making your easy to use codes available to us to help us further elucidate the implications of our data. I would like to also thank Walter Greiner for his encouragement.

I would like to thank my dissertation committee, John Harris, Helen Caines, Bonnie Flemming, Jack Sandweiss, and Witek Skiba, for reading my thesis and giving me valuable input and Rene Bellwied, for acting as the outside reader.

Within the Yale group – Stephen Baumgart, Betty Bezverkhny, the three JB's: Jana Bielcikova, Jaro Bielcik and Jakub Bielcik, Manuel Calderon, Oana Catu, Jon Gans, Mark Heinz, Boris Hippolyte, Matt Horsley, Anders Knospe, Matt Lamont, Brian Lasiuk, Mike Miller, Christine Nattrass, Nikolai Smirnov, Thomas Ullrich and Richard Witt – we really learned from each other especially when it came to problems related to C++ and Root. I would like to thank them also for their friendship and for making this such a pleasurable and healthy experience. (I literally mean healthy. Thanks Christine for your good food and for teaching me how to lift weights and to all the group members for sharing your good chocolate and sweets frequently with the rest of us.) I would like to thank also once more my officemate, Betty, for all the ups and downs that we shared together during this adventure.

There were surely so many others who affected my graduate school experience. I cannot pass without saying thanks to Aric, Dale, Grace, Gülhan, Qian, Mingchang, Veronica, Wei and Yong. We spent quite a long time together, tackling homework problems. Thanks again for your friendship. Eric, thank you for always running with me from one location to the other. Last but not least I would like to thank my parents and sisters, particulary Sema for being the role model that I admire most and for always being there for me whenever I need her.

Thank you so much!

Contents

List of Figures

List of Tables

Chapter 1

Introduction

Protons and neutrons that constitute atomic nuclei are themselves composed of fundamental particles called quarks and gluons (together called partons). In nature we can only observe quarks either as a quark and an anti-quark in a pair, or a triplet of quarks or anti-quarks. Table 1.1 presents the properties of quarks. Since quarks are confined inside hadrons, quark masses cannot be measured directly but instead they can be determined indirectly through their influence on hadronic properties.

The interaction of these particles can be described with four fundamental forces in nature: gravitational, weak, electromagnetic and strong in order of increasing strength. Each of these forces is mediated by the exchange of particles, i.e., gluons for the strong force. Quantum Chromodynamics (QCD) has been developed to describe the strong force interactions of quarks and gluons. An approximation of the potential

	Mass [GeV/c^2]	Q/e	S	C	B	T
u	$1-5\times10^{-3}$	2/3	0	0	0	0
d	$3-9\times10^{-3}$	-1/3	0	0	0	0
c	$1.15-1.35$	2/3	0	1	0	0
s	$75-170\times10^{-3}$	-1/3	-1	0	0	0
t	174 ± 5	2/3	0	0	0	1
b	$4-4.4$	-1/3	0	0	-1	0

Table 1.1: Properties of quarks in terms of their mass, charge (Q) in units of e, and strangeness (S), charm (C), bottom (B) and top (T) numbers.

between the two quarks is

$$V(r) = -\frac{4\alpha_s}{3r} + kr \tag{1.1}$$

with α_s the strong coupling constant, k another constant ($\sim$ 1 GeV/fm) and r the separation between the two quarks. On long distance scales the second term, and on short distances the first term, dominates the potential. This means that it is not possible to separate two quarks over a large distance scale, and thus the quarks are confined. However, since the small distance scale is governed by the term proportional to 1/r , deconfinement of quarks is possible if α_s approaches to a small value faster than r. The behavior of α_s approaching to a smaller value faster than r is called 'running', and thus α_s is a running coupling constant.

Partons behave almost as free particles when they are very close to each other. This surprising phenomenon, called 'asymptotic freedom', honored by a Nobel Prize awarded to David J. Gross, H. David Politzer, Frank Wilczek in 2004, has led to our current QCD theory describing interactions of particles. At very high densities and energies, asymptotic freedom leads to the predicted existence of a quark gluon plasma (QGP) phase of matter. The phenomenon expected to lead to a QGP in heavy ion collisions is the Debye Screening of the color charge at high partonic densities. This is analogous to the Debye Screening of an electric charge in QED. Compressed quark matter at high densities is predicted to produce a color conducting system of deconfined quarks and gluons referred to as the QGP phase. It is hoped that in heavy ion collisions at relativistic energies the deconfinement conditions can be reached due to the high energy densities produced in the collision region.

1.1 Heavy Ion Collisions

The liberation of quarks and gluons into a new phase of matter, the QGP, is predicted to occur in ultra-relativistic heavy ion collisions where the energy densities created are very large [1]. The Relativistic Heavy Ion Collider (RHIC) at Brookhaven National Laboratory, the first of its kind, is built to create and search for this novel form of matter by colliding Au ions at energies up to $\sqrt{s_{\mathrm{NN}}}$ = 200 GeV. Higher energies to probe shorter distances will be available at the Large Hadron Collider (LHC) at

CERN within a year or two.

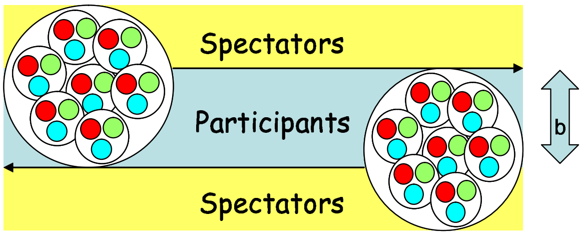

Figure 1.1: Schematic representation of nuclear collisions. During the most peripheral collisions, the number of participants is small and the impact parameter b is large. During a central collision the impact parameter b is small so that all nucleons participate in the collision.

A cartoon picture of two incoming nuclei consisting of nucleons and their constituent quarks (red, green, and blue) is presented in Figure 1.1. The geometry of the heavy ion collisions as, illustrated in the Figure 1.1, can be approximated by superposition of many nucleon-nucleon collisions. The number of participating nucleons is inversely related to the size of the impact parameter, b. The impact parameter is large for peripheral collisions, consisting of a small number of participants and a large number of spectators. A central collision occurs when the impact parameter b is small. Only central collisions of two heavy nuclei at high energies are expected to provide an environment sufficiently dense to produce a deconfined phase of nuclear matter.

The space-time evolution of a heavy ion collision is shown in Figure 1.2. Incoming heavy ion beams are represented as A and B. The first stage in this picture on both sides is when A and B beams collide to form a pre-hadronic phase. On the right side a heavy ion collision undergoes a QGP phase transition. As the system expands and cools due to internal pressures, a critical temperature (T_c) is reached and the hadronization starts. Hadronization continues until the chemical freeze out temperature (T_{ch}), when the distribution of particles amongst the various hadronic states is frozen and there are no inelastic flavor changing reactions. The expansion and cooling continues until elastic collisions between particles stop at the thermal freeze out temperature (T_{fo}), when the momenta of the particles are fixed. On the left side of the phase-space diagram, the hydrodynamic evolution of a heavy ion

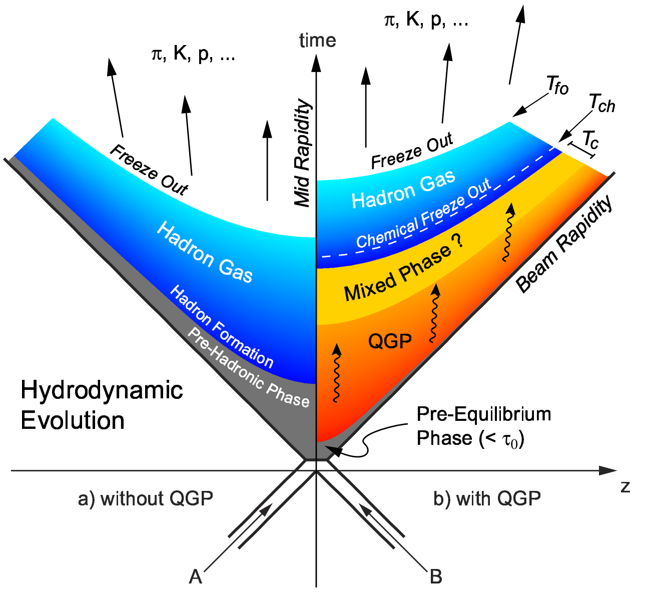

Figure 1.2: A lightcone diagram of a collision for a case (**a**) without a QGP and (**b**) with a QGP. $\mathrm{T_{fo}}$ is an abbreviation for thermal and $\mathrm{T_{ch}}$ for chemical freeze-out. Hadronization starts at $\mathrm{T_c}$, the critical temperature.

collision is presented without the QGP phase transition. It is predicted that the region between $\mathrm{T_{ch}}$ and $\mathrm{T_{fo}}$ should be accessible with the information from resonance measurements due to their very short lifetimes resulting from their strong decays. This thesis examines the production of the $\Sigma^*(1385)$ strange baryonic resonance in Au+Au heavy ion collisions in comparison to smaller systems, d+Au and p+p collisions, in order to investigate the evolution of the fireball in the region between $\mathrm{T_{ch}}$ and $\mathrm{T_{fo}}$.

The phase diagram [2] [3] of hadronic and partonic matter in terms of temperature (T) and baryo chemical potential (μ_B) is presented in Figure 1.3. The hatched region indicates the current expectation for the phase boundary based on lattice QCD calculations at $\mu_\mathrm{B} = 0$. The high temperature and low μ_B region is expected to be accessible with heavy ion collisions. Colliders with various energies (LHC, RHIC, SPS, AGS, and SIS) can reach different regions in this phase diagram as represented by the red circles. The QGP matter that can be created in the laboratory is believed to have existed in the first few micro-seconds after the Big Bang. The expected high temperature and minimum baryonic chemical potential of the 'Early universe' when

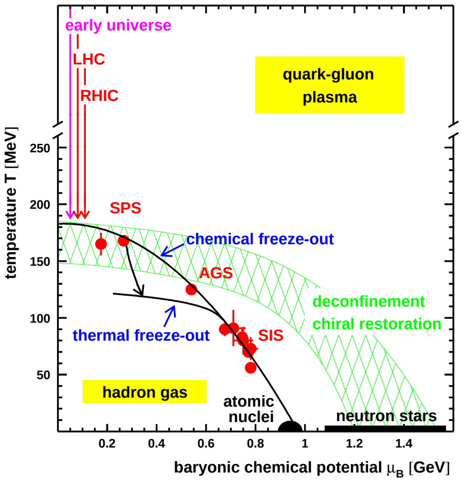

Figure 1.3: Phase diagram of hadronic and partonic matter. The hatched region indicates the current expectation for the phase boundary based on lattice QCD calculations at $\mu_{\mathrm{B}} = 0$. Figure is taken from [2].

QGP matter was created is shown in the phase diagram. The region near zero temperature and high μ_{B} is where the deconfined high-density phase is also predicted to exist (i.e. the interior of neutron stars).

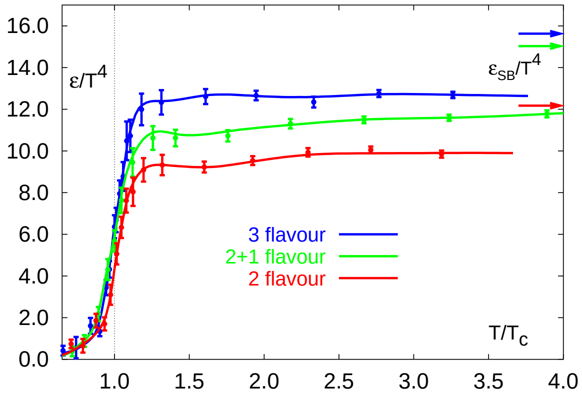

Figure 1.4: The energy density in QCD from lattice calculations as a function of $\mathrm{T}/\mathrm{T}_{\mathrm{c}}$. The number of degrees of freedom rises steeply for temperatures larger than T_{C}. Arrows indicate the ideal gas values of energy density for the three cases shown. Figure is taken from [4].

Numerical calculations of QCD on the lattice can be performed to check the dependence of temperature on the energy density of the system. In a quark gluon plasma phase due to the increase in the number of degrees of freedom, it is expected that there will be a change in the energy density. The dependence of the energy density, ϵ, divided by T^4 on $\mathrm{T}/\mathrm{T}_\mathrm{c}$ is presented in Figure 1.4. The number of degrees of freedom rises steeply for temperatures above T_c, corresponding to a transition in the system to a state where the quarks and gluons are deconfined, (i.e the number of degrees of freedom increases). T_c is predicted to be in the range of $150 - 190$ MeV.

1.2 Resonance Particles

Resonances are strongly decaying, extremely short lived particles. The lifetime of resonances is on the order of 10^{-23} seconds. Before decaying, these particles only travel about 10^{-15} meters. Since distances of this magnitude cannot be measured with current detectors, resonances are measured indirectly from their decay particles. Depending on the multiplicity of the events, identification of resonances can be quite challenging.

The first resonance particle, known as the pion-nucleon resonance, was found in 1952 by Anderson, Fermi and their collaborators at Chicago in pion-nucleon interactions [5]. At that time this observation was not recognized as a particle. Resonances first started to be identified as particles with the invention of the hydrogen bubble chamber several years later and the discovery of the Y^* particle, later known as the $\Sigma^*(1385)$, in 1960 by the Luis Alvarez group in Berkeley [6]. He was honored by a Nobel Prize in 1968 for his decisive contributions to elementary particle physics, but in particular his discovery of a large number of resonance states starting with the $\Sigma^*(1385)$ baryon.

The energy distributions of the two π mesons from the reaction $K^- + p \rightarrow \Lambda + \pi^+ + \pi^-$ was plotted as in Figure 1.5. It was expected that the distributions should be smooth if the cross sections were dominated by phase space alone. On the contrary, both the π^+ and the π^- distributions had peaks around 285 MeV, and this type of distribution was expected from a quasi-two-body reaction of the type

$$K^- + p \rightarrow Y^{*\pm} + \pi^{\mp}. \tag{1.2}$$

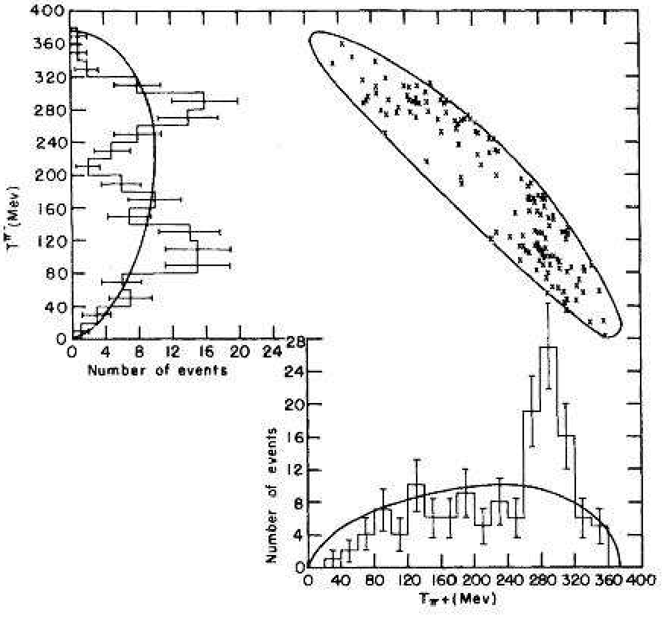

Figure 1.5: Energy distributions of the two π from the reaction $K^- + p \rightarrow \Lambda + \pi^+ + \pi^-$. Figure is taken from [6].

Resonances can be detected via the presence of a peak in the invariant mass spectrum of their decay particles. The invariant mass distribution of the Y^* state (both Y^{*+} and Y^{*-}), is plotted in Figure 1.6 [6]. The mass of the Y^* particle is observed to be at 1385 MeV. The discovery of the Y^* particle encouraged the exploration of many more resonances in the following years.

There are two possible ways to describe the resonance cross-section peaks. In one view, the peak is not related to a real particle but instead itself is the resonant state. In this picture, peaks are simply energies at which the cross section of a particle reaches a maximum. This is analogous to peaks associated with transitions between atomic energy levels. The second view is that the peaks are evidence for real particles that form as intermediate steps in the collision. The presence of resonance particles makes the collision of the incoming particles more likely by enhancing to the cross-section.

Both explanations, resonant states and resonance particles, have their advantages, and either can be used to find resonance properties. The energy at which the cross-section reaches a peak is the energy of resonances for the resonant state explanation.

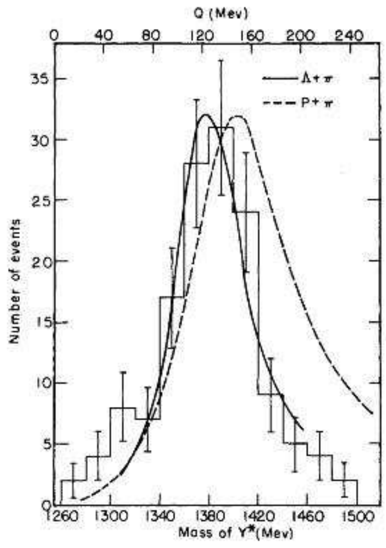

Figure 1.6: Invariant mass distribution for $\Sigma^*(1385)$ and fitted curves for $\pi\Lambda$ and πp. Q is the kinetic energy released. Figure is taken from [6].

In the particle explanation, the energy is the mass of an intermediate particle through which the reaction takes place. The particle is formed by the collision but almost instantly decays into more stable particles. The energy of the resonance is when the collision is most probable according to the resonant state explanation.

According to the uncertainty principle, $\Delta E \times \Delta t > h/2$, the mean lifetime is therefore given by $\tau = h/\Delta E$ with ΔE the width of the peak at the half maximum. If resonances are particles, then this formula gives their lifetimes. If they are resonant states, then the lifetime is the duration of the excited state, analogous to the time an electron stays in an excited atomic state.

1.3 Outline

This thesis discusses how studying strongly decaying resonances can increase our understanding of the evolution of the fireball created during the collisions. In Chapter 2 we will present the signatures predicted for the quark gluon plasma phase transition and in Chapter 3 the machinery that we use to investigate this transition. In Chapters

4 and 5, the analysis of the $\Sigma^*(1385)$ resonance and the simulations used to correct for the efficiency and acceptance are shown in detail for the p+p, d+Au and Au+Au collisions. The results of $\Sigma^*(1385)$ analyses are presented in Chapter 6. In Chapter 7 we discuss pentaquarks, what they are and how we search for them. The implications and further discussions are presented in Chapter 8.

Chapter 2

Quark Gluon Plasma Formation

The experimental signatures proposed for quark matter formation in relativistic heavy ion collisions can be grouped into two categories: bulk matter signatures and hard probes. The bulk matter signatures include the investigation of particle multiplicities, yields, momentum spectra and correlations of hadrons especially in the low momentum region ($p_T \leq 1.5$ GeV/c). It is also possible to produce energetic particles through hard scattering processes. The interaction of these highly energetic particles with the medium provide a unique set of penetrating probes of the medium, also known as hard probes.

The questions raised and analyzed in this thesis are concentrated on the bulk aspects of the matter. By investigating strange resonances in heavy ion collisions, we expect to find information about the evolution of the fireball. But before going into the details of the analyses, it is important to review some of the proposed signatures of the phase transition, especially those relevant for the analysis discussed in this thesis.

2.1 Resonance Production in Heavy Ion Collisions

During the expansion of the hot and dense matter (fireball) created in heavy ion collisions, chemical freeze-out is reached when the hadrons stop interacting inelastically. Elastic interactions continue until thermal freeze-out. Due to the very short lifetime ($\tau < \tau_{fireball} \sim$ 10 fm) of most resonances, a large fraction of their decays occur before the thermal freeze-out. Elastic interactions of resonance decay products with particles in the medium alters the momenta of these particles. This results in a loss of the signal reconstructed for resonances (due to re-scattering). However, secondary interactions (regeneration) can increase the resonance yield (such as $\Lambda + \pi \rightarrow \Sigma(1385)$). The detected resonance signals are therefore a product of both regenerated and primary produced but un-scattered resonances.

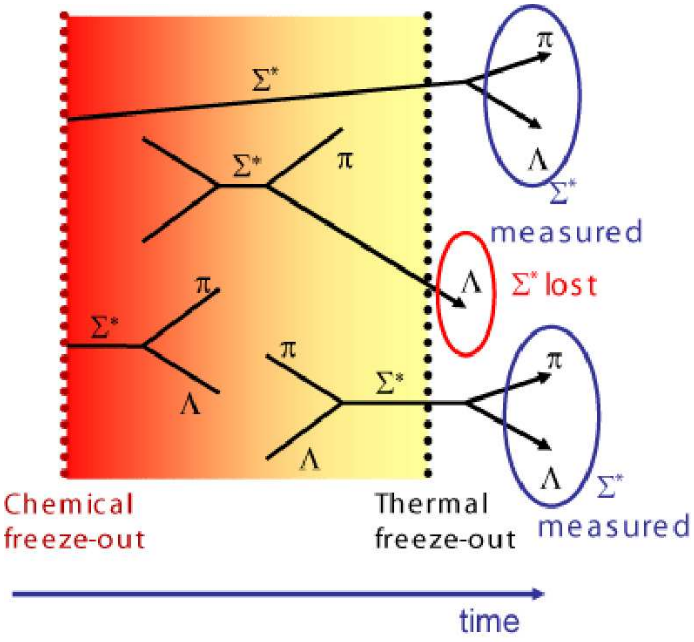

Figure 2.1: The re-scattering and regeneration effects on measured resonance yields during the time between chemical and thermal freeze-outs.

In Figure 2.1 a schematic representation of the $\Sigma^*(1385)$ re-scattering and regeneration between T_{ch} and T_{fo} is presented. The elastic interactions of decay products after T_{ch} and before T_{fo} with the surrounding particles result in a signal loss in the particle identification though this is offset by secondary interactions which increase the resonance yield (e.g., regeneration: $\Lambda + \pi \rightarrow \Sigma(1385)$; re-scattering: the decay products, π or Λ, are re-scattered in the medium therefore the $\Sigma^*(1385)$ is lost). The contribution of re-scattering and regeneration to the total observed yields depends on the time span between chemical and thermal freeze-out and the lifetime of each resonance [7, 8]. Resonances with higher transverse momenta are more likely to be reconstructed because of their larger relative lifetimes. They are more likely to decay outside of the medium and hence their daughter particles interact less with the medium. Both re-scattering and regeneration via possible pseudo-elastic interactions affect the measured total yields of resonances and may give rise to effects such as a change in the physical properties of the resonances such as width broadening and mass shift or change in $\mathrm{p_T}$ spectra. Thus the study of resonances provides an additional tool in the determination of the hadronic expansion time between chemical and thermal freeze-out by comparing resonance to stable particle ratios.

The resonances that are studied with the STAR experiment and their strangeness content, decay channel, branching ratio and widths are presented in Table 2.1. Mesonic $\rho^0(770)$ [9], $K^*(892)$ [10, 11] , $f_0(980)$ [12], and $\phi(1020)$ [13] and baryonic resonances $\Delta^{++}(1232)$ [14], $\Sigma^*(1385)$ $\Lambda(1520)$ [15, 16] and $\Xi^*(1530)$ [17] have been measured.

Table 2.1: Mesonic $\rho^0(770)$, $K^*(892)$, $f_0(980)$, and $\phi(1020)$ and baryonic resonances $\Delta^{++}(1232)$, $\Sigma^*(1385)$ $\Lambda(1520)$ and $\Xi^*(1530)$ that are measured in the STAR experiment.

Resonance	Strangeness	Decay Channel	Branching Ratio	Width [MeV/c^2]
$\rho^0(770)$	0	$\pi^-\pi^+$	100%	150
$K^*(892)$	±1	πK	100%	50.7
$f_0(980)$	0	$\pi^-\pi^+$	100%	40-100
$\phi(1020)$	0	K^-K^+	49.2%	4.46
$\Delta^{++}(1232)$	0	π^-p	100%	120
$\Sigma^*(1385)$	±1	$\pi\Lambda$	88.2%	36
$\Lambda(1520)$	±1	pK^-	22.5%	15.6
$\Xi^*(1530)$	±2	$\pi^+\Xi^-$	100%	9.1

2.2 Strangeness enhancement

Strangeness production was proposed as one of the possible signatures of a QGP phase by Rafelski and Muller more than 20 years ago [18]. They predicted that there would be an enhancement of strange particles in the presence of a QGP solely due to the lower thresholds of gluon fusion ($g + \bar{g} \rightarrow s + \bar{s}$) and annihilation of light $q\bar{q}$ pairs into $s\bar{s}$ pairs. In a QGP phase the threshold for s and $\bar{s}$ production is ∼ 300 MeV, which corresponds to the bare mass of two strange quarks. Since all the quantum numbers need to be conserved, in a hadronic interaction the threshold energy to produce strange particles is higher. For example Equation 2.1 requires 670 MeV and Equation 2.2 requires 986 MeV. The threshold energy of ∼ 300 MeV required to create a strange quark pair in a QGP phase is much smaller than that in hadronic interactions. This idea lies behind the proposed signature of enhancement of strangeness.

$$p + p \rightarrow p + \Lambda + K^{+} \tag{2.1}$$

$$p + p \rightarrow p + p + K^{-} + K^{+} \tag{2.2}$$

One very useful way of studying strangeness enhancement is the Wroblewski parameter, also known as the strangeness suppression factor [19]. This parameter is defined as the ratio of the numbers of strange quarks to light quarks,

$$\lambda_s = \frac{2\langle s\bar{s}\rangle}{\langle u\bar{u}\rangle\langle d\bar{d}\rangle}. \tag{2.3}$$

Since K mesons carry the majority of the produced strangeness, due to their smaller mass relative to other strange particles, the Wroblewski parameter can be measured reasonably well using the K/π ratio. For example it is measured to be $\lambda_s = 0.29 \pm 0.02 \pm 0.01$ from the $K^0_S/\pi^{\pm}$ ratio in $\sqrt{s} = 630$ GeV elementary $p + \bar{p}$ collisions by the UA1 Collaboration [20]. For comparisons with heavy ion systems, Figure 2.2-a shows the energy and system dependence of the K/π ratios at mid-rapidity. While triangles corresponds to heavy ion collisions, circles are from p+p collisions at the given energies [21, 22]. An enhancement in the K/π ratios of about 50% is observed at RHIC energies in central Au+Au collisions relative to elementary collisions extrapolated to similar energies. A similar magnitude of enhancement in K^-/π has already been observed at the lower energies of the AGS and SPS [23, 24].

The energy dependence of the Λ and $\overline{\Lambda}$ yields at mid-rapidity from Au+Au collisions at RHIC and Pb + Pb collisions at SPS as a function of $\sqrt{s_{NN}}$ is presented in

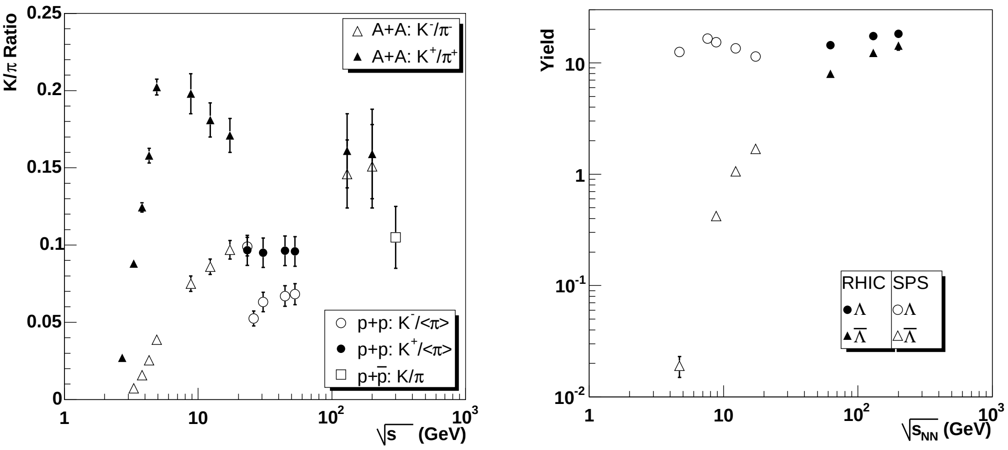

(a) (b)

Figure 2.2: (**a**) Mid-rapidity K/π ratios versus $\sqrt{s}$ and their dependence on heavy ion and p+p collisions. (**b**) The energy dependence of Λ and $\overline{\Lambda}$ yields.

Figure 2.2-b [25]. From SPS to RHIC energies, strange baryon production is approximately constant at mid-rapidity, whereas the $\overline{\Lambda}$ rises steeply, reaching 80% of the Λ yield at RHIC top energies. The other hyperons Ξ and Ω follow similar trends. Since most of the strange baryons produced also include light up and down quarks, at low energies, strange baryon production is dominated by valance quark transport from the colliding system, but at RHIC it is dominated by pair production. This also implies that at RHIC energies most of the incoming baryons continue moving towards the higher rapidity regions therefore they do not cause any increase in the baryon number in the mid-rapidity regions.

2.3 Hard processes and jet quenching

It is predicted that high momentum partons lose energy by induced gluon radiation when they pass through dense matter such as QGP [26]. This phenomenon called jet quenching, can be studied with the measurements of nuclear modification factors. A nuclear modification factor is the scaled ratio of particle yields in heavy ion collisions relative to the particle yields in p+p collisions, R_{AA}. It is called R_{CP} when the numerator of the ratio is for central collisions and the denominator is for peripheral collisions. The nuclear modification factor is formulated as

$$R_{AA}(\mathrm{p_T}) = \frac{d^2N_{AA}/d\mathrm{p_T}d\eta}{T_{AA}d^2N_{pp}/d\mathrm{p_T}d\eta} \tag{2.4}$$

The scaling factor, $T_{AA} = \langle N_{Binary}\rangle/\sigma^{NN}_{inel}$, is calculated using the Glauber Model [27]. In this model, the interactions of nuclei can be approximated as a superposition of individual nucleon-nucleon interactions with the assumption that each nucleon follows a straight line trajectory with a known nucleon-nucleon cross section. R_{AA} is expected to be unity if there are no nuclear affects.

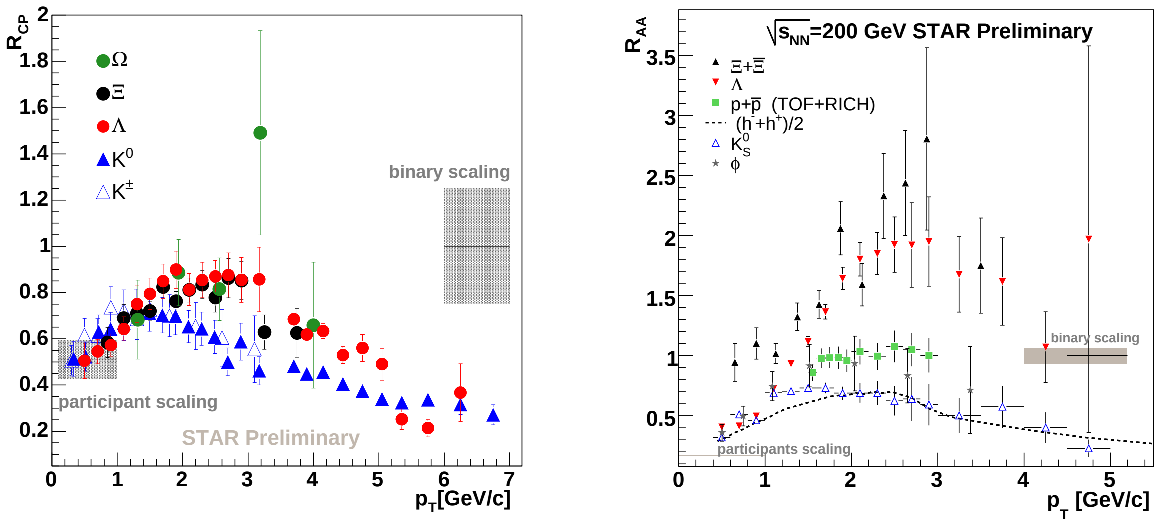

(a) **(b)**

Figure 2.3: Nuclear Modification factors from **(a)** the ratio of 0-5% and 40-60% Au+Au collisions and **(b)** the ratio of the 0-5% most central Au+Au and scaled minimum bias p+p collisions.

Figure 2.3-a shows the measured nuclear modification factor of strange particles with the STAR experiment at $\sqrt{s_{\mathrm{NN}}}$ = 200 GeV. At higher $\mathrm{p_T}$, the ratios exhibit a suppression from binary scaling, attributed to fast moving partons losing energy as they traverse a dense medium. The suppression for Λ and K^0_S particles are distinctly different. Whether this difference is a baryon-meson effect, particle species specific

or due to their masses is still undetermined. The measurement of resonance particles with different masses but with the same quark content as their stable particles can distinguish if this is a mass effect or a species effect.

The nuclear modification factors for Ξ, Λ, p, K_S^0, ϕ and charged hadrons from the 0-5% most central Au+Au collisions are presented in Figure 2.3-b. While the R_{AA} for mesons ($\mathrm{h}^+ + \mathrm{h}^-$, $\mathrm{K_S^0}$, ϕ) is similar to their R_{CP} values, R_{AA} of strange baryons shows significant differences (i.e. no suppression). Instead, there is an enhancement and ordering with strangeness content: the higher the strangeness content, the higher the R_{AA} measurement in the intermediate $\mathrm{p_T}$ region. The difference between yields in p+p and peripheral Au+Au may be explained by phase space (canonical) suppression in the p+p collisions [28].

2.4 Particle Spectra and Ratios

Since we cannot directly measure the initial short-lived source in heavy ion collisions, we attempt to gain information about the evolving conditions through the temperature, by studying the momentum spectra of various particles. The number of particles produced are measured per unit rapidity for each $\mathrm{p_T}$ range. Simple functions such as exponential, power law, or Boltzman are used to describe the distributions of these transverse momentum spectra allowing integration of the yields, dN/dy, by extrapolating over all $\mathrm{p_T}$. The accuracy of extrapolation and choice of function play an essential role in determination of the integrated yields.

2.4.1 Exponential Distribution

The particle production is expected to follow an exponential distribution as predicted by Hagedorn in the early 1960's [29]. For a thermally equilibrated particle distribution, the $\mathrm{p_T}$ spectrum can be described by

$$\frac{\mathrm{d^2N}}{2\pi \mathrm{p_T dy dp_T}} = \mathrm{A e}^{-\frac{\mathrm{m_T}}{\mathrm{T}}} \tag{2.5}$$

where the transverse mass $\mathrm{m_T}$ is defined as $\mathrm{m_T} = \sqrt{\mathrm{p_T}^2 + \mathrm{m_0}}$. The left side of Equation 2.5 can be re-written as,

$$\frac{\mathrm{d}^2\mathrm{N}}{2\pi \mathrm{p_T}\mathrm{dy}\mathrm{dp_T}} = \frac{\mathrm{d}^2\mathrm{N}}{2\pi \mathrm{m_T}\mathrm{dy}\mathrm{dm_T}}. \tag{2.6}$$

If we substitute Equation 2.6 into Equation 2.5 and integrate over $\mathrm{m_T}$

$$\int_{\mathrm{m_0}}^{\infty} \frac{\mathrm{d}^2\mathrm{N}}{2\pi \mathrm{m_T}\mathrm{dy}\mathrm{dm_T}} \mathrm{dm_T} = \int_{\mathrm{m0}}^{\infty} \mathrm{A} \mathrm{e}^{-\frac{\mathrm{m_T}}{\mathrm{T}}} \mathrm{dm_T} \tag{2.7}$$

We obtain Equation 2.7 which can be re-arranged so that the multiplicative constant A can be evaluated directly,

$$\mathrm{A} = \frac{\mathrm{dN/dy}}{\int_{\mathrm{m_0}}^{\infty} 2\pi \mathrm{e}^{-\frac{\mathrm{m_T}}{\mathrm{T}}} \mathrm{m_T}\mathrm{dm_T}} = \frac{\mathrm{dN/dy}}{2\pi \mathrm{T}(m_0 + \mathrm{T})\mathrm{e}^{-\frac{m_0}{\mathrm{T}}}}. \tag{2.8}$$

We can substitute Equation 2.8 into Equation 2.5 and get the following with only the two variables dN/dy and T,

$$\frac{\mathrm{d}^2\mathrm{N}}{2\pi \mathrm{m_T}\mathrm{dy}\mathrm{dm_T}} = \frac{\mathrm{dN/dy}}{2\pi \mathrm{T}(m_0 + \mathrm{T})} \mathrm{e}^{-\frac{(\mathrm{m_T} - m_0)}{\mathrm{T}}}. \tag{2.9}$$

Equation 2.9 is used to describe the $\mathrm{p_T}$ spectra of the particles that are measured. The temperature parameter T, more commonly referred to as the inverse slope parameter, was initially expected to be directly related to the freeze-out temperature. However with the presence of transverse flow in the system, T is blue shifted as

$$\mathrm{T_{eff}} = \mathrm{T}\sqrt{\frac{1+\beta_\mathrm{r}}{1-\beta_\mathrm{r}}} \tag{2.10}$$

where β_r is the transverse expansion velocity.

2.4.2 Thermal Models

Assuming QGP formation in the initial state in heavy ion collisions it is expected that the thermal nature of the partonic medium could be preserved during hadronization [30]. The particle yields measured in the final state then resemble a thermal equilibrium population. Thermal models are used to predict the equilibrium properties of a macroscopic system from the measured yields of the constituent particles. It is commonly agreed that light (u and d) quarks are more likely to reach equilibrium in the hadron gas than the strange quarks due to the relatively larger strange quark mass ($m_s \sim T_c$). The strangeness suppression factor, γ_s, is introduced to account the amount of strangeness chemical equilibrium [31].

With the given ratios of particles it is possible to deduce the temperature T, the volume V, the baryonic chemical potential $\mu_{\rm B}$, strangeness chemical potential $\mu_{\rm S}$ and charge chemical potential $\mu_{\rm Q}$ [30, 32, 33]. Chemical potentials require that the variables are conserved on the average in the whole system for a Grand Canonical (GC) ensemble. The partition function, Z(T,V) is,

$$Z^{GC}(T, V, \mu_Q) = Tr[\exp(-\frac{1}{T}(H - \sum_i \mu_{Q_i} Q_i))], \tag{2.11}$$

where H is the Hamiltonian and Q_i are the conserved charges. The choice of the Hamiltonian varies but is usually taken to describe a hadron gas so that the partition function contains all relevant degrees of freedom of the strongly interacting medium. For the charge, baryon number and strangeness conserving partition function, Equation 2.11 can be written as a sum of partition functions $\ln Z_i$ of all hadrons and resonances

$$\ln Z(T, V, \overrightarrow{\mu}) = \sum_i \ln Z_i(T, V, \overrightarrow{\mu}) = \sum_i \frac{V g_i}{2\pi^2} \int_0^\infty \pm p^2 dp \ln[1 \pm \lambda_i \exp(-\frac{\epsilon_i}{T})], \tag{2.12}$$

for $\epsilon = \sqrt{p^2 + m_i^2}$, $\overrightarrow{\mu} = (\mu_B, \mu_S, \mu_Q)$, and g_i is the spin-isospin degeneracy factor. Fugacity is defined to introduce further approximations as

$$\lambda_i(T, \overrightarrow{\mu}) = \exp(\frac{B_i \mu_B + S_i \mu_S + Q_i \mu_Q}{T}). \tag{2.13}$$

The fugacity of a hadron is defined by the product of its valance quark fugacities (e.g., $\lambda_\pi = \lambda_u \lambda_d$, $\lambda_n = \lambda_u \lambda_d^2$ and $\lambda_\Lambda = \lambda_u \lambda_d \lambda_s$).

After expanding the logarithm and performing the integration, the right hand side of Equation 2.12 is

$$\ln Z_i(T, V, \overrightarrow{\mu}) = \frac{V T g_i}{2\pi^2} \sum_{k=1}^{\infty} \frac{(\pm 1)^{k+1}}{k^2} \lambda_i^k m_i^2 K_2(\frac{k m_i}{T}) \tag{2.14}$$

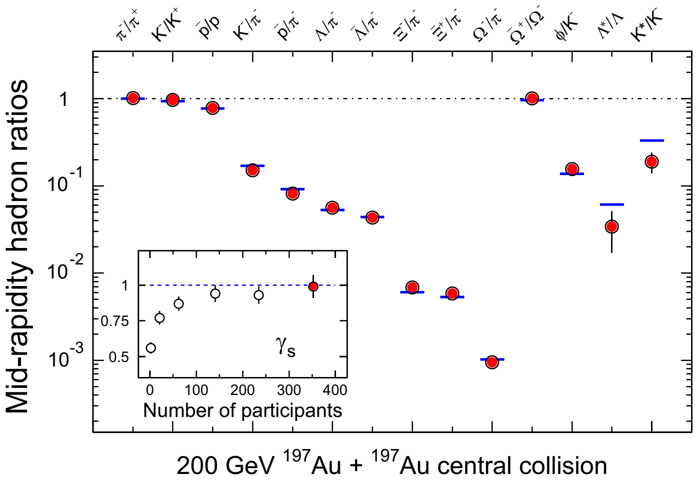

Figure 2.4: Ratios of $\mathrm{p_T}$ integrated mid-rapidity yields for different hadron species in STAR for central Au+Au collisions at $\sqrt{s_{\mathrm{NN}}} = 200$ GeV. The horizontal bars represent statistical model fits to the measured yield ratios for stable and long-lived hadrons. The fit parameters are T $= 163 \pm 4$ MeV, $\mu_B = 24 \pm 4$ MeV and $\gamma_s = 0.99 \pm 0.07$. The variation of γ_s with centrality is shown in the inset. Figure is taken from [34].

for K_2 the modified Bessel function. Following Equation 2.14, the density of the i^{th} particle can be written as

$$\ln n_i(T, \overrightarrow{\mu}) = \frac{\langle N_i \rangle}{V} = \frac{T g_i}{2\pi^2} \sum_{k=1}^{\infty} \frac{(\pm 1)^{k+1}}{k^2} \lambda_i^k m_i^2 K_2(\frac{k m_i}{T}). \tag{2.15}$$

The predicting power of statistical models for T, μ_B, μ_S, and γ_S require utilization of measured particle ratios. Within the ratios all degeneracy factors of the fireball in Equation 2.15 cancel, leaving just the relative fugacities. Some examples are given in Equation 2.16 and Equation 2.17,

$$\frac{\bar{p}}{p} = \lambda_u^{-4} \lambda_d^{-2} = \exp(-(\frac{4\mu_u + 2\mu_d}{T})), \tag{2.16}$$

$$\frac{\Lambda}{p} = \lambda_s \lambda_u^{-1} = \exp(\frac{\mu_s - \mu_u}{T}). \tag{2.17}$$

Figure 2.4 shows a comparison of integrated hadron yield ratios for central Au+Au collisions to statistical model fits. The horizontal bars represent statistical model fits to the measured yield ratios for stable and long-lived hadrons under the assumption that the system is in thermal and chemical equilibrium at that stage. While the fit provides a good agreement with the ratios measured for the stable and long-lived hadrons, deviations are observed for short-lived resonances. The variation of γ_s with centrality is shown in the inset. The strangeness suppression factor, γ_s, reaches 1 in the most central collisions implying equilibrated strangeness production in the most central collisions but not in the peripheral collisions.

Chapter 3

Experimental Facilities

3.1 Introduction

The experiments are done at the Relativistic Heavy Ion Collider (RHIC) at Brookhaven National Laboratory (BNL), located on Long Island in New York. RHIC is capable of colliding beams of both the same and different species of ions, ranging from protons to Au ions, at energies ranging from a minimum center of mass energy of 19 GeV per nucleon to a maximum center of mass energy of 200 GeV for Au+Au and 500 GeV for p+p per nucleon. The main reason for building RHIC was to produce and investigate the properties of a hot and dense phase of matter of quarks and gluons. At RHIC it is also possible to collide polarized protons in order to investigate the spin structure of hadrons, test QCD predictions and perform polarization searches for interactions beyond the Standard Model. The first Au+Au collisions at $\sqrt{s_{\rm NN}}$=130 GeV energy started in the summer of 2000, following 10 years of development and construction. To date, RHIC has been run in various configurations of p+p, Cu+Cu, d+Au, and Au+Au at energies ranging from $\sqrt{\rm s_{NN}}$ =19 to 200 GeV. There are a total of six interaction points at RHIC with four dedicated experiments, BRAHMS[1], PHOBOS[2], PHENIX[3], and STAR[4] . In this chapter we describe the RHIC experimental facility

---

[1] Broad Range Hadron Magnetic Spectrometers Experiment at RHIC

[2] Modular Array for RHIC Spectra (MARS)

[3] Pioneering High Energy Nuclear Experiment

[4] Solenoidal Tracker At RHIC

and the STAR detector, where these thesis data were collected.

3.2 RHIC

The RHIC experimental facility consists of a complex set of accelerators and beam transfer lines. A schematic diagram of RHIC and its components is shown in Figure 3.1. The subsystems of RHIC are a Tandem Van de Graaff facility, a proton linear accelerator (LINAC), the Booster synchrotron, the Alternating Gradient Synchrotron (AGS), and the RHIC synchrotron rings.

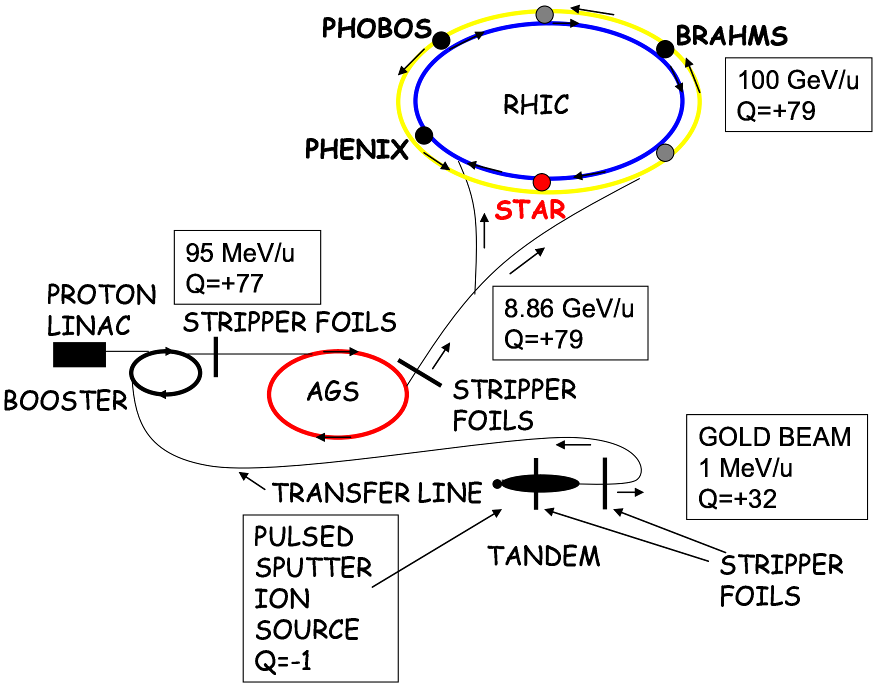

Figure 3.1: A schematic diagram of the RHIC accelerator facility at BNL. The locations of the four experiments BRAHMS, PHOBOS, PHENIX, and STAR are also presented. See text for details.

There are 6 locations where the two quasi-circular concentric rings with super conducting magnets (yellow for counter-clockwise beams and blue for clockwise beams) intersect along their 3.8 km circumference. Each ring has six arc sections and six interaction regions with an interaction point at the center. RHIC performs not only as an accelerator but also as a storage ring and a collider for a variety of ion species. The magnets are essential in performing these three duties. There are dipole, quadrupole and sextupole magnets which are cooled to a temperature of < 4.6 K by supercritical helium, for bending and focusing the ion beams. A pair of dipole magnets, DX and D0, located at 10 m and at 23 m from the collision point, respectively, steer beams for head-on collisions.

Figure 3.1 shows also the operational steps necessary in accelerating the heavy ions. The Tandem Van de Graaff Facility, which consists of two Tandems, is used to initially accelerate the Au ions starting from a Cesium sputter ion source. The ions leave the Tandem with 1 MeV/u energy after 13 of their electrons are removed with a carbon stripper foil. Another stripper just after the Tandem removes 20 more electrons and the beam is transported from Tandem to the Booster for further acceleration via the Transfer Line as shown schematically in Figure 3.1. Ions are transferred to the AGS after being accelerated to 95 MeV/u in the Booster. The Au ions are injected into RHIC after they are fully ionized and reach energies of 8.86 GeV/u in the AGS. The final acceleration up to 100 GeV/u for Au ions is achieved at RHIC in about 2 minutes from injection to top energies provided by the 28 MHz RF system. After reaching the operating beam energy the bunches are transferred to the storage RF (197 MHz) system. The beams in the blue and yellow rings are 'steered' so that bunches cross each other in the same place, and 'cogged' so that they cross at the same time. They are also 'tuned' to make the cross sectional area of the beam narrower.

3.3 The STAR Experiment

The Soleniodal Tracker at RHIC (STAR) is one of the four detector systems at RHIC. STAR was built to create strongly interacting matter under extreme conditions and to search for signatures of quark gluon plasma formation. The STAR detector system is designed to measure multiple observables simultaneously in the high track multiplicity collision environments at RHIC and to investigate both perturbative and non-perturbative aspects of the nuclear collision system. In order to achieve these goals, STAR was constructed to measure hadron production over a large solid angle with a large acceptance. A cut-away view of the STAR detector system is shown in Figure 3.2. Starting from the beam pipe, the main components of the STAR detector in its current configuration are a Silicon Vertex Tracker (SVT), one layer of Silicon Strip Detector (SSD), a large volume Time Projection Chamber (TPC), two radial-drift TPCs (FTPCs), and a barrel and end-cap Electromagnetic Calorimeter (BEMC and EEMC). The SVT consists of three concentric cylindrical barrels of ladders comprised of wafers and SSD performs as the fourth layer of the SVT. Both detectors, covering a pseudo-rapidity range $|\eta| \leq 1$ are used to increase the point charge resolution of the tracks to improve the primary and secondary vertexing. The TPC, with a pseudo-rapidity coverage $|\eta| \leq 1.8$, and two FTPCs, which extend the pseudo-rapidity coverage to $2.5 < |\eta| < 4$, are used to track charged particles and identify them at low momenta (p < 1 GeV/c). The BEMC and EEMC cover a pseudo-rapidity range $|\eta| < 1$ and $1 < \eta < 2$ respectively, and they measure the energy deposited by high transverse momentum photons and electrons.

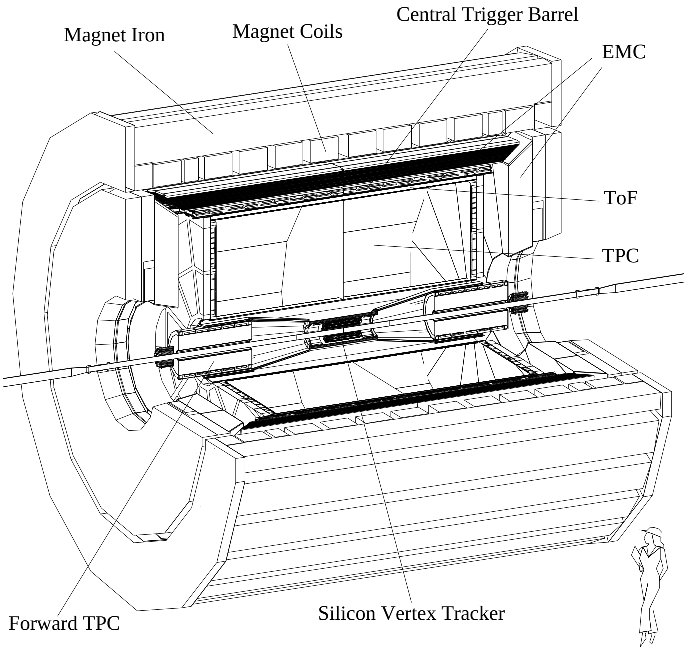

Figure 3.2: Cut-away view of the STAR detector.

Figure 3.3 shows the reconstructed momentum versus rapidity of particles from the collisions of p+p in the TPC and FTPC. All these detectors have complete azimuthal symmetry ($\Delta\phi = 2\pi$) and are embedded in a 0.5 T solenoidal magnet at room temperature, with a field parallel to the beam pipe. During the first three years of operation, there was also a ring imaging cherenkov detector (RICH) with a small coverage $|\eta| < 0.3$ and $\Delta\phi = 0.11\pi$ to extend the particle identification to higher momenta.

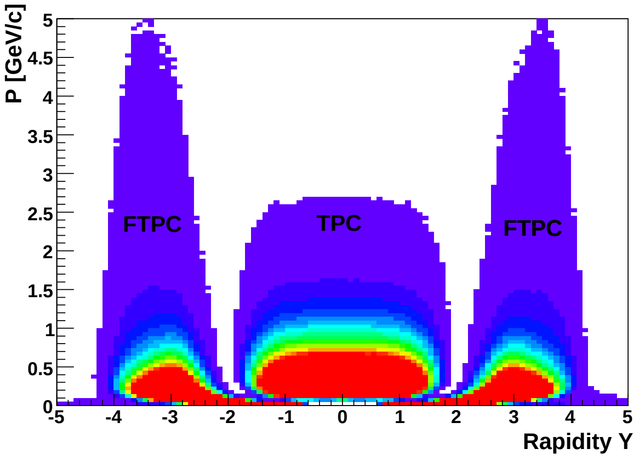

Figure 3.3: Momentum vs rapidity of the particles from Year 2 p+p events in the TPC and FTPCs. The TPC pseudo-rapidity coverage is $|\eta| \leq 1.8$. The two FTPCs cover the pseudo-rapidity range $2.5 < |\eta| < 4$.

In addition to tracking and particle identification detectors, there are also trigger detectors that are used to select events depending on the topology of the collisions. There are three main trigger detectors: the Zero Degree Calorimeter (ZDC), Central Trigger Barrel (CTB) and Beam-beam Counters (BBC). Different combinations of these trigger detectors are used depending on which ions are collided. The STAR trigger detectors for Au+Au collisions consist of the two ZDCs located $\sim$ 17 m up and down-stream of the nominal interaction point and the CTB surrounding the TPC. A minimum bias trigger for Au+Au collisions is defined by the coincident measurement of spectator neutrons in both ZDCs. The CTB, an array of scintillator slats, is used to detect event multiplicity and to trigger on the 10% most central Au+Au collisions. For p+p collisions, a minimum bias trigger is defined by coincidences in the two BBCs, which are scintillator detectors positioned around the beam pipe approximately 2 m from the center of the TPC covering $3.3 < |\eta| < 5$. Centrality tagging in d+Au collisions is based on the charged particle multiplicity in $-3.8 < \eta < -2.8$, measured by the FTPC, in the Au beam direction.

3.3.1 STAR Magnet

One of the fundamental requirements to enable a detailed study of heavy ion collisions is the tracking of particles. The STAR magnet, providing a magnetic field parallel to the beam direction, is used for particle tracking and momentum determination. The charge of the particles and the momentum of these charged particles can be measured via their helical trajectories in the magnetic field. In order to determine the momentum (p) of the particle, we measure the radius of curvature (r) of its trajectory using the Lorentz Force Law

$$\mathrm{F_{Magnetic}} = \mathrm{q}(\overrightarrow{v} \times \overrightarrow{B}) = \mathrm{qvB} \tag{3.1}$$

where v is the velocity of the particle and B the magnetic field. The magnetic force will be equal to

$$\mathrm{F} = \mathrm{m}\frac{\mathrm{v}^2}{\mathrm{r}}. \tag{3.2}$$

For a particle of mass m, we use Newton's 2nd Law, and the Equation 3.1, and Equation 3.2 to extract the momentum p of the particle.

$$\mathrm{F_{Centrifigual}} = \mathrm{F_{Magnetic}} \tag{3.3}$$

$$\mathrm{qvB} = \mathrm{m}\frac{\mathrm{v}^2}{\mathrm{r}}$$

$$\mathrm{qBr} = \mathrm{mv} = \mathrm{p}$$

After extracting the momentum with the assumption that the charge of the particle is ±1, it is possible to identify different particles with further detector information (i.e. particle identification with dE/dx and magnetic field information. See next section).

A large solenoidal magnet surrounds the STAR detectors. Due to the high multiplicities and large momentum range of tracks produced in heavy ion collisions at RHIC, the magnet was designed carefully. The homogeneity to minimize the distortions in the drift of electrons, high kinematic acceptance for low p_T and good momentum resolution for high p_T particles were main considerations of the magnet design. The STAR magnet is cylindrical, as can be seen in the photograph presented in Figure 3.4-a, with inner and outer diameters 5.27 m and 7.32 m, respectively, and a length of 6.85 m. A drawing of the cross-section of the STAR magnet is presented in Figure 3.4-b. The main components of the magnet are the 30 flux return bars (backlegs), four end-rings, and two poletips with a total weight of 1100 tons, resting on two 36 ton cradles. The flux return bars form the outer wall of the cylinder which encloses the main and space trim coils. The poletip also includes a trim coil to keep the magnetic field uniform. The maximum magnetic field along the length of the beamline is 0.5 Tesla when the current through the main and space trim coils is 4500 A. The magnet coils operate at a mean temperature of 29 C. There is a water cooling system to maintain the required temperature by removing the excess heat.

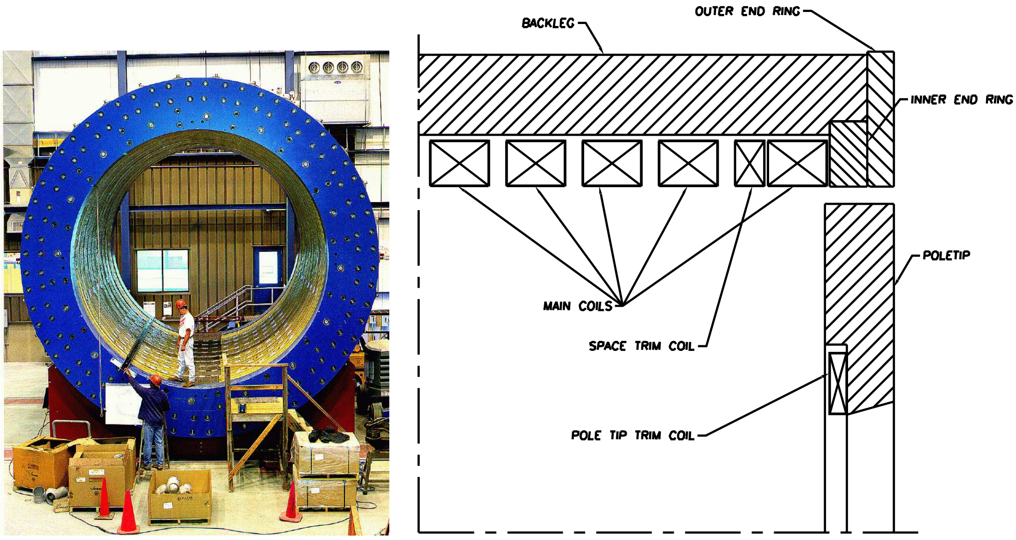

(a) **(b)**

Figure 3.4: (**a**) A picture of the STAR magnet before the TPC was installed. (**b**) Sideview quarter-section drawing of magnet steel and coil locations.

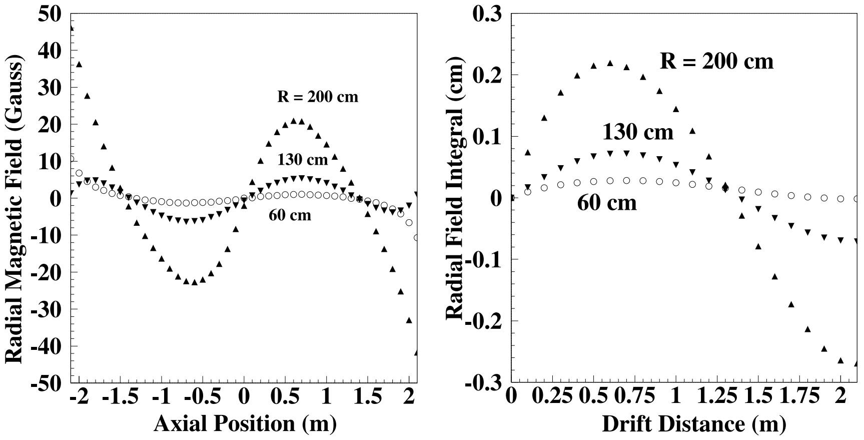

(a) (b)

Figure 3.5: (**a**) Measurements of the radial component of the STAR magnetic field (Gauss) as a function of axial (z) position for three radii at $\phi = 0°$. The center of the TPC and the magnet are at $z = 0$. The inner and outer radii of the TPC are 50 and 200 cm, respectively. (**b**) Values of the field integral ($\Im_r$) of the STAR magnetic field (cm) as a function of drift distance (z). Representative data are given at three radii in the TPC for $\phi = 0°$ and $z < 0$ (TPC East Half). Figures are taken from [35].

During the first year's run and later for track quality checks the magnet was run at half field (0.25 Tesla). Similarly, the polarity is also switched occasionally to study further systematics of the tracking. The magnetic field is mapped for all three components $\mathrm{B_r}$, B_ϕ, $\mathrm{B_z}$ with an apparatus, available from CERN, consisting of a steerable array of Hall probes. Field maps were taken for the magnet at both full-field and half-field. In Figure 3.5-a the measurements of the radial component of the STAR magnetic field (Gauss) as a function of axial (z) position for three radii at $\phi = 0°$ are presented. The maximum value for the radial component is 50 Gauss for full-field and 25 Gauss for half-field. The ϕ component of the field is ±3 Gauss maximum for full-field and ±1.5 Gauss for half-field. These deviations are orders of magnitude smaller than the operational (0.5 Tesla) magnetic field and factor of 2 better than the specifications and in agreement with the design calculations. The corresponding field integrals ($\Im_r$) of the same three field measurements with respect to the drift distance are plotted in Figure 3.5-b. There are angular variations of the radial field but the values are less than 0.30 cm for $|\Im_r|$ and 0.035 cm for $|\Im_\phi|$.[6]

3.3.2 The STAR TPC

Heavy ion collisions at RHIC energies can result in very dense systems ($\sim$ 6000 particles). In order to have enough accuracy to separate tracks produced in these dense environments, the size of the detectors can be quite large. The Time Projection Chamber, with its large volume, is the main detector in STAR and is used to track charged particles. A schematic picture of the large acceptance STAR TPC is shown in Figure 3.6. The TPC, with a length of 4.2 m, an inner radius of 0.5 m and an outer radius of 2 m, is cylindrical in design and is concentric with the beam line (z axis). Due to its cylindrical shape, the TPC covers the full azimuthal angular range ($0 \leq \phi \leq 2\pi$). As can be seen schematically in Figure 3.6, the TPC covers geometrically a range $-2 \leq \eta \leq 2$ in pseudo-rapidity defined by its inner radius. Due

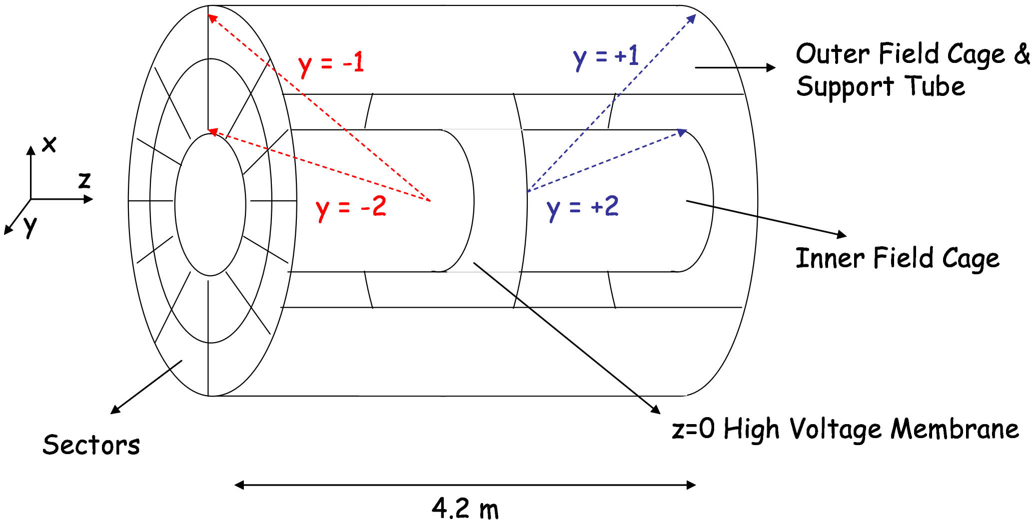

Figure 3.6: Cut-away view of the STAR Time Projection Chamber. TPC's diameter is 4 m and its length is 4.2 m. The high voltage membrane is located at $z = 0$. There are 12 pairs of inner and outer sectors of pads on each end for reading out the TPC. The red and blue lines are the schematic view of the tracks illustrating the pseudo-rapidity in the TPC.

---

[6] The field integrals are $|\Im_r| = |\int \frac{B_r}{B_z} dz|$ and $|\Im_\phi| = |\int \frac{B_\phi}{B_z} dz|$.

to a minimum number of hits required for adequate tracking, the effective tracking volume is reduced to $|\eta| \lesssim 1.5$. The TPC volume is divided at its center along the beam direction by a high voltage cathode membrane as shown in Figure 3.6. The

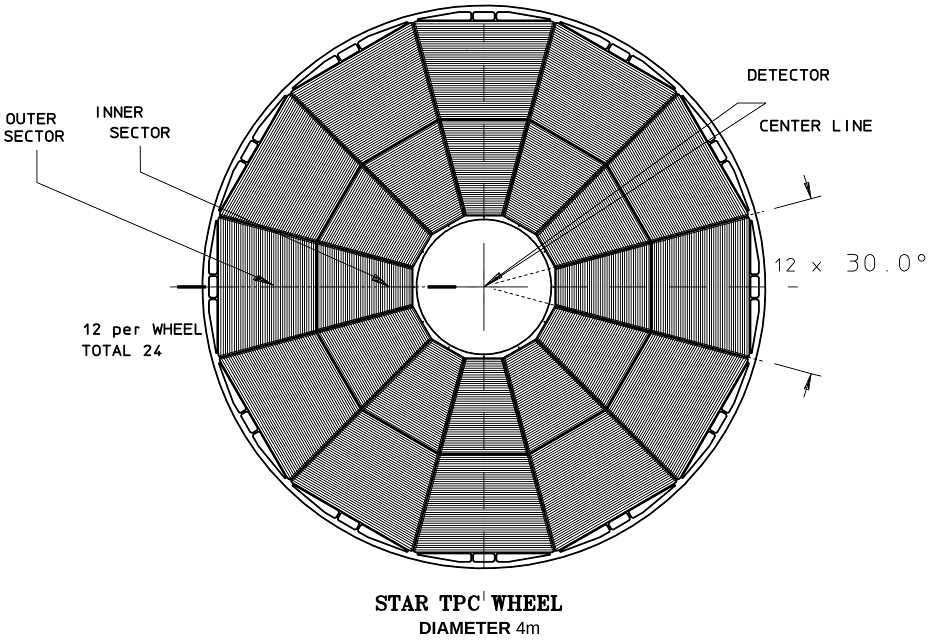

Figure 3.7: End view of the STAR TPC. 12 sectors cover the full azimuthal range, inner and outer sectors can be seen.

outer field cage consists of wide concentric field cage cylinders that provide a series of equipotential rings to divide the voltage evenly. The grounded end caps (0 V), the central membrane at 31 kV and equipotential rings of the outer field cage provide the necessary uniform electric field. The TPC is filled with P10 gas which is a mixture of 90% Argon and 10% Methane. The gas is chosen to minimize the attenuation of the drifting electrons and to provide a drift velocity ~ 5.4 cm/μs. Air which includes H_2O and O_2 influences the drift velocity. That is why the TPC is pressurized at 2 mbar above atmospheric pressure to minimize leakage of air from the outside to inside. Electrons are liberated when charged particles traverse and ionize the P10 gas. These electrons drift in the electric field towards the nearest end cap, where the signals are read out. The readout planes, Multi-Wire Proportional Chamber (MWPC) with pad readout, are modular units mounted on aluminium support wheels. An end view of the STAR TPC is illustrated in Figure 3.7. The beam is perpendicular to the page and goes through the center of the TPC. The read out is divided into 24 sectors, 12 at each end, and each sector divided into inner and outer subsectors.

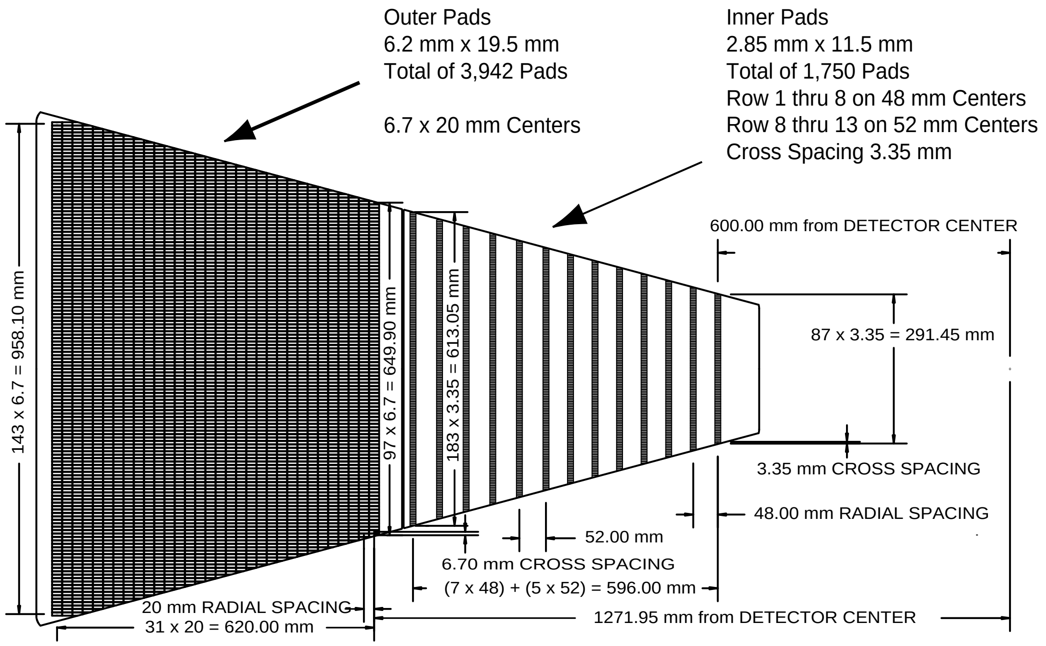

Figure 3.8: Detailed view of a single sector of the TPC showing inner and outer sub-sectors. The inner sub-sector is on the right and it has small pads arranged in widely spaced rows. The outer sub-sector is on the left and is densely packed with larger pads. Figure is taken from [36].

As shown in Figure 3.8, the inner sector consists of 13 pad rows with a total 1750 small pads (2.85 mm × 11.5 mm) and the outer sector has 32 pad rows with 3940 larger pads (6.20 mm × 19.5 mm) respectively. The inner sector has small pads, due to the high track density, arranged in widely spaced rows to extend the position measurements along the track to small radii thus improving the momentum resolution. The outer sector has densely packed (i.e. no space between pad rows) larger pads to optimize the dE/dx resolution. With larger pads in the outer sector the full track ionization signal is collected and more ionization electrons improve statistics on the dE/dx resolution.

As shown in Figure 3.9, the readout MWPC have 3 wire planes: a gating grid, ground plane, and anode wires. The drifting electrons are amplified by a grid of wires on each end of the TPC and the signals are measured with small pads behind the anode wires. The outermost wire plane on the sector structure is the gating grid. The grid controls the entry of ionized electrons from the TPC drift volume into the MWPC. To minimize the buildup of positively charged ions in the drift volume, the gating grid is normally closed (voltages alternate ±75 V from the nominal value) but opens (held at 110 V equipotential relative to the surrounding material) when a trigger is received. The TPC pad plane together with the anode wires and ground plane (shield grid) forms STAR's multi-wire proportional chamber. When electrons pass the gating grid and drift to the anode wires (held at 1170 V for the inner and 1390 V for the outer sector), they initiate avalanches. The readout pads directly below the anode wires detect the signal induced by the ions created in this avalanche.

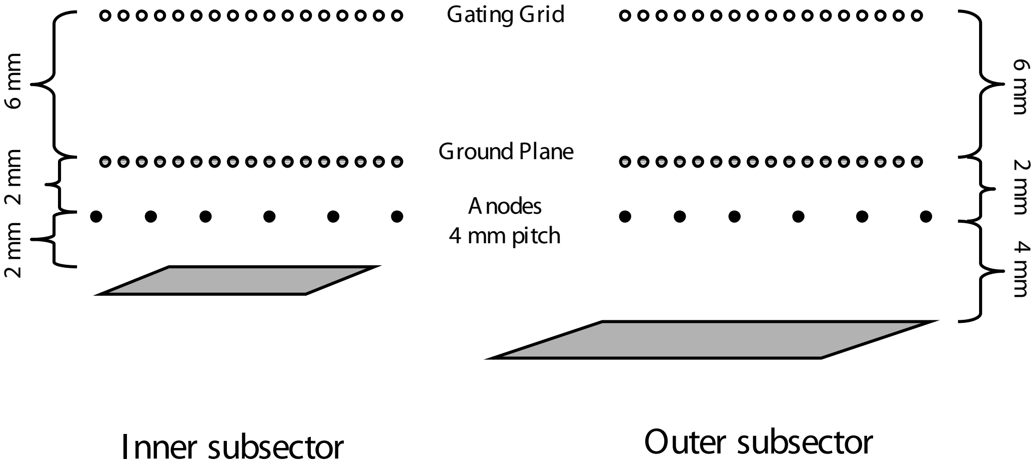

Figure 3.9: The readout chamber region of the STAR TPC. The gating grid and ground plane wires are on a 1 mm pitch, while the anode wires are spaced every 4 mm. Figure is taken from [37]

.

The track of a primary particle passing through the TPC is reconstructed by finding ionization clusters along the track for x, y and z-space separately. The x and y coordinates of a cluster are determined by the charge measured on adjacent pads in a single pad row. The z coordinate of a point inside the TPC is determined by measuring the time of drift of a cluster of ionized electrons from the point of origin to

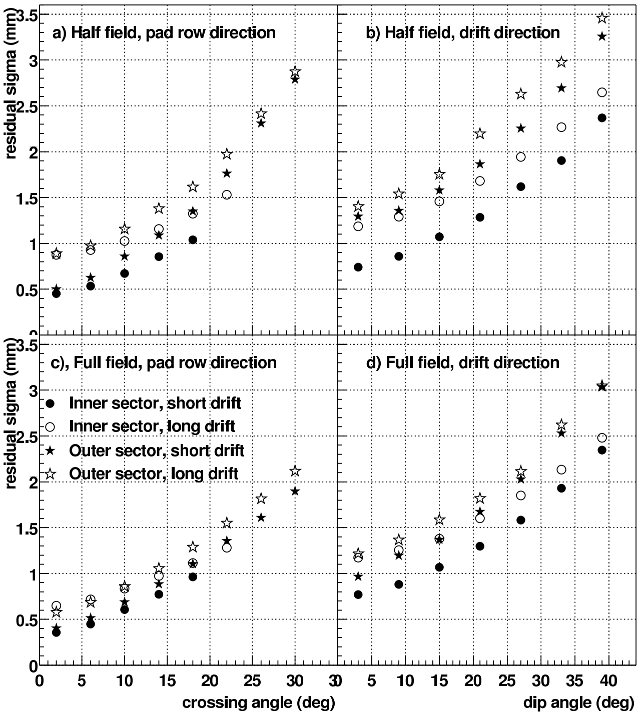

Figure 3.10: Position resolution across the pad rows (a,c) and along the z-axis (b,d) of the TPC. The crossing angle is the angle between the particle momentum and the pad row direction. The dip angle is the angle between the particle momentum and the drift direction, $\theta = \cos^{-1}(p_z/p)$. Figures are taken from [36]

the anodes on the endcap and dividing by the average drift velocity. Figure 3.10-a&c presents the position resolution along the pad rows and Figure 3.10-b&d for the z-axis of the TPC in 0.25 and 0.5 Tesla magnetic fields. The residual sigma is extracted by fitting a Gaussian distribution to the residual distribution (i.e. the distance between the track extrapolation and the hit position). The crossing angle is the angle between the particle momentum and the pad row direction. The dip angle is the angle between the particle momentum and the drift direction, $\theta = \cos^{-1}(p_z/p)$. The resolution is best for short drift distances and small crossing and dip angles.

3.4 Trigger Detectors

The luminosities at RHIC (Au+Au collisions: $L \approx 2 \times 10^{26}$ cm^{-2}s^{-1} and p+p collisions: $L \approx 6 \times 10^{30}$ cm^{-2}s^{-1}) provide a rich data taking environment. A triggering system is required to select events to record during the run since STAR can take data at input rates up to 100 Hz while RHIC can deliver $\sim$ 2000 Hz collisions. It is essential to optimize the selection of the events that will be recorded based on the geometry of the Au+Au collision. The multiplicity of the events vary depending on the geometry of the Au+Au collision. The three trigger detectors that are used in the analysis of the data provided in this thesis: the two Zero Degree Calorimeters (ZDCs), Central Trigger Barrel (CTB) for Au+Au collision, and Beam Beam Counters (BBCs) for p+p collisions. The 'hadronic minimum bias' trigger requires a coincidence between the two ZDCs with summed signals in each greater than $\sim$ 40% of a single neutron signal. The 'central' triggered Au+Au collisions are recorded with the required signals in both ZDCs and the CTB signal is above a very high threshold. The 'minimum bias p+p' collisions are triggered if the signal is higher than a predetermined threshold of summed signals of all tiles on each BBC. The trigger for 'minimum bias d+Au' collisions is based on a single ZDC which lies in the fragmentation region of the Au ions.

3.4.1 Zero Degree Calorimeter

The main purpose of the two Zero Degree Calorimeters is to detect spectator neutrons emitted along both beam directions and to measure their total energy (multiplicity) to provide a hadronic minimum bias signal and to verify centrality in Au+Au collisions [38]. The ZDCs also provide luminosity monitoring for heavy ion collisons. Each of the four RHIC experiments is equipped with a pair of ZDCs so that the RHIC machine can be tuned for the optimum collision rates. Each of them is located 17 meters away from each side of the intersection point along the beam direction. The configuration of the detectors is shown in Figure 3.11. Neutral beam fragments can be detected downstream of RHIC heavy ion collisions with the ZDC detectors. In each ZDC there is a hadron calorimeter consisting of tungsten plates with alternating layers of optical fibers. The Cherenkov light produced by shower electrons, due to energy deposit from the fragmented neutrons, is measured.

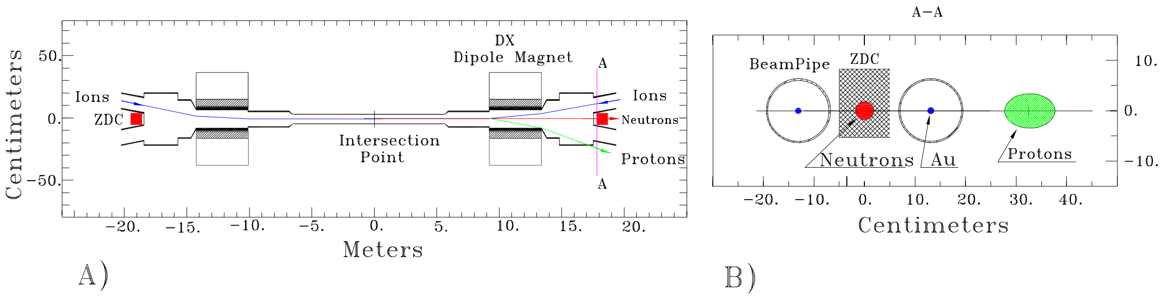

Figure 3.11: (**A**) Configuration of the Zero Degree Calorimeter detectors within the collision region. (**B**) The 'beam's eye' view of the ZDC location indicating position of neutrons, and deflection of protons and charged fragments (with Z/A∼1) downstream of the DX dipole magnet.

3.4.2 Central Trigger Barrel

The Central Trigger Barrel's main purpose is to measure charged particle multiplicity over $-1 < \eta < 1$. It consists of 240 scintillator slats arranged in four cylindrical bands each covering a half unit of pseudo-rapidity. The CTB slats are located on the outer shell of the 4 m diameter TPC.

Correlations between the ZDC and CTB signals are presented in Figure 3.12. In the most peripheral collisions, the multiplicity at mid-rapidity is small and the number of dissociation neutrons is scarce corresponding to a low CTB signal and a low sum of the East and West ZDC signals, respectively. The correlation of the CTB and ZDC for the Minimum Bias Trigger, which includes these peripheral collisions, can be seen in the left plot with the signals in the lower left corner corresponding to the peripheral events. As the overlap area of the colliding nuclei increases, the multiplicity of the events increases due to the higher number of participants in the collision, and since more neutrons are dissociated, the counts in the ZDCs increase. When the collisions are sufficiently central the number of neutron counts in the ZDC decreases while the multiplicity of the events as measured in the CTB still increases.

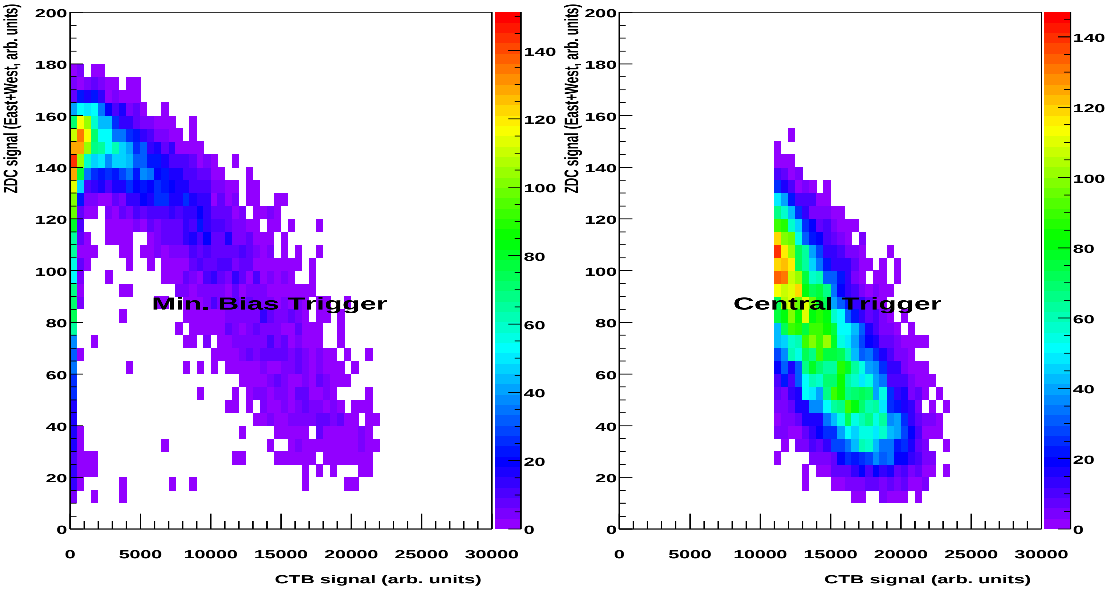

Figure 3.12: Correlation between the Zero Degree Calorimeter vs Central Trigger Barrel counts for the Minimum Bias and Central Triggers in Au+Au Collisions.

3.4.3 Beam Beam Counters

In p+p collisions the traditional Au+Au trigger detectors (CTB and ZDC) cannot be used due to the lower multiplicity of p+p events and since there are no neutrons in the colliding beams. An additional trigger detector, the Beam Beam Counter (BBC), is implemented for p+p operation. There are two BBC detectors on the outside of the east and west poletips of the STAR magnet located 3.5 meters away from the interaction points. From outside of the STAR magnet looking towards the interaction point along the beam, there are two annuli tiled by small and large hexagonal cells as presented schematically in Figure 3.13. The large cells have exactly four times the dimensions of the small cells. The small hexagon marked 'B' is reserved for the beam pipe. The 1 cm annular clearance between the beam pipe and the inner ring of small hexagonal scintillators sets the scale. The small regular hexagons can be inscribed in a circle of diameter 9.64 cm.

For the FY02 run, eight photomultiplier tubes (PMT) were used for the 18 small hexagonal scintillator tiles comprising one annulus on both the east and west sides

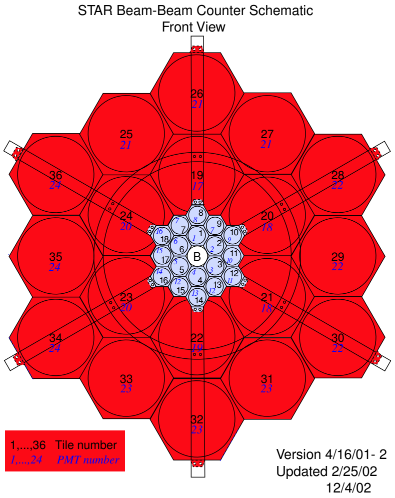

Figure 3.13: The cut away view of the STAR Beam Beam Counter. The BBCs are located on the outside of the east and west poletips of the STAR magnet. The inner region (tiles 1-18) lie within an approximate circle of radius ∼10 cm. The beam is perpendicular to the page and intersects the BBC in the non-instrumented region labelled 'B'.

of the STAR magnet. The p+p events are accepted if both BBCs have a total signal from all tiles above a predetermined threshold within a time window.

Chapter 4

Analysis

In this chapter the event and track selection and the identification techniques for the decay particles of the $\Sigma^*(1385) \rightarrow \Lambda+\pi$ using the STAR TPC will be introduced. The identification of the neutral Λ via the mixed event technique for the pure combinatorial and the decay vertex topology for the hybrid combinatorial technique for the $\Sigma^*(1385)$ baryon reconstruction are introduced. We discuss the pros and cons of these two different techniques that are used for the reconstruction of the $\Sigma^*(1385)$ baryon. Since the Ξ baryon shares the same decay channel ($\Xi^- \rightarrow \Lambda + \pi^-$) with $\Sigma(1385)^-$ baryon ($\Sigma(1385)^- \rightarrow \Lambda + \pi^-$), the measurements with the same techniques for Ξ^- and the $\bar{\Xi}^+$ are presented. Optimization of experimental cuts are discussed for extracting the signals. $\Sigma^*(1385)$ and $\overline{\Sigma^*}(1385)$ raw yields from p+p, Au+Au, and d+Au collisions at $\sqrt{s_{\mathrm{NN}}} = 200$ GeV collisions are presented.

4.1 Event Selection

The events are triggered as discussed in the previous chapter first depending on if they took place within the TPC. Due to the long bunch length (i.e. ~ 20 cm in a Au bunch), the collisions can occur along the beam line (along Z direction) at any position. Distributions of the Z position of the primary interaction vertex in p+p and Au+Au collisions with and without event selection are shown in Figure 4.1. The 'false' sharp peak at $Z = 0$ before event selection is due to events where the primary vertex cannot be reconstructed and assigned $Z = 0.000$ cm in the track reconstruction chain. The primary vertex is found by considering all tracks reconstructed in the TPC and then extrapolating them back to the origin. When the multiplicity of an event is low, accurate identification of the primary interaction vertex in that event is not feasible.

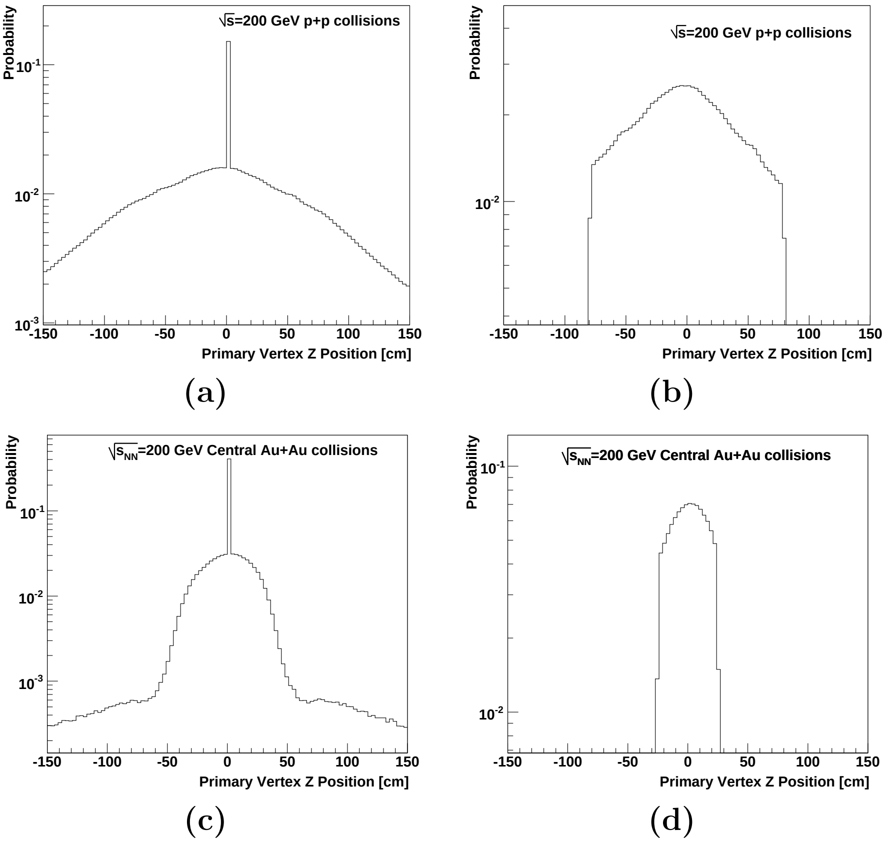

(a) (b) (c) (d)

Figure 4.1: Z position of the primary vertex distribution of events in the STAR TPC. Year 2 data set of minimum bias p+p collisions: (**a**) All triggered events before event selection. The population at $z = 0$ is mainly due to events when the primary vertex cannot be reconstructed due to pile-up events or low multiplicities. (**b**) After the events without primary vertex and the primary vertex at high z ($z > 85$ cm) are subtracted. Year 2 data set of central triggered Au+Au collisions: (**c**) All triggered events before event selection. (**d**) After the event selection. The difference in triggers during the data taking for Au+Au and p+p collisions can be seen dramatically in the z distributions of the primary vertex.

There is also a non-negligible probability that two or more bunch crossings may produce several individual events, so-called pile-up events. In these pile-up events, due to multiple interaction vertices, the correct primary vertex and therefore the momentum of the primary tracks cannot be extracted accurately. The events without a good primary vertex identification are rejected for this analysis. The tracking of the particles in an event depends highly on the primary interaction vertex location due to correlation of number of possible hits and efficiency. The events are selected with central vertex locations in the TPC to minimize the variations in the tracking. Table 4.1 gives the selection criteria of the accepted primary vertex for various collision systems. The selection criteria differ due to differences in the event multiplicities.

Collision System	Au+Au	p+p	d+Au
Accepted $\|Z\|$	< 25 cm	< 50 cm	< 50 cm
Accepted Ref Mult	< 800	< 25	< 50

Table 4.1: The primary vertex selection along the beam direction (Z position) and Ref Mult before centrality selection for events accepted for this analysis.

The multiplicity of the event is correlated with the geometry of the collision. In order to select collisions with similar geometries, a cut is applied on the track multiplicity in each event. The applied cuts on the reference multiplicity (Ref Mult[1]) for all centralities is given in Table 4.1 for various collision systems. The upper cut is required to divide events in equal multiplicity bins while calculating background contributions of the $\Sigma^*(1385)$ analysis.

Figure 4.2 presents the Ref Mult distributions for the p+p and Au+Au collisions before (black) and after (red) event selection. Centralities of the collisions are correlated with the multiplicities of the events and hence, by using the reference multiplicity of the events, different centralities of the collisions can be selected. For example in Figure 4.2-b, the 0-5% most central Au+Au collisions are selected from the Central triggered data set by accepting events with reference multiplicity greater than 510.

---

[1] Reference multiplicity defines the number of charged tracks. To be counted in the reference multiplicity a track must pass the following cuts; $|\eta| \leq 0.5$, number of Fit Points ≥ 10, and distance of closest approach to the primary vertex < 3 cm.

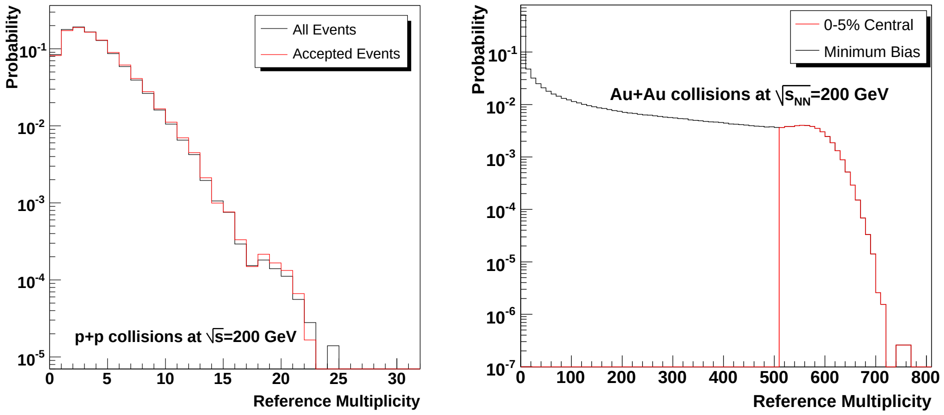

(a) (b)

Figure 4.2: Reference multiplicity distribution of accepted (red) and all triggered (black) events in the STAR TPC from Year 2 data set for **(a)** minimum bias p+p and **(b)** minimum bias Au+Au collisions at $\sqrt{s_{\mathrm{NN}}} = 200$ GeV. The selection of 0-5% most central Au+Au collisions can be performed by accepting events with a reference multiplicity greater than 510 as presented with the red curve.

4.2 Charged Particle Identification

Charged particles, such as π, K, p and e lose energy when they interact electromagnetically with the constituent gas of the STAR TPC. The magnetic field, which is parallel to the beam line, causes charged particles to follow helical trajectories about the field direction. The radius of curvature of a charged particle trajectory is determined by fitting a circle through the x, y coordinates (azimuthal coordinates) of the vertex point and the points along the track. The total momentum, with the assumption that the charge of the particle is ±1, is calculated using this radius of curvature and the angle that the track makes with respect to the z-axis (along the beam line). Particles also lose energy in frequent collisions with atoms as they traverse the gas of the TPC. The energy loss per unit length (dE/dx) of a track in the TPC is extracted from a fit of all clusters and the energy loss measured on all padrows associated with a given track.

Identification of charged particles is performed with their dE/dx and momentum information. The dE/dx distribution as a function of momentum of charged particles in the STAR TPC is presented in Figure 4.3. These particles can be clearly identified using the Bethe-Bloch parametrization shown as dashed lines in Figure 4.3. The mean energy loss $\langle\frac{dE}{dx}\rangle$ of a particle with charge Z and speed $\beta = v/c$ moving in a medium with density ρ is given as

$$-\frac{dE}{dx} = Kz^2\frac{Z}{A}\frac{1}{\beta^2}[\frac{1}{2}\ln\frac{2m_ec^2\beta^2\gamma^2E_M}{I^2} - \beta^2 - \frac{\delta}{2}]\ [39]. \tag{4.1}$$

For this formula, K represents a constant $4\pi N_A r_e^2 m_e c^2 = 0.307$ MeV cm^2 for r_e the classical radius and m_e the rest mass of the electron and N_A the Avogadro's number. The z is the atomic number and A is the atomic mass of the absorbing material. I corresponds to the mean excitation energy, and E_M is the maximum transferable energy in a single collision. While both β and γ are the kinematic variables with their usual meanings, δ is the density effect correction to ionization energy loss. Protons with momenta up to 1 GeV/c can be identified clearly with a 3 sigma Gaussian cut applied around the Bethe-Bloch parametrization curve. It is not possible to identify π and K mesons cleanly for momenta above 800 MeV/c when this dE/dx technique is used, since the curves cross-over in this region.

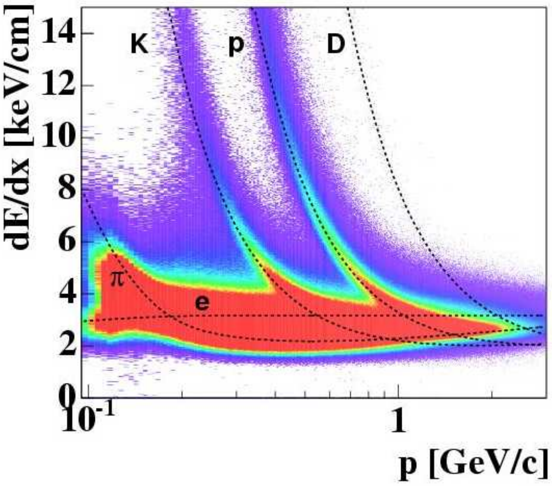

Figure 4.3: Distributions of the energy loss per unit length (dE/dx) in the STAR TPC as a function of momentum of the charged particles from the Year 2 data set for minimum bias p+p collisions. The bands represent the Bethe-Bloch parametrization for electrons, pions, kaons, protons and deuterons.

4.3 $\Sigma^*(1385)$ Identification

The $\Sigma^*(1385)^\pm$ decays strongly into a Λ and a $\pi^\pm$ as illustrated in Figure 4.4. The direct identification and measurement of the $\Sigma^*(1385)$ in the detectors is not possible due to its short life-time ($c\tau_{\Sigma(1385)} = 6$ fm). Instead, the $\Sigma^*(1385)$ and other short-lived resonances are identified by reconstructing the invariant mass distribution from their decay daughter candidates via a combinatorial technique. Equation 4.2 is used to calculate the invariant mass distribution of a resonance that decays into two daughter particles with masses M_1 and M_2 and momenta $\overrightarrow{p_1}$ and $\overrightarrow{p_2}$.

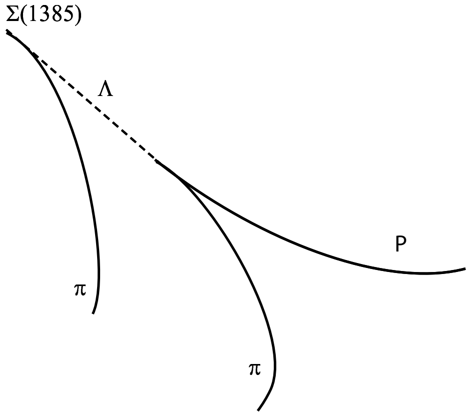

Figure 4.4: Schematic representation of a $\Sigma^*(1385)$ decay. The $\Sigma^*(1385)$ decays strongly into a Λ and a bachelor π. The neutral Λ candidate can be identified by first selecting charged daughter particles, π^- and p, and then calculating their invariant mass distribution. Charged particles are identified by energy loss per unit length with momentum determination in the magnetic field.

$$M^2_{Resonance} = M_1^2 + M_2^2 + 2(E_1E_2 - \overrightarrow{p_1} \cdot \overrightarrow{p_2}) \tag{4.2}$$

Energies of the daughter particles E_1 and E_2 are calculated with Equation 4.3 by using conservation of energy. For the $\Sigma^*(1385)$ analysis the particle data group mass values are used for the stable daughter particles ($\text{Mass}_\pi = 139.57$ MeV and $\text{Mass}_\Lambda = 1115.68$ MeV). These stable particle energies are thus calculated, with measured momenta in the STAR TPC, by using

$$E_{1,2}^2 = M_{1,2}^2 + |\overrightarrow{p_{1,2}}|^2. \tag{4.3}$$

In order to enhance the significance of the $\Sigma^*(1385)$ signal, $\Sigma^{*+}(1385) \rightarrow \Lambda + \pi^+$ and $\Sigma^{*-}(1385) \rightarrow \Lambda + \pi^-$ are combined.

4.3.1 Three Particle Combinatorial Technique (TPM)

The neutral Λ does not interact with the TPC gas and therefore does not leave a track as represented by the dashed line in Figure 4.4. However the p and π from the decay of the Λ are charged and can be identified by their energy loss per unit length and trajectory in the magnetic field as described in Section 4.2. In the three particle combinatorial method (TPM), every selected π^- is combined with every selected p to calculate a candidate Λ invariant mass distribution using Equation 4.2. (M_1 for π^- is 139.57 MeV and M_2 for p is 938.27 MeV.) Figure 4.5 shows the calculated invariant mass distribution for the Λ candidates in p+p collisions at $\sqrt{s_{\mathrm{NN}}}$ = 200 GeV. The grey band represents the selected Λ candidates that are combined with a π to derive the invariant mass spectrum of $\Sigma^*(1385)$. For all combined pairs of cleanly identified π and proton, the signal to background of the Λ signal is one to three.

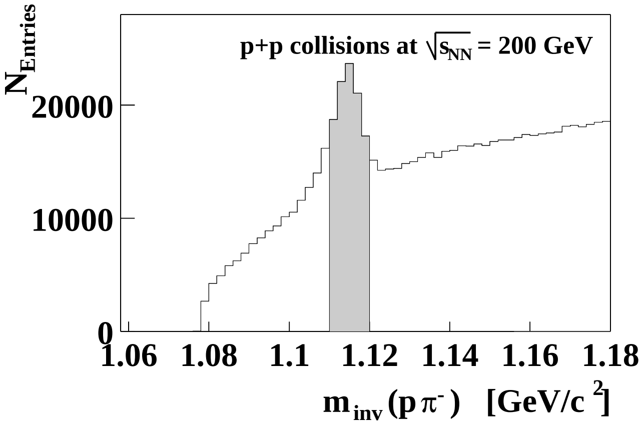

Figure 4.5: Invariant mass distribution of Λ candidate from π^- and p identified in the STAR TPC in p+p collisions at $\sqrt{s_{\mathrm{NN}}}$ = 200 GeV.

Invariant mass spectrum of the $\Sigma^*(1385)$ candidate is reconstructed using the selected Λ baryon candidates and all selected π mesons within the same event. There is a large source of background using this technique that comes from uncorrelated π and Λ pairs. A mixed event technique, where no real correlations are possible, is used to estimate the contribution of this background [9, 11]. For the $\Sigma^*(1385)$ case, the mixed event background is described by combining π mesons from one event with Λ baryons of another event and calculating the invariant mass distributions. The background is normalized over a wide kinematic range to minimize possible biases, and this background is then subtracted from the original invariant mass distribution. The invariant mass spectrum for the $\Sigma^*(1385)$ is presented in Figure 4.6-a as the black curve and the corresponding normalized background as the red curve. In Figure 4.6-b the mass spectrum of $\Sigma^*(1385)$ after the background subtraction is shown. The doubly strange baryon, Ξ^-, also decays into a Λ and π^-. Therefore, there is a peak at the mass 1.321 GeV/c^2 in the Λ and π^- invariant mass spectrum that corresponds to the Ξ^- baryon.

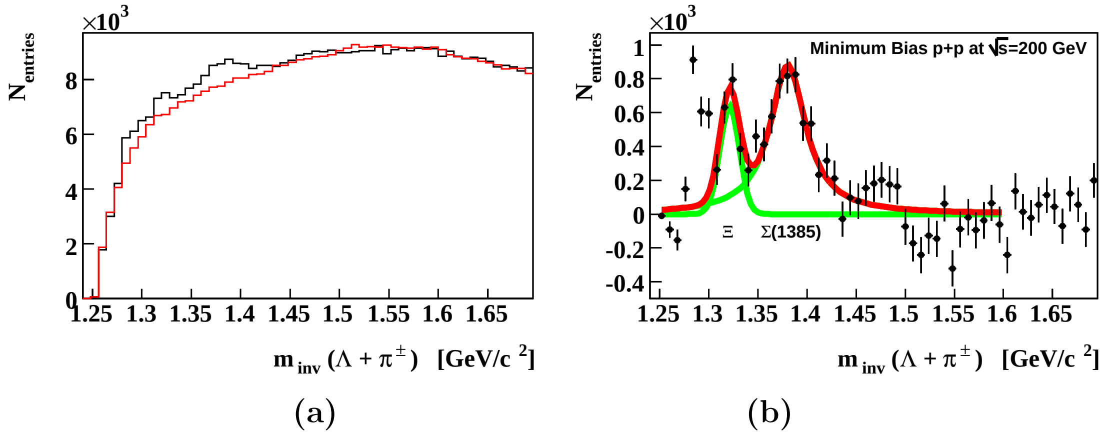

(a) (b)

Figure 4.6: (**a**) The invariant mass distribution (in black) of $\Lambda + \pi^{\pm}$ from the TPM technique in minimum bias p+p collisions at $\sqrt{s_{NN}} = 200$ GeV. The normalized mixed event background for the $\Sigma^*(1385)$ is presented in red. (**b**) The mixed event background subtracted invariant mass distribution with a Gaussian fit for the Ξ^- and a Breit-Wigner fit for the $\Sigma^{*\pm}(1385)$.

The $\Sigma^*(1385)$ is fit with a Breit-Wigner and the Ξ is fit with a Gaussian distribution. These fits are shown in Figure 4.6-b. The Breit-Wigner function used to describe the $\Sigma^*(1385)$ mass distribution is

$$\frac{A}{4(M-M_0)^2+\Gamma^2}, \tag{4.4}$$

for the fit variables A the amplitude dependent parameter, M_0 the peak invariant mass for the $\Sigma^*(1385)$, and Γ the full width of the $\Sigma^*(1385)$ distribution [40]. The Gaussian function for the Ξ mass distribution is

$$A\exp(-0.5(\frac{M-M_0}{\Gamma})^2). \tag{4.5}$$

The full invariant mass distribution of $\Lambda+\pi$ is fit with the sum of the distributions described in Equation 4.4 and Equation 4.5.

The observed population above the background near the kinematic cut off ($\sim$ 1.28 GeV/c^2) is due to correlated combinations that cannot be subtracted via the mixed event technique. Misidentification of particles such as misidentified Ω baryons are one of the possible causes of this excess due to the similar three particle decay of the Ω ($\Omega \to \Lambda + K$). Details of the investigation of this background using Monte Carlo studies can be found in Chapter 5.

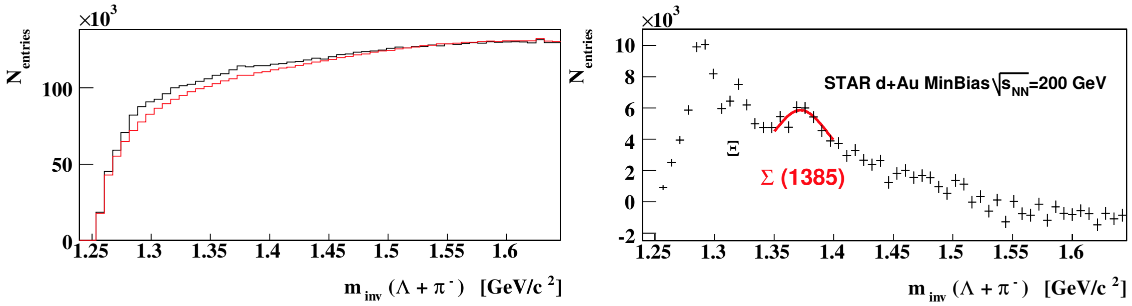

(a) (b)

Figure 4.7: (**a**) $\Lambda+\pi$ invariant mass distributions from the three particle combinatorial technique before background subtraction in black and the normalized mixed event background in red; (**b**) the invariant mass distribution after the mixed event background subtraction in minimum bias d+Au collisions at $\sqrt{s_{NN}} = 200$ GeV.

The magnitude of the correlated background structure in the lower kinematic cut off region (peaked at $\sim$ 1.28 GeV/c^2) increases as the event multiplicity increases. Figure 4.7-a shows the $\Sigma^*(1385)$ invariant mass spectrum before the mixed event background subtraction (in black) and the normalized mixed event background (in red) in d+Au collisions at $\sqrt{s_{\mathrm{NN}}}$ = 200 GeV. Figure 4.7-b presents the invariant mass spectrum after the normalized mixed event background subtraction. In comparison to p+p collisions (see Figure 4.6) the significance of the correlated background in d+Au collisions increases.

The invariant mass spectra before and after the mixed event background subtraction for the Au+Au Minimum Bias collisions at $\sqrt{s_{\mathrm{NN}}}$ = 200 GeV are presented in Figure 4.8. Neither $\Sigma^*(1385)$ nor Ξ signals are visible after the mixed event background subtraction due to the correlated background around the kinematic cut off region as can be seen in Figure 4.8-b. This background totally dominates the spectrum in Au+Au collisions due to an increase in background combinatorial statistics and prohibits the identification of the Ξ and the $\Sigma^*(1385)$.

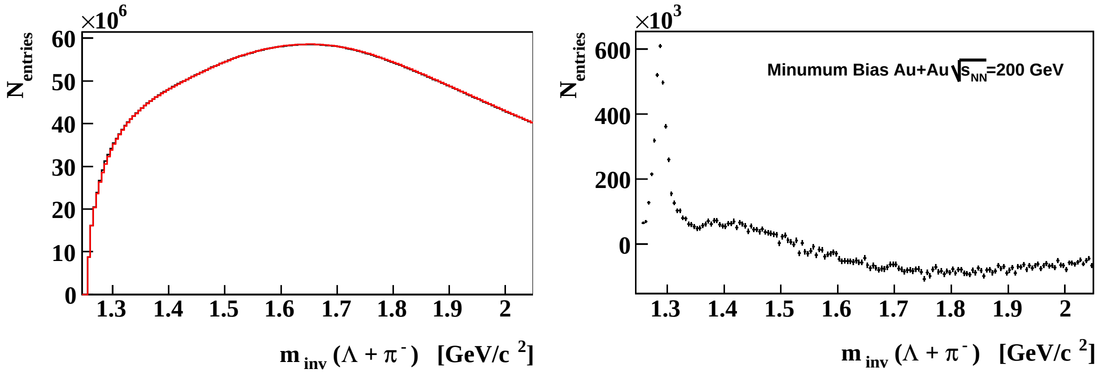

(a) (b)

Figure 4.8: (**a**) $\Lambda + \pi$ invariant mass distributions from the three particle combinatorial technique before background subtraction in black and the normalized mixed event background in red; (**b**) the invariant mass distribution after the mixed event background subtraction in minimum bias Au+Au collisions at $\sqrt{s_{NN}}$ = 200 GeV. The magnitude of the 'false' peak is high and both Ξ and the $\Sigma^*(1385)$ signals are not visible.

4.3.2 Hybrid Combinatorial Technique (HCT)

The long-lived ($c\tau >$ few cm) strange particles such as the Λ and K^0_S can also be reconstructed in the TPC from their charged decay products. Due to the neutral

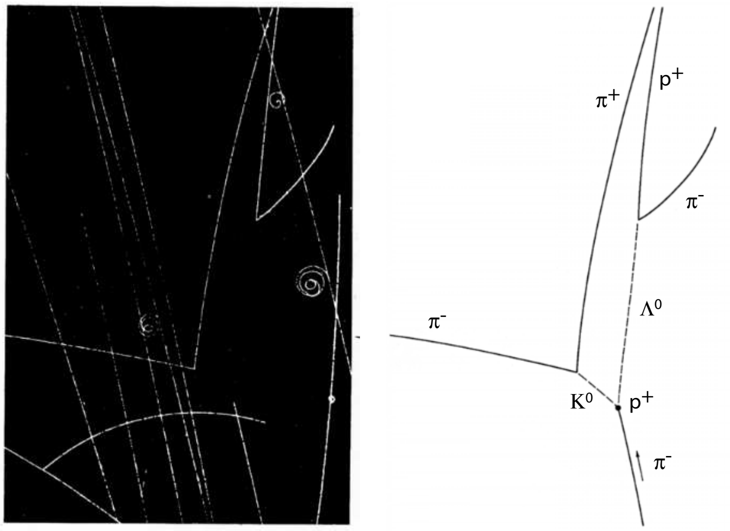

(a) **(b)**

Figure 4.9: (**a**) A photograph of Λ and K^0_S production and decay in a bubble chamber experiment and (**b**) diagram showing reconstruction of the interaction in the photograph [41].

charge of the K^0_S and Λ particles, only their decay particles, which look topologically like the letter V were observed in the first bubble chamber experimental setups. Figure 4.9 shows a photograph from a bubble chamber experiment at Lawrence Berkeley National Laboratory with a corresponding diagram showing reconstruction of the interaction seen in the photograph [41]. In this photograph a number of negatively charged π mesons enter from the bottom; these are the beam particles and have momenta of 1.20 GeV/c. The mesons thus move at 99.3% the speed of light. One of the beam particles interacts with a proton to form a neutral Λ and a neutral K^0_S; both of these leave no track in the bubble chamber since they have no electric charge. However when Λ and K^0_S decay into charged particles, these charged particles leave tracks in the chamber. The Λ decays into a proton and a π^- meson; the K^0_S decays into a π^+ meson and a π^- meson. Candidates of neutral particles that later decay into two charged particles, such as the K^0_S meson and Λ baryon, are called V_0 particles due to their characteristic decay topology.

A reconstruction chain called a V_0 finder is used to identify V_0 particles from the data collected with the STAR detector. All pairs of oppositely charged tracks in

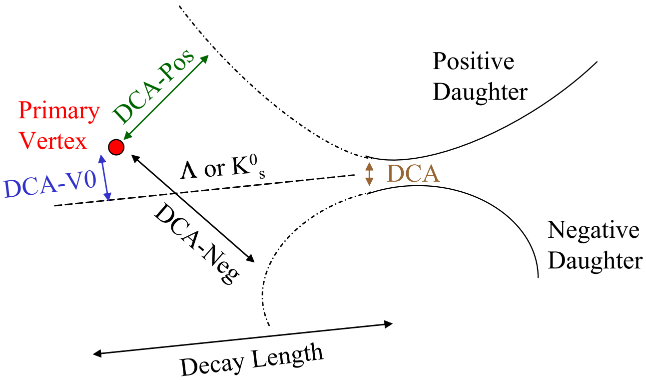

Figure 4.10: Schematic representation of a K_s^0 or Λ decay and corresponding parameters used for the topological analysis to identify K_s^0 and Λ particles.

the TPC are extrapolated towards the primary vertex to see if they originate from a secondary vertex representing the two-body decay topology of neutral particles. The geometric cuts applied with the V_0 finder are illustrated in Figure 4.10. The main cuts applied are the distance of closest approach (DCA) between the primary interaction vertex and the secondary decay vertex ($\mathrm{DCA}-\mathrm{V}_0$), DCA between the primary vertex and the DCA of the charged decay tracks ($\mathrm{DCA}-\mathrm{Pos}$ and $\mathrm{DCA}-\mathrm{Neg}$ for positive and negative charged tracks, respectively), DCA between the two charged tracks and finally the decay length. Upper and lower limits on these DCAs are applied to improve the signal of V_0 particles by minimizing the background contribution. The backgrounds are due to finite momentum resolution of the tracks in the TPC and a large number of fake secondary vertices resulting from primary tracks crossing each other. Since in the initial reconstruction chain the applied cuts are loose to accommodate different analysis needs, further cuts are applied to extract a clean sample of true V_0 particles. The invariant mass spectra of K_S^0 in Figure 4.11-a and Λ and $\overline{\Lambda}$ in Figure 4.11-b are presented for p+p collisions at $\sqrt{s_{\mathrm{NN}}} = 200$ GeV. The significance of the signals of V_0 particles from the topological reconstruction method are two orders of magnitude higher than the combinatorial technique (See Figure 4.5).

In the hybrid combinatorial technique (HCT) $\Sigma^*(1385)$ baryons are identified by combining these topologically reconstructed Λ baryons with π mesons. Figure 4.12 presents the invariant mass spectrum of the $\Sigma^*(1385)$ calculated with the HCT in p+p

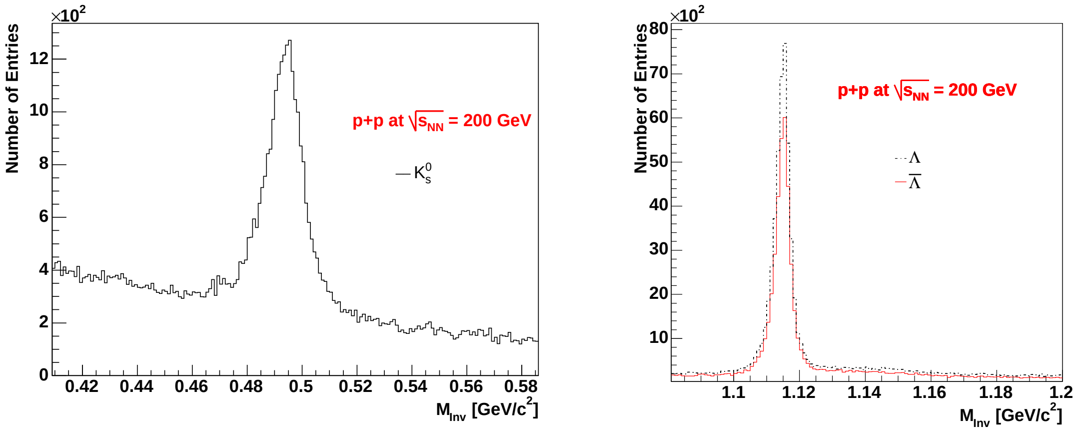

(**a**) (**b**)

Figure 4.11: Invariant mass spectra for (**a**) $K^0_S \longrightarrow \pi^+ + \pi^-$ and (**b**) for $\Lambda \longrightarrow p + \pi^-$ and $\overline{\Lambda} \longrightarrow \overline{p} + \pi^+$ using the decay topology technique in p+p collisions at $\sqrt{s_{NN}} = 200$ GeV.

collisions at $\sqrt{s_{\mathrm{NN}}}$ = 200 GeV. Figure 4.12 shows the invariant mass spectra before and after the mixed event background subtraction. The background is estimated in a similar way as in the TPM, by mixing π's from one event with Λ's identified with the topological technique from another event. Due to a cleaner sample of Λ candidates the excess around the kinematic cut off region as observed in the TPM is minimal. See Figure 4.6 to compare TPM and HCT methods of $\Sigma^*(1385)$ reconstruction in p+p collisions.

In the following sections, details of the specific HCT used for different collision systems and the results obtained in each data set are discussed.

4.4 $\Sigma^*(1385)$ Identification in p+p Collisions

The $\Sigma^*(1385)$ resonance is identified via calculating the invariant mass distribution of Λ and π as described in the previous section. In order to calculate the invariant mass spectrum of the $\Sigma^*(1385)$, its decay particles need to be identified. Table 4.2 shows the cuts applied on the V_0 particles to topologically reconstruct Λ baryons in p+p collisions at $\sqrt{s_{\mathrm{NN}}}$ = 200 GeV energy. Figure 4.13-a shows the invariant mass

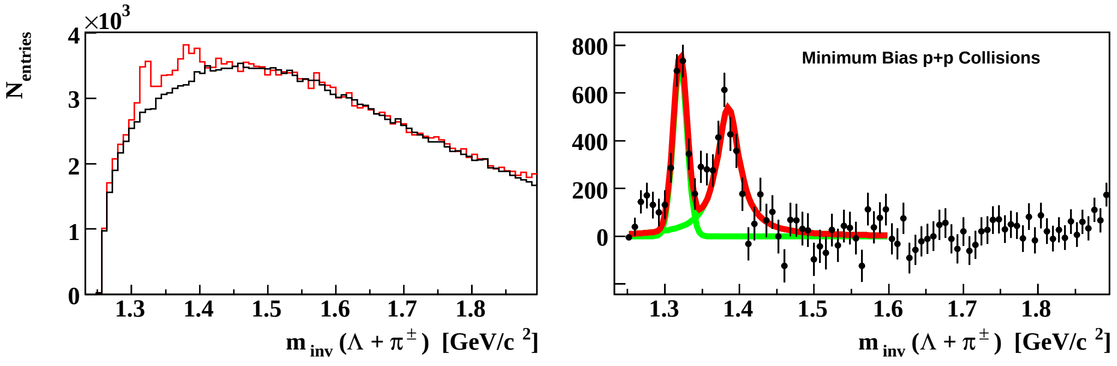

(a) (b)

Figure 4.12: (**a**) The invariant mass ($\mathrm{m_{inv}}$) distribution of $\Sigma^*(1385)$ before background subtraction in red and the normalized mixed event background in black for p+p collisions at $\sqrt{s_{\mathrm{NN}}} = 200$ GeV. (**b**) The $\mathrm{m_{inv}}$ distribution after mixed-event background subtraction for $\Sigma^* \rightarrow \Lambda + \pi^\pm$. Ξ^- (seen as peak at 1320 MeV) is fit with a Gaussian and $\Sigma^*(1385)$ is fit with a Breit-Wigner. Invariant mass signals for Ξ^- and $\Sigma^*(1385)$ particles are visible before the mixed event background subtraction.

distribution of $\mathrm{p} + \pi^-$ from topologically selected charged particles that pass the cuts in Table 4.2. These cuts are the DCA cuts presented in Figure 4.10 and the number of hit points for each track. The cut based upon the number of hit points is required to minimize the contribution of split tracks. A split track occurs when the track of a single particle with missing hit points in the middle is reconstructed as at least two separate tracks (multiple particles). From 45 hit points possible on a reconstructed track, a minimum of 15 hit points is chosen to minimize the probability of split tracks without losing significant statistics. Λ baryons are selected after a mass cut of 1.11-1.12 GeV/c^2 on the $\mathrm{p} + \pi^-$ invariant mass distribution.

The next step is to identify the π mesons. The charged π mesons are identified with the TPC using their energy loss per unit length and their momentum information as described in Section 4.2. Table 4.3 shows the cuts applied on primary tracks to select the most probable π candidates.

Figure 4.13-(b) and (c) shows the dE/dx vs momentum distribution for bachelor π mesons before and after the cuts given in Table 4.3 for π mesons. In order to increase the significance of the $\Sigma^*(1385)$ signals the charge states of $\Sigma^*(1385)$ are

Cut Description	Value
DCA of positive daughter to primary vertex [cm]	> 0.25
DCA of negative daughter to primary vertex [cm]	> 1.2
DCA between V_0 and primary vertex [cm]	< 2
DCA between daughters [cm]	< 1
Decay length of V_0 [cm]	$5 < L < 30$
Number of hits for positive daughters	> 15
Number of hits for negative daughters	> 15
dE/dx	$3\ \sigma$

Table 4.2: Cuts applied for Λ identification in p+p collisions at $\sqrt{s_{\rm NN}} = 200$ GeV energy.

Cut Description	Value
Momentum [GeV/c]	$0.1 - 1.2$
Number of fit points	> 15
dE/dx	$3\ \sigma$

Table 4.3: Cuts applied for π identification in p+p collisions.

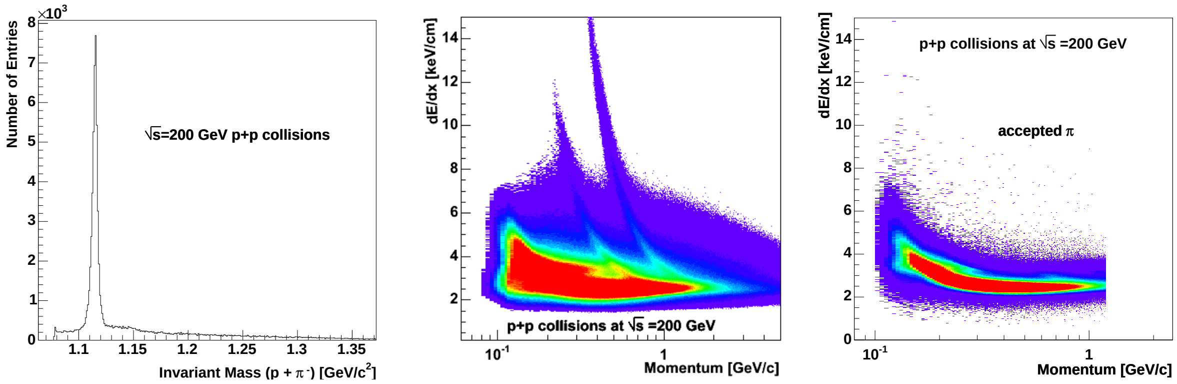

(a) **(b)** **(c)**

Figure 4.13: (**a**) Λ invariant mass distribution after the cuts given in Table 4.2. (**b**) dE/dx vs momentum for all tracks before cuts are applied (**c**) dE/dx vs momentum of accepted π tracks after the cuts given in Table 4.3 are applied. Contamination of electrons on the left side and kaons on the right side of the π distribution is visible.

added together before background subtraction. For particle states $\Sigma^{*+}(1385) \rightarrow \Lambda + \pi^+$ and $\Sigma^{*-}(1385) \rightarrow \Lambda + \pi^-$ are added, and for antiparticle states $\bar{\Sigma}^{*+}(1385) \rightarrow \bar{\Lambda} + \pi^+$ and $\bar{\Sigma}^{*-}(1385) \rightarrow \bar{\Lambda} + \pi^-$ are added.

The phase space distribution of the reconstructed $\Sigma^*(1385)$ and the corresponding mixed-event background are presented in Figure 4.14. The rapidity coverage is $|y| < 1$ due to the TPC acceptance. The transverse momentum of the $\Sigma^*(1385)$ is limited to $\mathrm{p_T} \leq 4$ GeV/c due to momentum cuts implied by particle identification for the π meson.

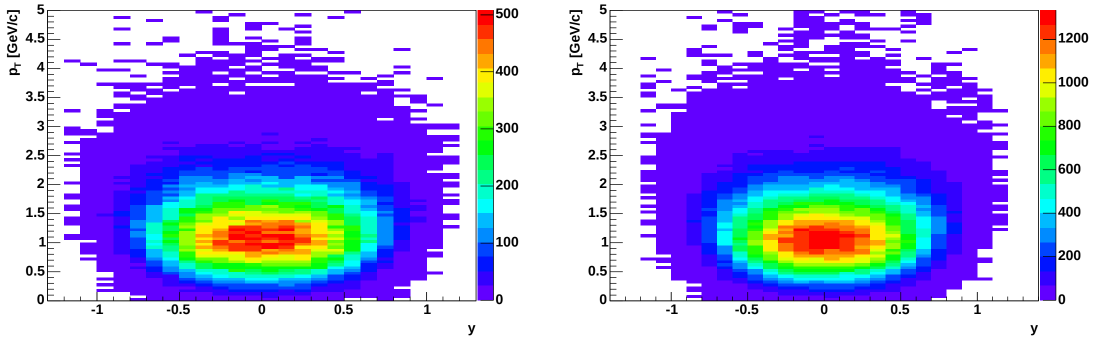

(a) **(b)**

Figure 4.14: (**a**) Transverse momentum versus rapidity distribution of $\Sigma^*(1385)$ and (**b**) the corresponding mixed event background. These signals can further be divided into smaller momentum and rapidity bins to measure and correct the transverse momentum spectra of $\Sigma^*(1385)$.

The invariant mass spectra of $\Sigma^{*\pm}(1385)$ and $\bar{\Sigma}^{*\pm}(1385)$ before and after the background subtraction for the rapidity range $|y| < 0.75$ and $\mathrm{p_T} < 4$ GeV/c from p+p collisions at $\sqrt{s_{\mathrm{NN}}} = 200$ GeV are presented in Figure 4.15. Peaks can be seen in the invariant mass distributions for $\Sigma^*(1385)$ baryons and anti-baryons even before normalized background subtraction in the left panels of Figure 4.15.

4.4.1 Raw $\Sigma^*(1385)$ Yields in p+p Collisions

The $\Sigma^*(1385)$ invariant mass spectrum is split into individual $\mathrm{p_T}$ bins due to differences in the correction factors for efficiency and acceptance. The invariant mass spectra for specific $\mathrm{p_T}$ bins for the $\Sigma^*(1385)$ are found in Appendix B. Figures B.1, B.2 and B.3 show the 9 $\mathrm{p_T}$ bins of $\Sigma^*(1385)$ invariant mass spectra before and after mixed-event background subtraction. The rapidity coverage of the $\Sigma^*(1385)$ is

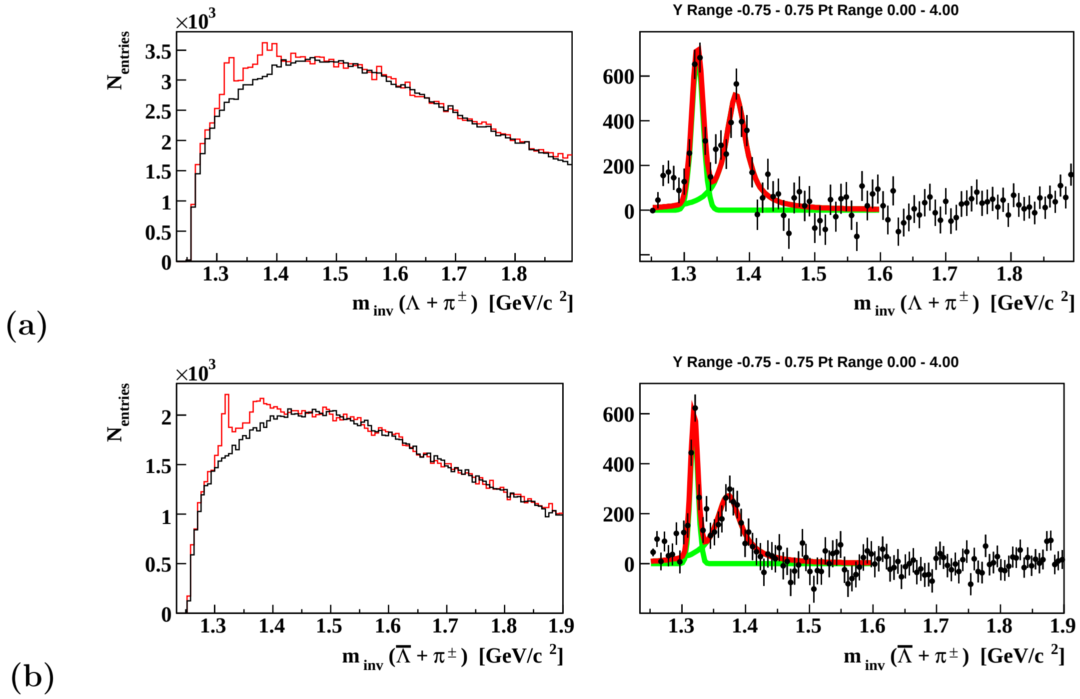

Figure 4.15: (**a**) Invariant mass spectra of $\Sigma^*(1385)$ baryons and (**b**) $\overline{\Sigma^*}(1385)$ anti-baryons for $|y| < 0.75$ and $p_T(\Sigma^*(1385)) < 4$ GeV/c. A Gaussian for Ξ and Breit-Wigner for the $\Sigma^*(1385)$ are fit to the mixed event background subtracted spectra.

$|y| < 0.75$ for all plots and the p_T ranges are 0.25-1, 1-1.25, 1.25-1.5, 1.5-1.75, 1.75-2, 2-2.25, 2.25-2.5, 2.5-2.75, 2.75-3.5 GeV/c. Ξ and $\Sigma^*(1385)$ peaks are visible even before background subtraction for all p_T ranges. A Gaussian for Ξ and a Breit-Wigner for the $\Sigma^*(1385)$ are fit to the background subtracted spectra. The χ^2/DOF and the probabilities of the fits are included in the insets of the plots. Due to differences in the significance of the signals for Ξ and $\Sigma^*(1385)$, the probabilities of the fits vary. The $\overline{\Sigma^*}(1385)$ invariant mass spectra for discrete p_T bins with the same cut ranges as used for the $\Sigma^*(1385)$ are presented in Figures B.4, B.5 and B.6 for rapidity $|\mathrm{y}| < 0.75$.

The raw counts for the yields are extracted by simply summing the number of counts under the peak rather than from the fits. This technique, also known as 'Bin Counting', is utilized due to the variations in the fit functions. Due to limited statistics on some p_T bins with low signal counts, the fit functions fail and do not represent the signals adequately. Both bin counting and the integration of the fits give similar raw counts when the fits successfully represent the signal. The bin counting technique requires that after background subtraction there is no additional background population under the resultant mass peak. The signal region is chosen in the range 1.33-1.40 GeV/c^2. This range covers 62 ± 10% of the signal and is chosen in a way to minimize the contribution from the Ξ and other Σ resonances. These counts are then corrected so that the raw yield covers the full range when the same assumption is used for the embedding data which will be discussed in Chapter 5.

The dependence of the raw spectra of $\Sigma^*(1385)$ and $\overline{\Sigma^*}(1385)$ on $\mathrm{m_T} - m_0$ in minimum bias p+p collisions, for $m_0 = 1.385$ GeV/c^2, are presented in Figure 4.16. The $\Sigma^*(1385)$ and $\overline{\Sigma^*}(1385)$ counts are plotted on the ordinate as:

$$\frac{1}{N_{Events}} \frac{1}{2\pi} \frac{1}{\mathrm{m_T}} \frac{1}{\Delta y} \frac{dN}{d\mathrm{m_T}}.$$

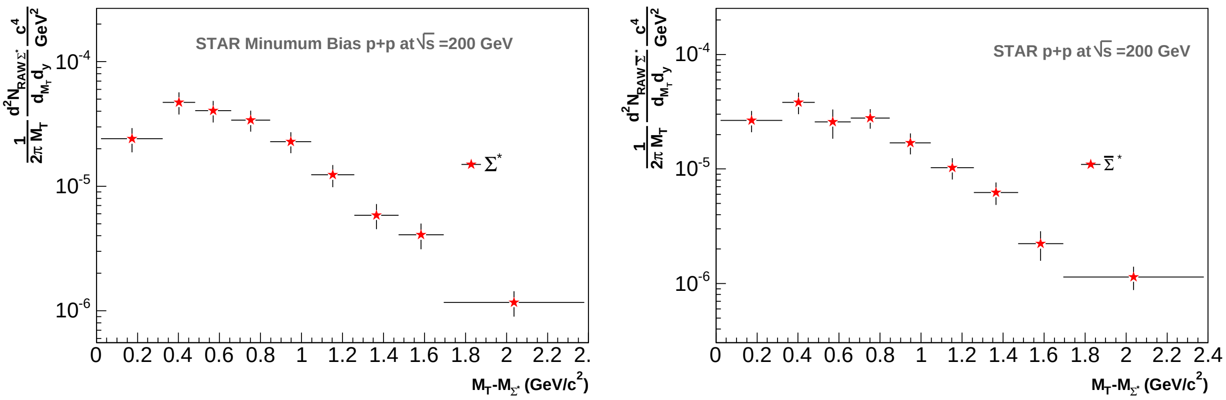

(a) **(b)**

Figure 4.16: The uncorrected transverse mass spectrum of the (**a**) $\Sigma^*(1385)$ baryon and (**b**) $\overline{\Sigma^*}(1385)$ anti-baryon in minimum bias p+p collisions at $\sqrt{s} = 200$ GeV.

4.4.2 Vertex Correction

The primary vertex of a collision is the point where the two nuclei collide. At RHIC the primary vertex can be located along the beam line anywhere within the TPC.

Comparison of p+p and Au+Au event vertex distributions are plotted in Figure 4.1. Finding the primary vertex in p+p events is challenging due to the low multiplicity within the p+p events, compared to Au+Au events, and due to the high luminosity of p+p collisions. Also 'pile-up' events may cause additional inefficiencies in primary vertex finding [42]. These inefficiencies result in misidentification of vertex position or an event lost when the vertex is not found at all. For per event yield extraction in minimum bias p+p collisions, it is essential that the events used for the analysis have no biases. Vertex correction is required to identify and overcome these inefficiencies.

Monte Carlo studies of the simulated pile-up events for p+p collisions have shown that the most stable variable to use for the vertex correction is the number of good primary tracks [43]. ('Good primary tracks' are defined as tracks with the properties of: Global DCA < 3 cm and the number of Fit Points > 15.) There are two different types of inefficiencies, which must be corrected for in different ways. The first type corresponds to 'lost' events (no vertex found at all). The fraction of lost events per number of good global tracks is shown in Figure 4.17-a as red triangles. Another

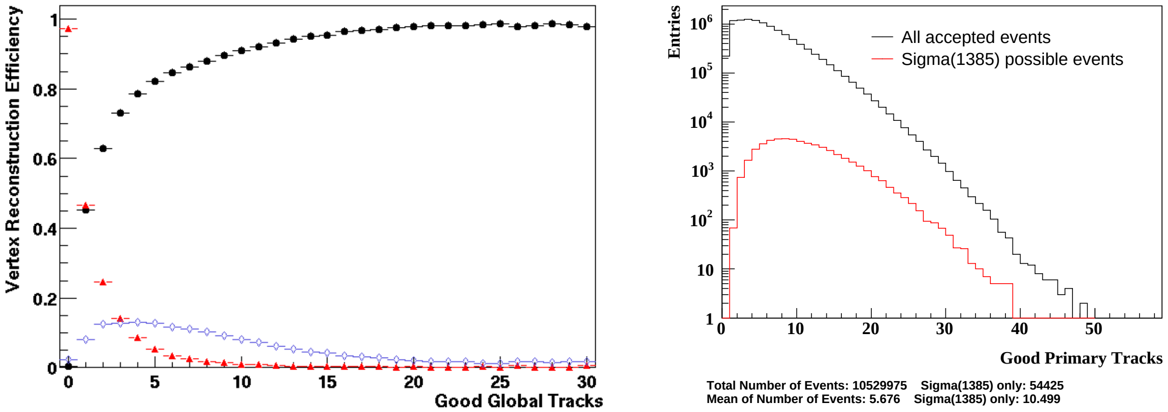

(a) **(b)**

Figure 4.17: (**a**) Good global tracks dependence of the vertex reconstruction efficiency in p+p events. Red triangles represent the fraction of lost events per number of good global tracks. The fake events are presented as blue diamonds. The overall efficiency is shown as black circles. See text for details. (**b**) The number of good primaries in all accepted events and those with a reconstructed $\Sigma^*(1385)$. The mean is shifted towards higher values for the $\Sigma^*(1385)$ events.

type of inefficiency comes from events where the vertex was reconstructed in the wrong place. These events are called ‘fake’ if the three dimensional distance between Monte-Carlo simulated and reconstructed vertex is greater than 2 cm. The fraction of such ‘fake’ events is shown as blue diamonds in Figure 4.17-a. The overall efficiency (accounting for both ‘lost’ and ‘fake’) is shown in Figure 4.17-a as black circles and is accounted for when the raw counts of $\Sigma^*(1385)$ are normalized to the number of events. This correction is applied as a weight to the entire event and is universal for any analysis. This results in an overall re-normalization of events by a factor of $\sim .857$.

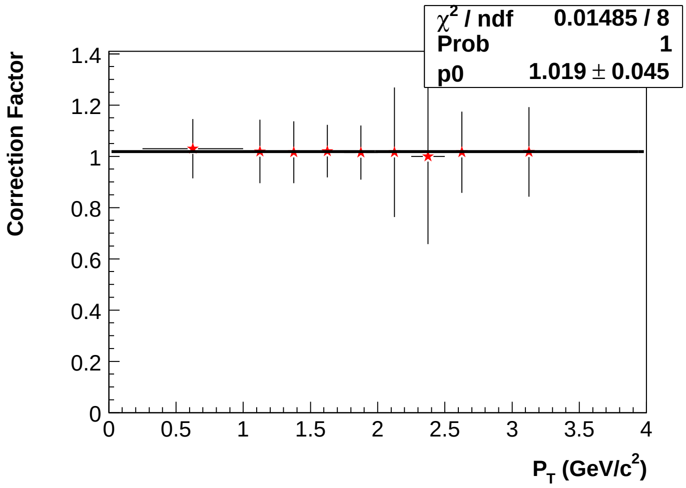

Figure 4.18: The p_T dependence of the $\Sigma^*(1385)$ correction factor for inefficiencies due to primary vertex identification.

If $\Sigma^*(1385)$ baryons are produced in events with failed or displaced primary vertex identification, they will be lost in our reconstruction chain. Figure 4.17-b shows the number of good primaries in all accepted events and the ones which are used for the $\Sigma^*(1385)$ analysis. The mean number of charged tracks in events which are used for possible $\Sigma^*(1385)$ reconstruction (at least one Λ and one π that pass the cuts) is ~ 10.5 while the mean number of charged tracks in all events is ~ 5.7. The shift towards higher values is due to the three body decay of the $\Sigma^*(1385)$ (minimum number of tracks in an event accepted for $\Sigma^*(1385)$ reconstruction is 3). The p_T dependence of the $\Sigma^*(1385)$ correction factor for inefficiencies of the primary vertex identification is presented in Figure 4.18. The line is a linear fit for the correction factors to estimate approximately the overall effect for all bins. The correction factor from the linear fit is around 2%. Due to the exponential distribution of the $\Sigma^*(1385)$ production, instead of this overall correction factor from the fit function, a bin by bin correction is undertaken.

The $\Sigma^*(1385)$ yield in p+p events is calculated for events with Z position of the primary vertex restricted to $|\mathrm{PV_Z}| < 50$ cm. The correction factors are estimated more accurately for this range. Details of this discussion can be found in Chapter 5.

4.5 $\Sigma^*(1385)$ Identification in Au+Au Collisions

The $\Sigma^*(1385)$ is reconstructed via the invariant mass spectrum using the hybrid mixing technique for the 0-5% most central Au+Au collisions. Due to the higher number of tracks produced, the cuts applied for the decay particle selection are tighter including a lower momentum cut. Table 4.4 shows the applied cuts on the V_0 particles to topologically reconstruct Λ baryons in the 0-5% most central Au+Au collisions at $\sqrt{s_{\mathrm{NN}}} = 200$ GeV.

Cut Description	Value
DCA of positive daughter to primary vertex [cm]	> 0.9
DCA of negative daughter to primary vertex [cm]	> 2.95
DCA between V_0 and primary vertex [cm]	< 0.5
DCA between daughters [cm]	< 0.75
Decay length of V_0 [cm]	$5 < L < 30$
Number of hits for positive daughters	> 15
Number of hits for negative daughters	> 15
dE/dx	$3\ \sigma$
Momentum of p [GeV/c]	> 0.1
Momentum of π [GeV/c]	> 0.1

Table 4.4: Cuts applied for Λ identification in 0-5% most central Au+Au collisions.

The next step is to identify the π mesons. As in the p+p case the charged π mesons are identified with the TPC from their energy loss per unit length and momentum information. Table 4.5 shows the cuts applied on primary tracks to select the most probable π meson candidates.

Cut Description	Value
Momentum [GeV/c]	0.1 – 1.0
Number of Fit Points	> 15
dE/dx	3 σ

Table 4.5: Applied cuts for π identification in 0-5% most central Au+Au collisions.

Figure 4.19 shows the invariant mass distribution of selected Λ baryons and dE/dx vs momentum distribution for charged particles before and after the applied cuts given in Table 4.4 and Table 4.5 for Λ baryons and π mesons, respectively.

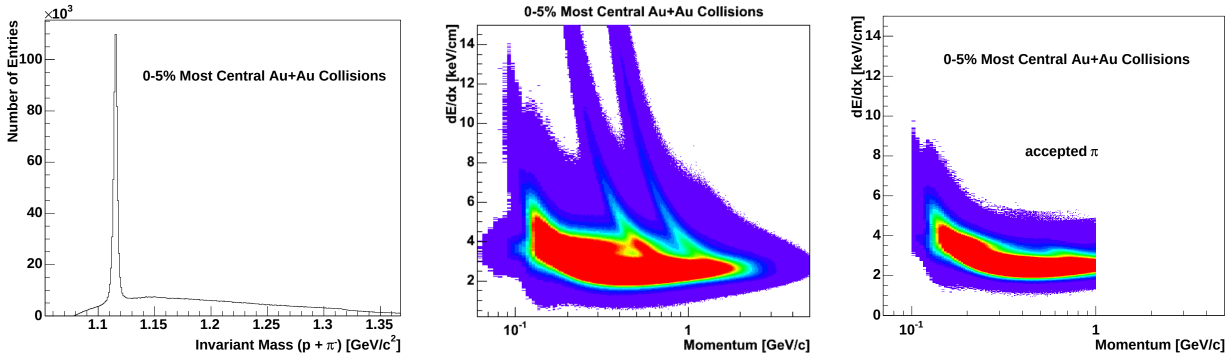

(**a**) (**b**) (**c**)

Figure 4.19: (**a**) Selected Λ invariant mass distribution after the applied cuts given in Table 4.4. (**b**) dE/dx vs momentum for all tracks before any cuts are applied (**c**) dE/dx vs momentum of accepted π tracks after the cuts given in Table 4.5 are applied. Contamination of electrons on the left side and kaons on the right side of the π distribution is visable.

The momentum and energy information of accepted π mesons and Λ baryons are used to calculate the invariant mass of the $\Sigma^*(1385)$ and $\overline{\Sigma^*}(1385)$ baryons. Figure 4.20 presents the $\Sigma^*(1385)$ and $\overline{\Sigma^*}(1385)$ invariant mass spectra before and after the mixed event background subtraction.

There are 1.7 million central triggered events recorded before any event selection in central Au+Au collisions from FY02. This number goes down to 750 K when quality cuts and centrality selection are applied. The smaller event statistics and

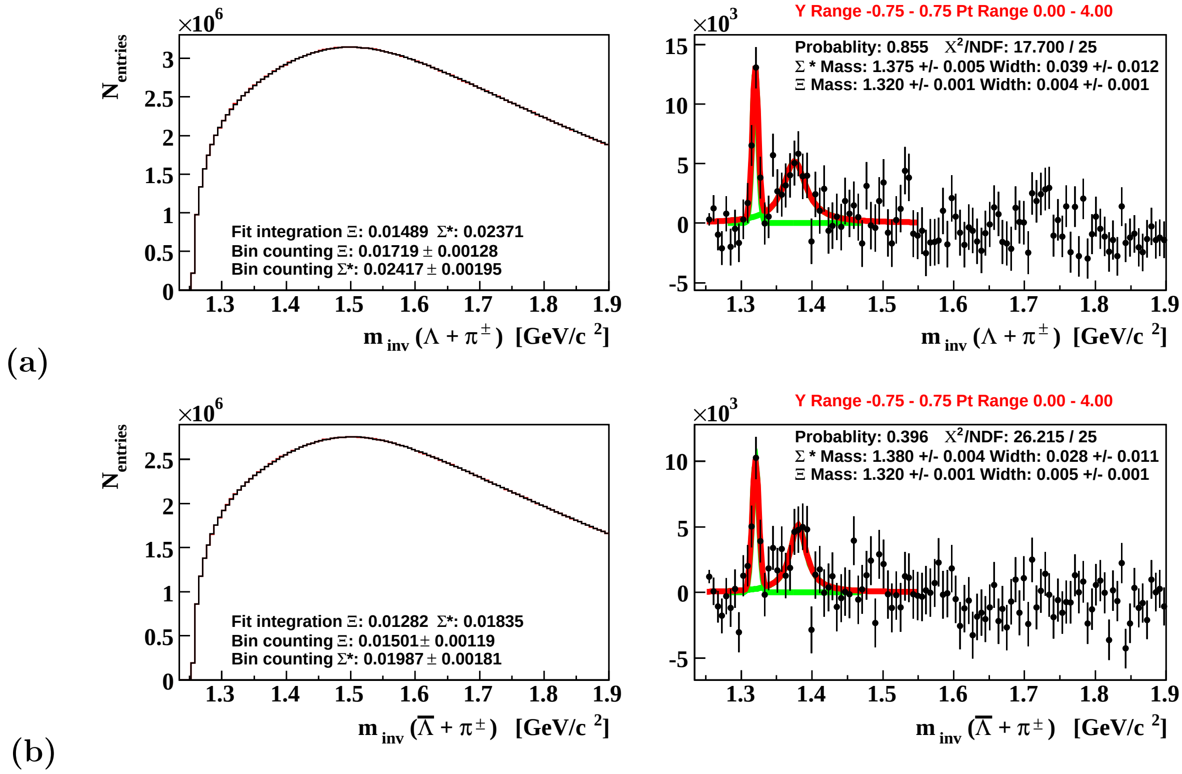

Figure 4.20: Invariant mass spectra (**a**) of the $\Sigma^*(1385)$ and (**b**) $\overline{\Sigma^*}(1385)$ before and after mixed event background subtraction for the $|y| < 0.75$ rapidity range in the 0-5% most central Au+Au collisions. A Gaussian fit for Ξ, Breit-Wigner fit for the $\Sigma^*(1385)$ and a linear fit to the background are shown. The χ^2/DOF, the probabilities of the fits and the raw counts from bin-counting and integration of the fits normalized to the number of events are included in each inset of the plots.

higher multiplicities in events resulting in higher combinatorial backgrounds restricts the $\Sigma^*(1385)$ and $\overline{\Sigma^*}(1385)$ identification. In order to enhance the significance of the signals for Au+Au collisions all four charged states of $\Sigma^*(1385)$ can be added ($\Sigma^*(1385) \equiv \Sigma^{*\pm} + \overline{\Sigma}^{*\pm}$). Figure 4.21 shows the invariant mass spectra of $\Sigma^*(1385)$ before and after mixed event background subtraction for the rapidity range $|y| < 0.75$.

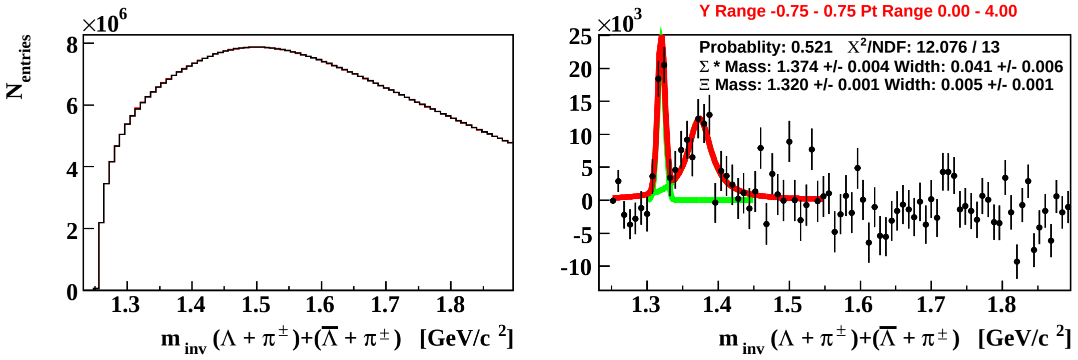

Figure 4.21: Invariant mass spectra of the $\Sigma^*(1385)$ ($\Sigma^*(1385) = \Sigma^{*\pm} + \overline{\Sigma}^{*\pm}$) before and after mixed event background subtraction for the $|y| < 0.75$ rapidity range in the 0-5% most central Au+Au collisions.

4.5.1 Raw $\Sigma^*(1385)$ Yields in the 0-5% Most Central Au+Au Collisions

The $\Sigma^*(1385)$ invariant mass spectrum can be extracted for discrete p_T bins. There are only 5 bins due to the smaller statistics of the Au+Au data set. In Appendix B Figure B.7 and Figure B.8 these 5 p_T bins of the $\Sigma^*(1385)$ invariant mass spectra before and after mixed-event background subtraction are presented. The rapidity coverage of the $\Sigma^*(1385)$ is $|y| < 0.75$ for these invariant mass plots. The p_T ranges of the $\Sigma^*(1385)$ in Figure B.7 are 0.5-1.25, 1.25-1.75, 1.75-2.25 and in Figure B.8 are 2.25-2.75, 2.75-3.5 GeV/c starting from the top figure down to the bottom. Peaks for the Ξ and $\Sigma^*(1385)$ are not visible before the background subtraction in Figure B.7-a due to the higher combinatorial background associated with the larger multiplicity of events. A Gaussian fit for Ξ, Breit-Wigner fit for $\Sigma^*(1385)$ and a linear fit to the background are fit to the background subtracted spectra.

The χ^2/DOF and the probabilities of the fits are included in the insets of the plots. Due to differences in the significance of the Ξ and $\Sigma^*(1385)$ signals, the probabilities of the fits vary.

The 'bin counting' technique described in Section 4.4 is used to estimate the raw yields of the $\Sigma^*(1385)$ baryon. The dependence on $m_T - m_0$ of the raw spectra of the combined $\Sigma^*(1385)$ and $\overline{\Sigma^*}(1385)$ are presented in Figure 4.22 for the 0-5% most

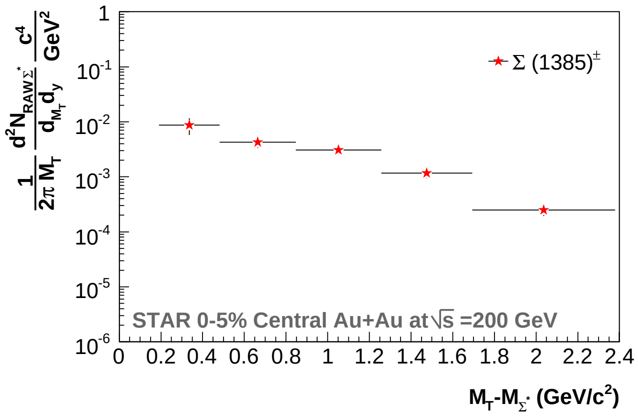

Figure 4.22: The uncorrected transverse mass spectrum of the $\Sigma^*(1385)$ together with the $\overline{\Sigma^*}(1385)$ for the 0-5% most central Au+Au collisions at $\sqrt{s_{NN}}$ = 200 GeV.

central Au+Au collisions. The $\Sigma^*(1385)$ counts together with $\overline{\Sigma^*}(1385)$ are plotted on the y-axis as:

$$\frac{1}{N_{Events}}\frac{1}{2\pi}\frac{1}{\mathrm{m_T}}\frac{1}{\Delta y}\frac{dN}{d\mathrm{m_T}}.$$

4.6 $\Sigma^*(1385)$ Identification in d+Au Collisions

In minimum bias d+Au at $\sqrt{s_{\mathrm{NN}}}$ = 200 GeV collisions, $\Sigma^*(1385)$ and $\overline{\Sigma^*}(1385)$ invariant mass distributions are again reconstructed using the hybrid mixing technique. Table 4.6 shows the cuts applied on the V_0 particles to topologically reconstruct Λ baryons in $\sqrt{s_{\mathrm{NN}}}$ = 200 GeV minimum bias d+Au collisions. Since the multiplicity of d+Au events are between the p+p and Au+Au events, values of the applied cuts are also between those values for p+p and Au+Au. Due to the higher number of events in d+Au collisions, it is possible to apply tighter cuts to identify decay candidates and to extract cleaner $\Sigma^*(1385)$ peaks. Table 4.6 presents the cuts applied to V_0 particles to identify the Λ decay candidates.

Table 4.7 shows the cuts applied to charged particles to identify the possible bachelor π of the $\Sigma^*(1385)$ decay.

Cut Description	Value
DCA of positive daughter to primary vertex [cm]	> 0.9
DCA of negative daughter to primary vertex [cm]	> 2.5
DCA between V_0 and primary vertex [cm]	< 1.1
DCA between daughters [cm]	< 1
Decay length of V_0 [cm]	$5 < L < 30$
Number of hits for positive daughters	> 15
Number of hits for negative daughters	> 15
dE/dx	3 σ
Momentum of p [GeV/c]	> 0.1
Momentum of [GeV/c] π	> 0.1

Table 4.6: Cuts applied for Λ identification in minimum bias d+Au collisions.

Cut Description	Value
Momentum [GeV/c]	$0.15 - 1.5$
Number of Fit Points	> 15
Number of Fit Points/Possible Hit Points	> 0.55
dE/dx	3 σ

Table 4.7: Cuts applied for π identification in minimum bias d+Au collisions.

Figure 4.23 shows the invariant mass spectrum of the Λ baryons and the dE/dx vs. momentum distribution of charged particles and selected π mesons. The Λ decay candidates for the $\Sigma^*(1385)$ reconstruction are selected to have a mass within the range $1.11 - 1.20$ GeV/c^2. Due to the tighter applied cuts, the contamination of K mesons is less visible in the selected π mesons' dE/dx vs. momentum distribution.

Figure 4.24 shows the invariant mass spectra of $\Sigma^*(1385)$ before and after mixed event background subtraction for the $|y| < 0.75$ rapidity range. Like the p+p collisions, in d+Au collisions the signals of Ξ^- and $\Sigma^*(1385)$ are visible before the background subtraction (see the left panels of Figure 4.24). A Gaussian for Ξ and Breit-Wigner for the $\Sigma^*(1385)$ are fit to the mixed event background subtracted invariant mass spectrum.

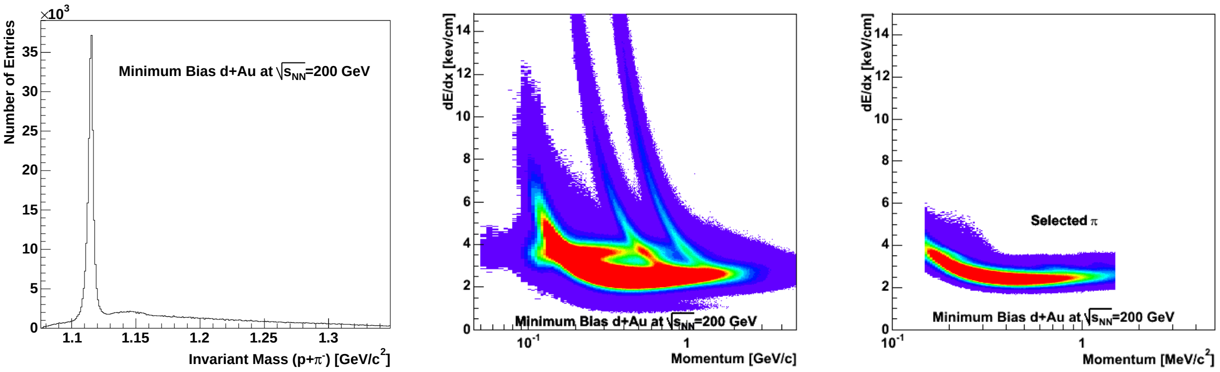

(a) **(b)** **(c)**

Figure 4.23: (**a**) Selected Λ invariant mass distribution after the applied cuts given in Table 4.6. (**b**) dE/dx vs momentum for all tracks before any cuts are applied (**c**) dE/dx vs momentum of accepted π tracks after the cuts given in Table 4.7 are applied. Due to the tight applied cuts, the contamination of electrons and K mesons are not visable in the π meson distribution.

4.6.1 Raw $\Sigma^*(1385)$ Yields in Minimum Bias d+Au Collisions

In d+Au collisions at $\sqrt{s_{\mathrm{NN}}}$ = 200 GeV, it is possible to divide the $\Sigma^*(1385)$ and $\overline{\Sigma^*}(1385)$ invariant mass spectrum into 8 discrete $\mathrm{p_T}$ bins. As in the cases of p+p and Au+Au collisions, this is required due to the differences in the correction factors of efficiency and acceptance. The first 3 $\mathrm{p_T}$ bins of the $\Sigma^*(1385)$ invariant mass spectra before and after mixed-event background subtraction are presented in Appendix B Figure B.9. While the rapidity coverage for $\Sigma^*(1385)$ is $|y| < 0.75$ for all plots in Figure B.9, the $\mathrm{p_T}$ ranges are 0.25-1, 1-1.25 and 1.25-1.5 GeV/c starting from the top to bottom. Signals of the Ξ and $\Sigma^*(1385)$ are visible even before the background subtraction in Figure B.9-a. A Gaussian for Ξ and a Breit-Wigner for the $\Sigma^*(1385)$ are fit to the background subtracted spectra. The raw yields from bin counting and the integration of the fit for Ξ and $\Sigma^*(1385)$ are given in the insets of the plots. In Figure B.10 and Figure B.11, the invariant mass spectra of $\Sigma^*(1385)$ for the rest of the $\mathrm{p_T}$ bins with the ranges of 1.5-1.75, 1.75-2.0, 2.0-2.25, 2.25-2.5, 2.5-2.75 and 2.75-3.5 GeV/c are presented. $\overline{\Sigma^*}(1385)$ invariant mass spectra for discrete $\mathrm{p_T}$ ranges identical to those for the $\Sigma^*(1385)$ in the rapidity range $|y| < 0.75$ are presented in Figure B.12, Figure B.13 and Figure B.14.

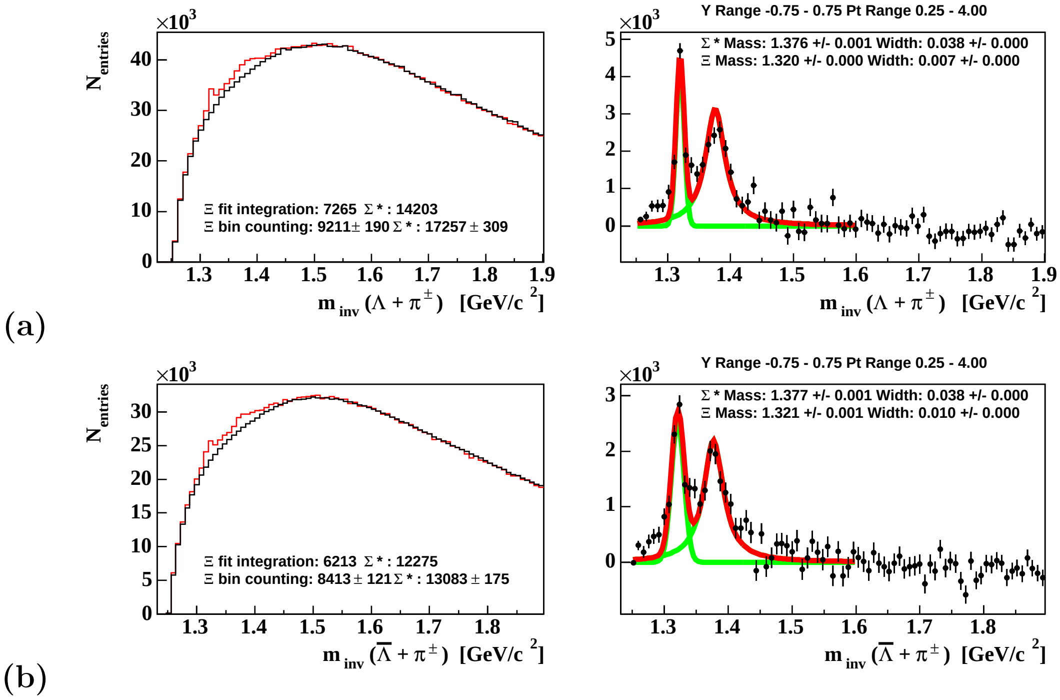

Figure 4.24: Invariant mass spectra of (**a**) the $\Sigma^*(1385)$ before and after mixed event background subtraction and (**b**) the $\overline{\Sigma^*}(1385)$ for the $|y| < 0.75$ rapidity range in minimum bias d+Au collisions. A Gaussian for Ξ, Breit-Wigner for the $\Sigma^*(1385)$ are fit to the spectra.

The raw counts of yields are extracted using the bin counting technique. The signal region for the $\Sigma^*(1385)$ (1.33-1.40 GeV/c^2) is chosen as discussed previously for the p+p and Au+Au collision environments. The dependence of the raw spectra of the $\Sigma^*(1385)$ and $\overline{\Sigma^*}(1385)$ on $\mathrm{m_T}-\mathrm{m_0}$ in minimum bias d+Au collisions are presented in Figure 4.25. The $\Sigma^*(1385)$ and $\overline{\Sigma^*}(1385)$ counts are plotted on the y-axis as:

$$\frac{1}{N_{Events}}\frac{1}{2\pi}\frac{1}{\mathrm{m_T}}\frac{1}{\Delta y}\frac{dN}{d\mathrm{m_T}}.$$

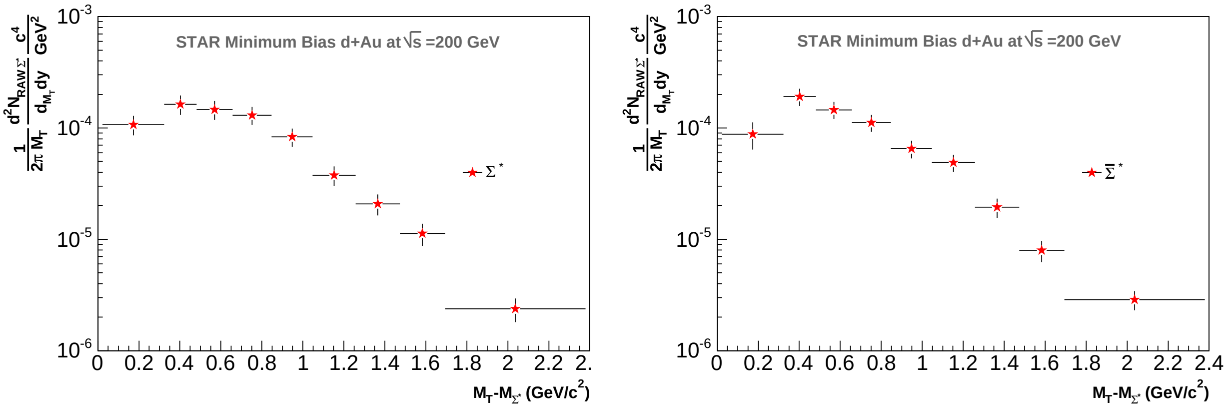

(a) **(b)**

Figure 4.25: (**a**) The uncorrected transverse mass spectrum of the $\Sigma^*(1385)$ baryon and (**b**) the $\overline{\Sigma^*}(1385)$ baryon in minimum bias d+Au collisions at $\sqrt{s} = 200$ GeV.

Chapter 5

Simulations

The Monte Carlo (MC) simulation studies are needed to address three main issues. The first is to investigate the correlated backgrounds that cannot be described by the mixed-event technique. The second is to optimize the cuts on the decay particles so that the identification of the resonances is feasible in high combinatorial events. The third is to estimate the detector acceptance and the reconstruction efficiency for each particle. This chapter discusses each of these simulation studies in turn.

5.1 Monte Carlo Studies

Pure Monte Carlo (MC) studies without the detector distortion effects were performed to investigate the correlated signals observed around the kinematic cutoff region in the invariant mass spectra of the $\Sigma^*(1385)$ with the TPM technique. The 3-dimensional momentum distributions of the $\Sigma^*(1385)$ decay particles are chosen, starting from a random seed, with the specified rapidity range and the T parameter of a thermal exponential momentum distribution.

The approximate momentum of the particle decays can be studied using MC techniques for decays of particles. To increase the significance of the signal, the $\mathrm{p_T}$ distribution of the MC decay tracks is investigated. In this section the MC studies used to investigate and tune the cuts when selecting the decay particles are discussed.

5.1.1 The $\Sigma^*(1385)$ Background Studies

Misidentification of decay particles might cause the population observed above background near the kinematic cutoff in the invariant mass distribution of the $\Sigma^*(1385)$ baryon (See Figure 5.2-b). We hypothesize that some of the contribution is due to misidentification of the Λ. Figure 5.1 represents a schematic diagram of the decay and correlated background contribution of the $\Sigma^*(1385)$ due to a misidentified π_{bachelor}. To distinguish the two π mesons of the decay we call the first π coming directly from the decay of the $\Sigma^*(1385)$, the π_{bachelor}, and the second π which is the decay product of the Λ, the π_{daughter}. As discussed in the previous chapter, we first must identify the π_{bachelor} and the Λ and then calculate the invariant mass distribution of the $\Sigma^*(1385)$ baryon. If the π_{daughter} is interchanged with the π_{bachelor}, it is possible to reconstruct a Λ_{False} and then use this Λ_{False} with the π_{daughter} to reconstruct a false $\Sigma^*(1385)$. This will contribute an additional correlation in the invariant mass spectrum of the $\Sigma^*(1385)$ that cannot be subtracted using a mixed event background. To quantify these contributions, Monte Carlo $\Sigma^*(1385)$ baryons are generated and the invariant mass distributions are calculated for the mis-identification of Λ_{False}.

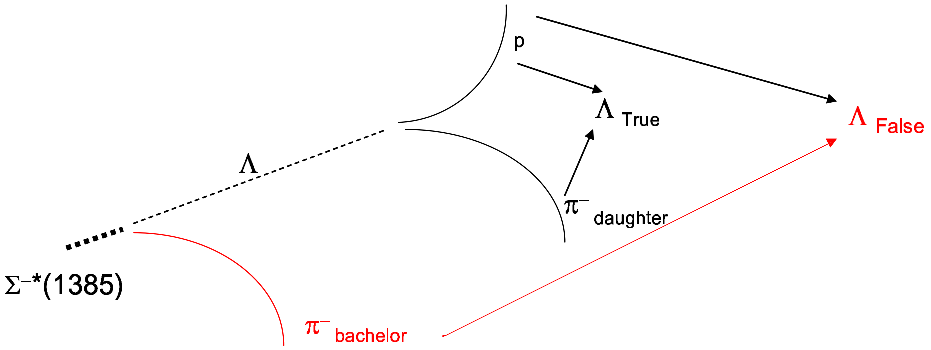

Figure 5.1: Schematic representation of the correlated background contribution of the $\Sigma^*(1385)$. To distinguish the two π mesons of the decay we call the first π coming directly from the decay of the $\Sigma^*(1385)$, the π_{bachelor}, and the second π that is the decay product of the Λ, the π_{daughter}. Correct $\Sigma^*(1385)$ identification can be achieved when Λ_{True} and π_{bachelor} are used for invariant mass calculation of $\Sigma^*(1385)$.

Figure 5.2-a represents the invariant mass spectrum of the Monte Carlo simulated

$\Sigma^*(1385)$ for the true and false mass signals. The red curve is for the $\Sigma^*(1385)$ spectrum that is calculated from Λ_{True} and π_{bachelor} while the blue curve is the calculation from Λ_{False} and π_{daughter}. The background subtracted invariant mass spectrum of the $\Sigma^*(1385)$ is presented in Figure 5.2-b. The location of the population near the kinematic cutoff of the real signal is comparable with the one from the simulation (blue curve in Figure 5.2-a). The narrow signal due to false $\Sigma^*(1385)$ identification can explain the population above the background near the kinematic cutoff but to estimate the contribution quantitatively, cuts need to be applied to the falsely reconstructed $\Sigma^*(1385)$ signal.

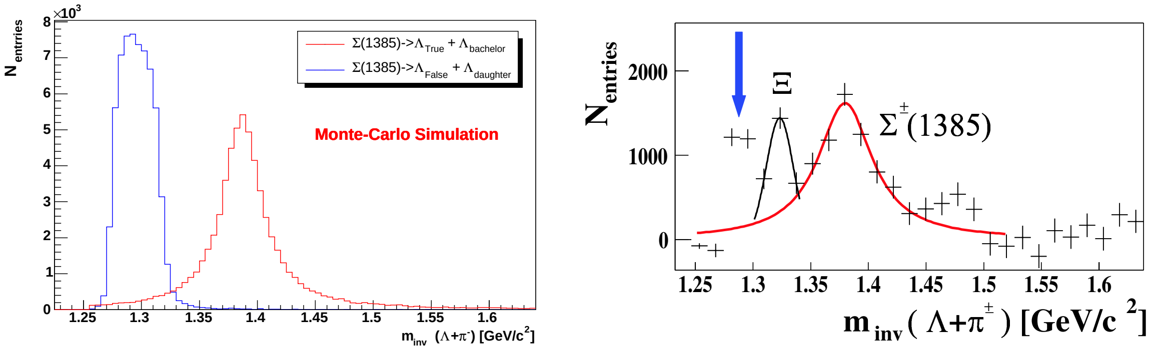

(a) **(b)**

Figure 5.2: (**a**) Monte-Carlo study of correlated background contribution to the $\Sigma^*(1385)$ in blue and MC input of the $\Sigma^*(1385)$ invariant mass spectrum in red. (**b**) The invariant mass spectrum of the $\Sigma^*(1385)$ in p+p collisions using the TPM technique. The location of the population near the kinematic cut off shown with a blue arrow in real data is comparable to the misidentified $\Sigma^*(1385)$ from π_{daughter} and Λ_{False}.

During the data analysis, in order to enhance the significance of the $\Sigma^*(1385)$ signal, cuts are applied to the possible decay candidates. Figure 5.3-a shows the invariant mass distribution of the misidentified Λ distribution. Figure 5.3-b shows the simulated invariant mass distribution of correct (in red) and false $\Sigma^*(1385)$ signals before (in blue) and after (in black) the applied cuts. The applied cut on the Λ mass range of $1.11 - 1.12$ GeV/c^2, due to the broadening of the width of Λ when falsely identified, causes a contamination of only $\sim 1\%$ of the reconstructed $\Sigma^*(1385)$ baryons. This small amount alone is insufficient to explain the full strength of the

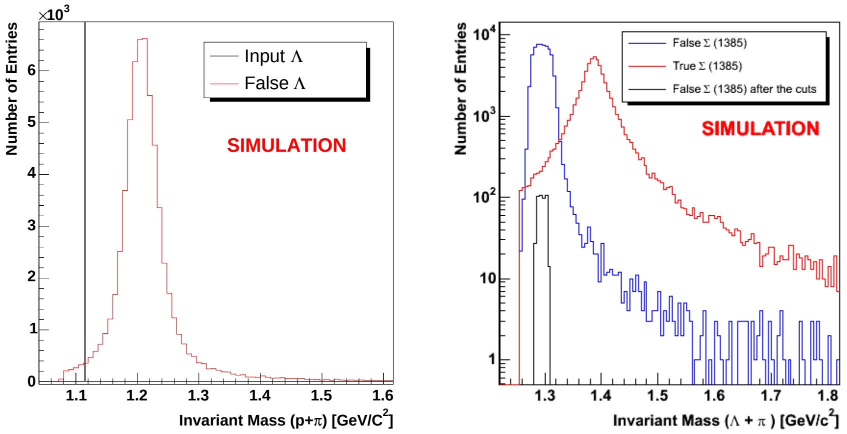

(**a**) (**b**)

Figure 5.3: (**a**) The invariant mass spectrum of input Monte-Carlo and falsely reconstructed Λ. The Λ width broadens due to the wrong π choice. (**b**) Monte-Carlo study of the correlated background contribution to the $\Sigma^*(1385)$ after momentum and mass cuts are applied. During the data analysis, the $1.11 - 1.12$ GeV/c^2 mass range is selected for the reconstructed Λ, and the contamination due to mixed π is of the order of 1% with the cuts in the kinematic cut off region.

signal.

Figure 5.4 represents schematically the decay of the Ω baryon. Similar to the $\Sigma^*(1385)$, the Ω baryon decays into three particles and most importantly both the $\Sigma^*(1385)$ and Ω baryons share the same decay particle, the Λ baryon. The Ω baryon decay provides another source of correlated background due to the misidentification of K mesons as π mesons. Since the dE/dx bands for π and K mesons start to merge at momenta above 700 MeV/c there is a contamination in π mesons from K mesons for momentum higher than 700 MeV/c.

Due to contamination of π mesons from K mesons, it is possible to calculate a false invariant mass distribution for Ω baryons that causes an additional correlated signal that cannot be subtracted using the mixed event background in the $\Sigma^*(1385)$ invariant mass spectrum. Figure 5.5 shows the invariant mass spectrum of Monte Carlo produced Ω baryons as black curves and corresponding falsely reconstructed Ω baryons. Due to the weak decay of the Ω, the correct invariant mass spectrum without detector resolution effects produces a delta function. To show the details of the falsely

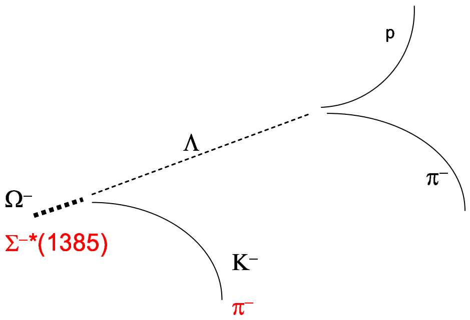

Figure 5.4: Schematic representation of Ω decay in comparison to Σ(1385) decay. While the $\Sigma^*(1385)$ decays into a π and a Λ, Ω decays into a K and a Λ.

reconstructed Ω signals, the magnitude of the correct Ω signal is suppressed. If K mesons are misidentified as π mesons, these particles will be assigned the mass of a π meson (137 MeV instead of 493 MeV). The smaller mass causes a shift in the invariant mass calculations as can be seen with the red curve in Figure 5.5. An additional contamination that can be seen in the $\Sigma^*(1385)$ invariant mass spectrum (blue curve) is caused by the false identification of the Ω from the combination of a misidentified $\Lambda \rightarrow \pi_{\mathrm{misidentified}} + \mathrm{p}$ and a misidentified π from the Λ decay as the bachelor π. The blue curve represents the wider population in the invariant mass spectrum due to these mixed and misidentified K mesons. There is also another but smaller population at 1.47 GeV/c mass in the invariant mass distribution of the $\Sigma^*(1385)$ shown in Figure 5.2-b. The blue curve due to misidentified and mixed K mesons can explain this second peak since it also peaks at 1.47 GeV/c. The overall contribution of misidentified Ω baryons in the invariant mass distribution of the $\Sigma^*(1385)$ depends on the yield of Ω baryons that are produced in our collision systems.

The kinematic cut off population is correlated with the multiplicities of events. In Au+Au collisions where the multiplicities are high the population cannot be fully described with only falsely reconstructed $\Sigma^*(1385)$ or misidentified Ω baryons since there are only 0.53 ± 0.05 $\Omega + \bar{\Omega}$ baryons per Au+Au event. The contribution is not fully understood for these higher multiplicities. The HMT was introduced as an

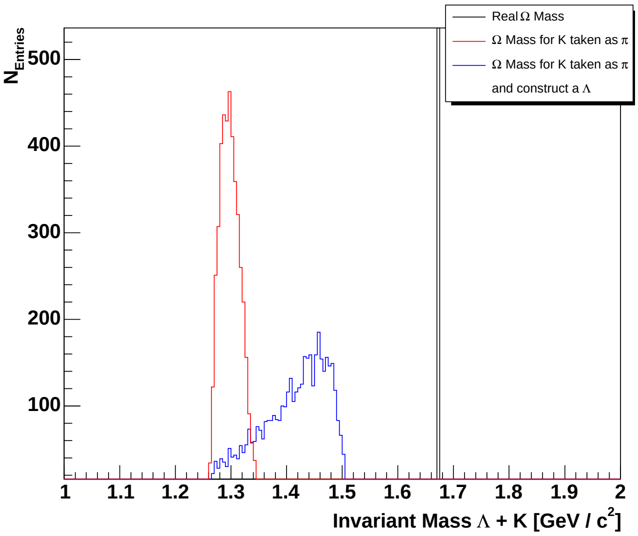

Figure 5.5: Monte-Carlo study of correlated background contribution of Ω in the Λ+π due to misidentified K. The black histogram is for simulated real invariant mass of Ω. The red histogram is the invariant mass of the misidentified Ω through misidentified Kaons as pions. The blue histogram is the invariant mass spectrum due to mixed and misidentified Kaons. See text for details.

improved technique to clean up the Λ baryon identification and to minimize the correlated misidentification that cannot be subtracted using the mixed event background in the invariant mass spectrum of the $\Sigma^*(1385)$.

5.2 The Effect of Applied Cuts

Simulated MC $\Sigma^*(1385)$ decays are also used to investigate the effects of applied cuts. Monte Carlo simulated $\Sigma^*(1385)$ baryons are produced with a thermal exponential distribution at T = 350 MeV and a flat rapidity interval $| y |< 1.2$. The transverse momentum distribution of the simulated $\Sigma^*(1385)$ is presented as the black curve in Figure 5.6-a. The $\Sigma^*(1385)$ baryon decays asymmetrically into a heavy Λ baryon and a light π meson. The transverse momentum distribution of the decay products, π and Λ, is also shown in Figure 5.6-a with blue and red curves, respectively. For soft $\Sigma^*(1385)$ baryons ($p_T < 4$ GeV/c), a momentum cut on the π above 1 GeV/c causes negligible $\Sigma^*(1385)$ signal loss.

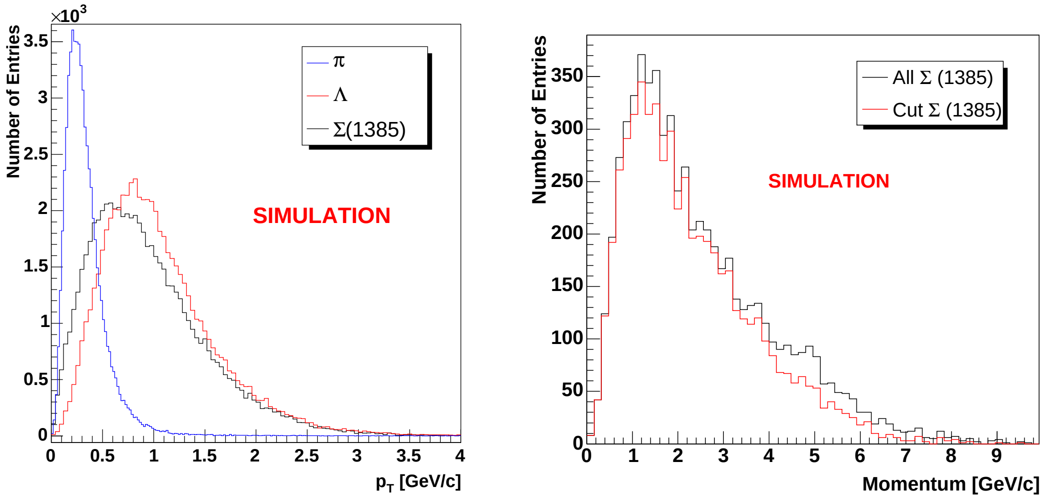

(a) **(b)**

Figure 5.6: (**a**) Transverse momentum distribution of MC simulated $\Sigma^*(1385)$ baryons (black curve) and the decay products (blue curve for π and red curve for Λ). Most of the $\mathrm{p_T}$ of the $\Sigma^*(1385)$ is transferred to the Λ. (**b**) The momentum distribution of simulated $\Sigma^*(1385)$ without cuts on the bachelor π momentum (black curve) and with a momentum cut $0.1 < \mathrm{p_T} < 1.2$ GeV/c on the π (red curve).

The effect on the identified $\Sigma^*(1385)$ from the applied cut on the momentum of the bachelor π can be seen in Figure 5.6-b. The applied cut affects the higher momentum region of the $\Sigma^*(1385)$ baryon ($\mathrm{P}(\Sigma^*(1385)) > 4$ GeV/c) significantly.

5.3 Acceptance and Efficiency Corrections

The raw counts of $\Sigma^*(1385)$ measured and presented in Chapter 4 must be corrected to measure the yields produced in the collision. There are two main correction factors necessary: acceptance and efficiency. The acceptance correction accounts for the geometrical coverage of the detectors and the efficiency correction accounts for both the efficiency of detecting particles in the detector and the reconstruction efficiency of the software. For example, a charged particle can be undetected if it does not deposit sufficient energy in the sensitive volume of the TPC, if it decays in flight before it reaches the detector or if it fails one of the cuts imposed. Due to the topological cuts that are applied on the V_0 particles, in order to make any comparisons between the TPM and HMT, acceptance corrections are folded into the efficiency corrections.

The efficiency correction for the $\Sigma^*(1385)$ can be calculated as the ratio of the number of particles that pass the geometrical cuts to the number that are produced. For this study, Monte Carlo simulated $\Sigma^*(1385)$ baryons are produced with a thermal exponential distribution at T = 350 MeV over a flat rapidity interval $\mid y \mid < 1.2$. The simulated decay of the $\Sigma^*(1385)$ is passed to the detector simulation package to calculate how the particles interact in the detector materials and to simulate the response of detector elements, and then embedded in real p+p events to calculate the efficiency. In Figure 5.7 the invariant mass spectra of the MC simulated $\Sigma^*(1385)$ input and the corresponding $\Sigma^*(1385)$ reconstructed via the TPM technique are presented. The p_T integrated efficiency and acceptance of the $\Sigma^*(1385)$ is calculated to be $15 \pm 4\%$.

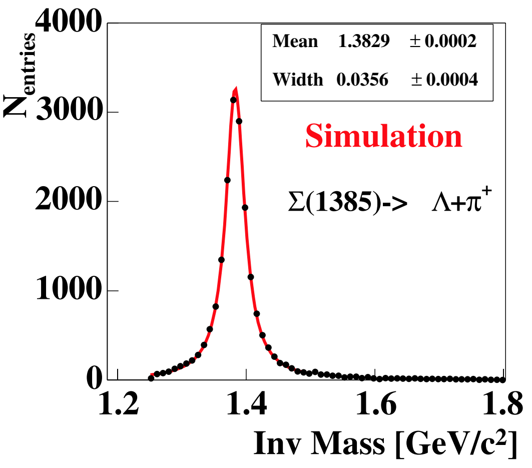

(a) (b)

Figure 5.7: (**a**) The invariant mass spectrum of the input MC simulated $\Sigma^*(1385)$ that are embedded in real p+p events and (**b**) the reconstructed invariant mass spectrum of the $\Sigma^*(1385)$ via TPM.

To make further comparisons of the TPM and HMT techniques, the invariant mass spectra of the $\Sigma^*(1385)$ is presented in Figure 5.8 for the input MC and the reconstructed $\Sigma^*(1385)$ with the HMT technique before and after mixed event background subtraction. With the bin-counting technique, the efficiency is calculated as $6.4 \pm 2.5\%$.

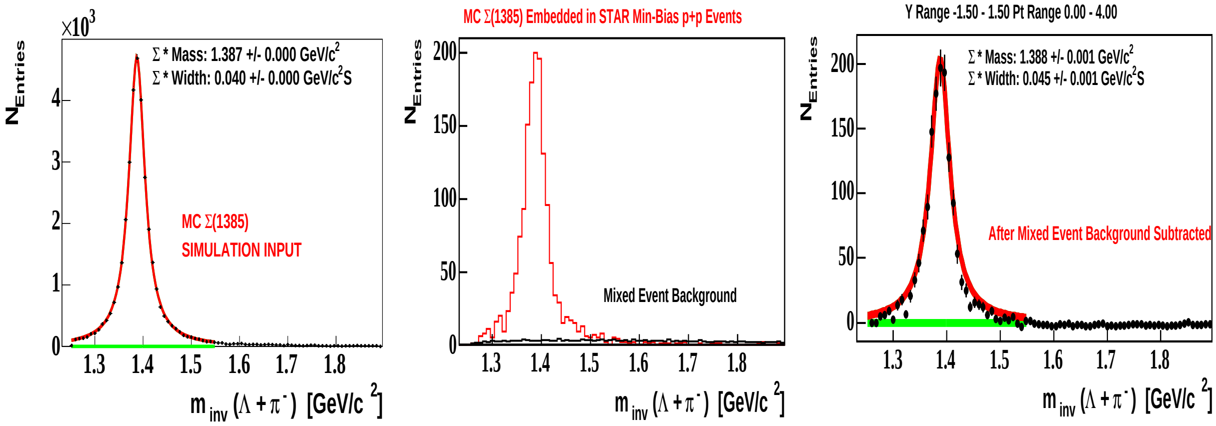

(a) (b) (c)

Figure 5.8: (**a**) The invariant mass spectra of the Monte-Carlo input $\Sigma^*(1385)$, (**b**) the reconstructed invariant mass spectra of the $\Sigma^*(1385)$ embedded in STAR minimum bias p+p events in red and mixed event background in black and (**c**) the mixed event background subtracted invariant mass spectrum.

The efficiency is twice as high for the TPM than HMT, that is why initially the TPM was used to reconstruct the $\Sigma^*(1385)$ in p+p events. However, due to the correlated backgrounds in the kinematic cutoff region that cannot be subtracted using the mixed event background in the TPM, HMT was developed and used to obtain the final results in the previous chapter.

5.3.1 p+p Collisions

Efficiency corrections vary as a function of the $y - p_T$ phase space distribution of particles emitted in the collision. The efficiency correction for the spectra is calculated by embedding Monte-Carlo simulated $\Sigma^*(1385)$ decays into real minimum bias p+p collisions. The tracking of particles depends on the multiplicities of the events. With embedding, since real events are used, it is possible to simulate the tracking of the

MC particles more realistically. The embedding is performed by simulating the hits and ionization of the Monte-Carlo tracks.

The events used for the embedding are carefully selected to represent the actual collision dynamics such as where the collision occurs and the multiplicity of the events. Figure 5.9 shows the Z vertex position and reference multiplicity of all accepted p+p events (in black) in comparison to events used for the embedding data (in red). The distributions of reference multiplicities and the primary vertex of selected events for the embedding are similar to the ones for the actual full p+p data set.

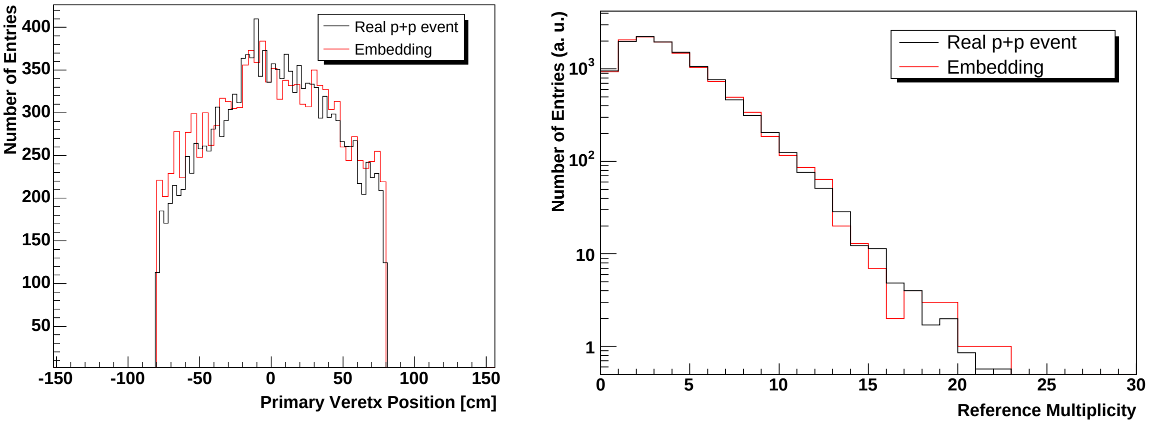

(a) (b)

Figure 5.9: (**a**) Primary vertex position and (**b**) reference multiplicity of accepted p+p events in comparison to events used for the embedding data. The black histogram is for all accepted p+p events and red histogram is for selected events.

To calculate the correction factors, all cuts that are applied on the real data need to be applied to the embedding data. First, event selection cuts described in Chapter 4 for the p+p events are applied to the embedding data. Then the embedded tracks of the selected events are associated with the MC tracks, and decay particle identification cuts (except the σ dE/dx cuts) are applied. The widths of the Gaussian distribution for the dE/dx measurement cannot be represented accurately with the embedding tracks. It is possible to correct the spectra later with a multiplication factor that is the percentage area of the tails of the Gaussian distribution.

Figure 5.10 shows rapidity and p_T dependence of the $\Sigma^*(1385)$ efficiency in p+p

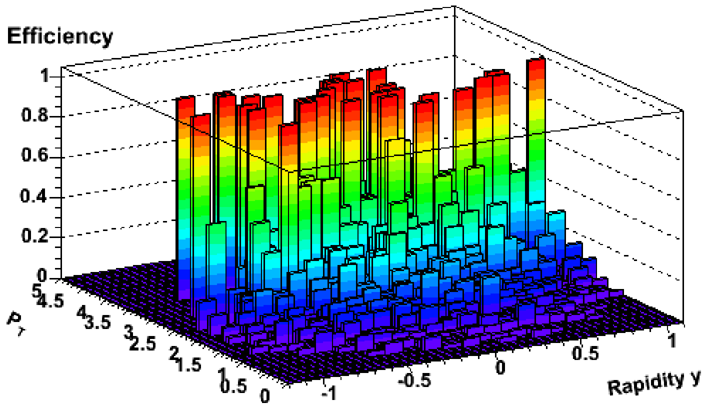

Figure 5.10: The rapidity and p_T dependence of the $\Sigma^*(1385)$ efficiency in minimum bias p+p collisions.

collisions. Since the rapidity dependence of the $\Sigma^*(1385)$ efficiency is flat for the $|y| < 0.75$ range, the correction factors are calculated for the $\mathrm{p_T}$ bins in this rapidity range. In real data, in order to increase the significance of the signals of the $\Sigma^*(1385)$

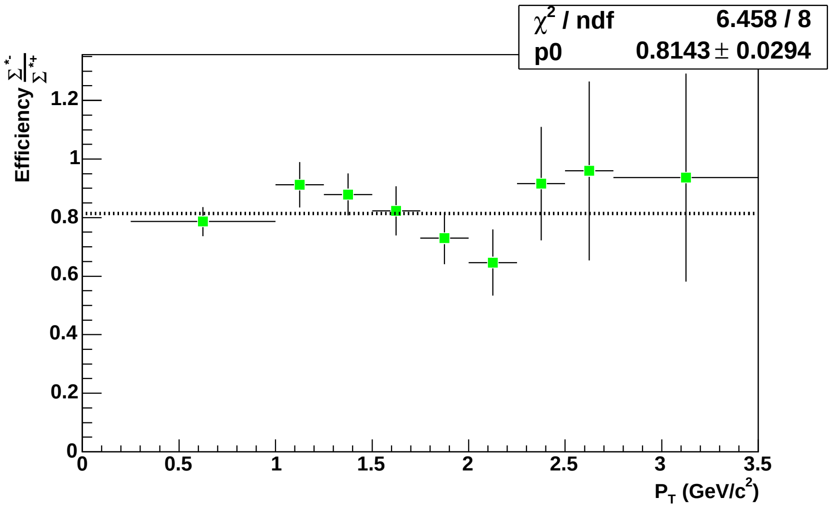

Figure 5.11: The $\mathrm{p_T}$ dependence of the ratio of efficiency calculations for $\Sigma^+(1385)$ and $\Sigma^-(1385)$ in p+p collisions. The dashed line is an empirical line to parameterize the ratio.

both $\Sigma^+(1385) \rightarrow \Lambda + \pi^+$ and $\Sigma^-(1385) \rightarrow \Lambda + \pi^-$ are added. Due to the differences in the efficiency calculations presented in Figure 5.11, identical numbers of $\Sigma^+(1385)$ and $\Sigma^-(1385)$ are embedded separately into the events to calculate the efficiency.

The $\mathrm{m_T} - \mathrm{m_0}$ dependence of efficiency and acceptance correction factors of the two charged states of $\Sigma^*(1385)$ for the minimum bias p+p collisions in the rapidity range $|y| < 0.75$ is presented in Figure 5.12.

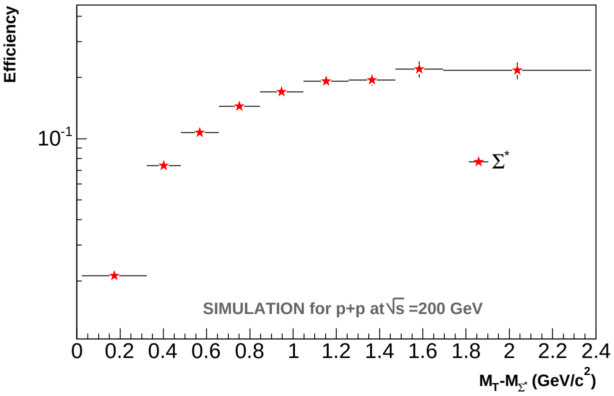

Figure 5.12: $\mathrm{m_T} - \mathrm{m_0}$ dependence of efficiency correction factors of the two charged states of $\Sigma^*(1385)$ for the minimum bias p+p collisions.

5.3.2 Au+Au Collisions

We can repeat the same study for the Au+Au most central collisions and calculate the efficiency and acceptance of our measurement. For this study the MC simulated $\Sigma^*(1385)$ baryons are embedded in real Au+Au events. The event selection cuts such as reference multiplicity are applied to select the 0-5% most central Au+Au collisions (See Chapter 4 for details). All the cuts except the dE/dx cut on the decay particle candidates are applied to the associated tracks.

Figure 5.13 shows the rapidity and $\mathrm{p_T}$ dependence of the $\Sigma^*(1385)$ efficiency and acceptance in the 0-5% most central Au+Au collisions. Since the rapidity dependence of the $\Sigma^*(1385)$ efficiency is mostly flat for the $|y| < 0.75$ range, the correction factors are calculated by only varying $\mathrm{p_T}$ bins within a $|y| < 0.75$ rapidity range. In

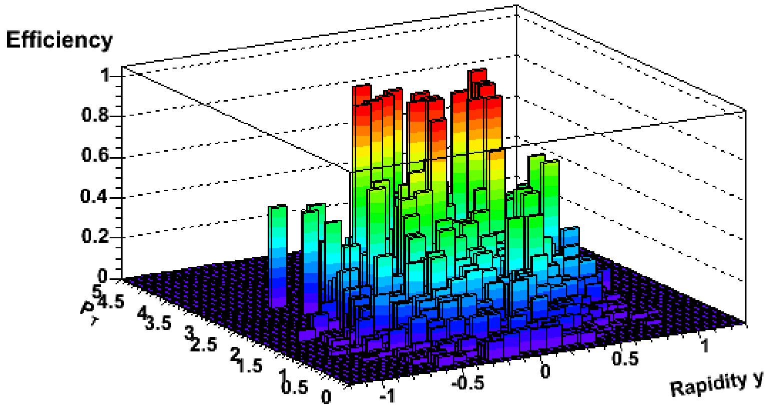

Figure 5.13: The rapidity and p_T dependence of the $\Sigma^*(1385)$ efficiency in the 0-5% most central Au+Au collisions.

Figure 5.14, the $\mathrm{m_T}-\mathrm{m_0}$ dependence of the efficiency correction values of $\Sigma^*(1385)$ for the $|y| < 0.75$ rapidity range in the 0-5% most central Au+Au collisions is presented.

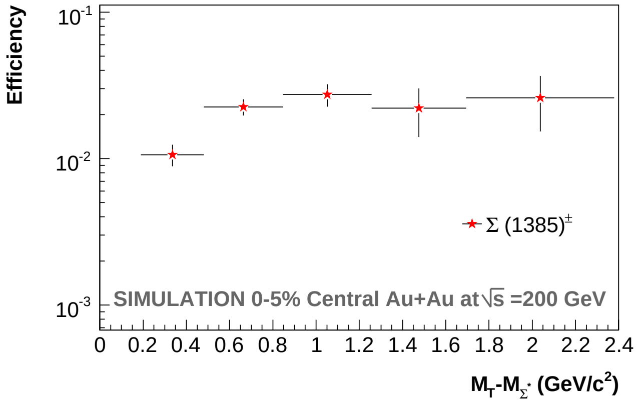

Figure 5.14: The $\mathrm{m_T} - \mathrm{m_0}$ dependence of efficiency of the two charge states of the $\Sigma^*(1385)$ in the 0-5% most central Au+Au collisions.

5.3.3 d+Au Collisions

Similar to p+p and Au+Au collisions, the efficiency is calculated with the MC simulated $\Sigma^*(1385)$ decays embedded in d+Au collisions. The $\mathrm{m_T} - \mathrm{m_0}$ dependence of efficiency of the two charged states of $\Sigma^*(1385)$ in minimum bias d+Au collisions is presented in Figure 5.15.

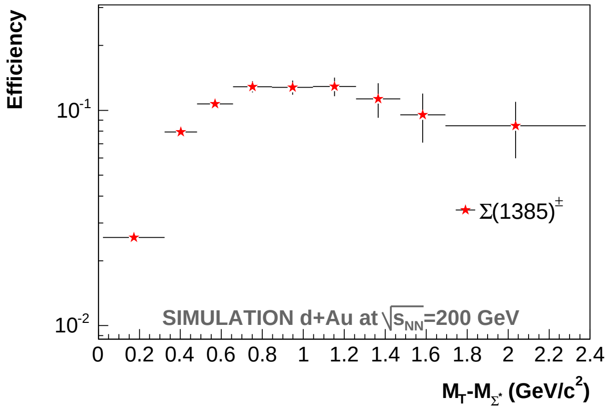

Figure 5.15: The $\mathrm{m_T} - \mathrm{m_0}$ dependence of efficiency of the two charge states of the $\Sigma^*(1385)$ in minimum bias d+Au collisions.

5.3.4 Total Correction

The raw yields are corrected with both acceptance and efficiency corrections presented in the previous sections for all three collision systems. In addition, branching ratios and the dE/dx cut applied in real data need to be corrected to calculate the total true yield of $\Sigma^*(1385)$. In order to minimize the disk space requirements for the embedding data, all the branching ratios were set to 100%. This affects the correction factor of the $\Sigma^*(1385)$ and the Λ and needs to be included in the correction factor. (The branching ratios are 88% and 64% for $\Sigma^*(1385)$ and Λ, respectively.) The applied dE/dx cut is 3σ of the Gaussian distribution of the π band to select the $\pi_{bachelor}$. A 3σ cut, cuts out 0.27% of the Gaussian distribution [39]. A 5σ cut applied on the decay particles of Λ, cuts out only 5.7×10^{-5}% of the Gaussian distribution, which is negligible.

For each $\mathrm{p_T}$, the raw yields are multiplied by

$$\frac{1}{Efficiency} \times \frac{1}{0.88} \times \frac{1}{0.64} \times 1.0027. \tag{5.1}$$

Since the rapidity range is chosen as $|y| < 0.75$, to calculate per unit rapidity the corrected values are divided by 1.5.

Chapter 6

Experimental Findings

The corrected $\Sigma^*(1385)$ and $\overline{\Sigma^*}(1385)$ spectra in p+p, Au+Au and d+Au collisions at $\sqrt{s_{\mathrm{NN}}} = 200$ GeV collisions are presented in this chapter. The $\Sigma^*(1385)$ baryon yields and $\langle p_T \rangle$ dependence are extracted from the corrected spectra for various collision systems. Antiparticle to particle ratios are shown. The $\mathrm{p_T}$ dependent nuclear affects are discussed in terms of the nuclear modification factor for $\Sigma^*(1385)$ in d+Au and Au+Au collisions.

6.1 p+p Results for $\Sigma^*(1385)$

Ξ and $\Sigma^*(1385)$ baryons are fit with Gaussian and Breit-Wigner distributions as described in Chapter 4. The fit parameters, mass and width with statistical and systematic uncertainties are presented in Table 6.1 for Ξ^-, $\Sigma^*(1385)$ and their antiparticles for the $\mathrm{p_T}$ and rapidity ranges given in p+p collisions at $\sqrt{s_{\mathrm{NN}}} = 200$ GeV. The masses and widths are in agreement with the known Particle Data Group values within our detector resolution in minimum bias p+p collisions at $\sqrt{s_{\mathrm{NN}}}$=200 GeV [39].

For each individual $\mathrm{p_T}$ and rapidity bin presented in Appendix B, the Gaussian and Breit-Wigner summed distributions have 5 free fit parameters. These parameters are the amplitude, the width and the mass of the Gaussian peak of Ξ^- and the amplitude and the mass of the Breit-Wigner peak of $\Sigma^*(1385)$. Since the width of the Breit-Wigner peak is in agreement with the PDG value for the summed signal presented in Table 6.1, the width is fixed to 38 MeV/c^2 for each p_T and y plot due to limited statistics which cause the free parameter fit to fail. The Table 6.2 presents the mass parameters for the $\Sigma^*(1385)$ Breit-Wigner fits of each p_T and y plot.

Table 6.1: Mass and width fit parameters of Ξ^-, $\Sigma^*(1385)$ and their antiparticles from minimum bias p+p collisions including statistical and systematic errors for given p_T and rapidity y.

Particle	m [MeV/c^2]	Γ [MeV/c^2]	p_T [GeV/c]	$\lvert \mathbf{y} \rvert$
Ξ^-	$1320 \pm 1 \pm 1$	$7 \pm 1 \pm 1$	0.25 – 4.00	≤ 0.75
$\bar{\Xi}^+$	$1320 \pm 1 \pm 1$	$7 \pm 1 \pm 1$	0.25 – 4.00	≤ 0.75
Σ^*	$1376 \pm 3 \pm 3$	$44 \pm 8 \pm 8$	0.25 – 4.00	≤ 0.75
$\bar{\Sigma}^*$	$1374 \pm 4 \pm 3$	$53 \pm 14 \pm 8$	0.25 – 4.00	≤ 0.75

Table 6.2: The masses from the Breit-Wigner fits for the $\Sigma^*(1385)$ and their antiparticles from minimum bias p+p collisions at mid rapidity $|y| < 0.75$, including statistical and systematic errors for the p_T ranges given.

p_T [GeV/c]	$\Sigma^*(1385)$ Mass [MeV/c^2]	$\overline{\Sigma^*}(1385)$ Mass [MeV/c^2]
0.25–1.00	$1377 \pm 6 \pm 7$	$1404 \pm 4 \pm 7$
1.00–1.25	$1381 \pm 4 \pm 3$	$1355 \pm 9 \pm 3$
1.25–1.50	$1373 \pm 5 \pm 3$	$1377 \pm 4 \pm 3$
1.50–1.75	$1378 \pm 5 \pm 3$	$1378 \pm 4 \pm 3$
1.75–2.00	$1377 \pm 4 \pm 3$	$1371 \pm 4 \pm 3$
2.00–2.25	$1382 \pm 4 \pm 3$	$1380 \pm 6 \pm 3$
2.25–2.50	$1375 \pm 7 \pm 3$	$1381 \pm 12 \pm 3$
2.50–2.75	$1384 \pm 6 \pm 4$	$1376 \pm 10 \pm 4$
2.75–3.50	$1385 \pm 5 \pm 2$	$1381 \pm 8 \pm 7$

The raw yields of the $\Sigma^*(1385)$ and $\overline{\Sigma^*}(1385)$ presented in Chapter 4 are corrected with the efficiency and other corrections described in Chapter 5. In Section 2.4.1 the motivation for an exponential fit function is given and the function was introduced as

$$\frac{\mathrm{d^2N}}{2\pi \mathrm{m_T dy dm_T}} = \frac{\mathrm{dN/dy}}{2\pi \mathrm{T}(m_0 + \mathrm{T})} \mathrm{e}^{-\frac{(\mathrm{m_T} - m_0)}{\mathrm{T}}} . \tag{6.1}$$

Since the $\Sigma^*(1385)$ yield (dN/dy) and the inverse slope parameter, T, are the two free parameters in this fit function, the yield can be obtained directly as the fit parameter from the fit. Corrected $\mathrm{m_T} - \mathrm{m_0}$ spectra normalized to unit rapidity are presented in Figure 6.1 for the $\Sigma^*(1385)$ (closed circles) and $\overline{\Sigma^*}(1385)$ (open circles) in minimum bias p+p collisions at $\sqrt{s_{\rm NN}}$=200 GeV. The error bars presented correspond to statistical uncertainties. The systematic uncertainty, which is not included in the error bars, is estimated mainly from variation of the cuts and normalization of the background and discussed further in Appendix C. The dashed lines in Figure 6.1 represent exponential fits (Equation 6.1) to the data. The $\overline{\Sigma^*}(1385)$ is scaled by 0.5 to separate the $\Sigma^*(1385)$ and $\overline{\Sigma^*}(1385)$ bins and the exponential fits.

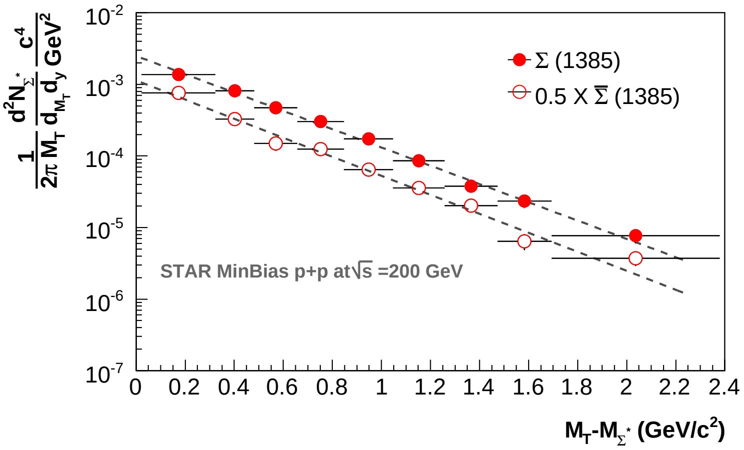

Figure 6.1: The transverse mass spectra for $\Sigma^*(1385)$, drawn as open circles and for $\overline{\Sigma^*}(1385)$ as closed circles for minimum bias p+p collisions at $\sqrt{s_{NN}}$ = 200 GeV. The dashed curves represent the exponential fits to the data.

The corrected spectra are also plotted with respect to $\rm p_T$, and fit with the function

$$\frac{\rm d^2N}{2\pi \rm p_T dy dp_T} = \rm Ae^{-\frac{m_T}{T}}, \tag{6.2}$$

to calculate the mean $\rm p_T$ ($\langle p_T \rangle$) with the fit parameters by evaluating:

$$\langle p_T \rangle = \frac{\int_0^\infty A\rm p_T e^{-\frac{m_T}{T}}}{\int_0^\infty Ae^{-\frac{m_T}{T}}}. \tag{6.3}$$

The $\langle p_T \rangle$ for $\Sigma^*(1385)$ is derived from the full range integration (0-10 GeV/c) of the corresponding exponential fit.

Inverse slope parameters of the exponential fit functions, the $\langle p_T \rangle$, and the yields from the exponential fits of the $\Sigma^*(1385)^{\pm}$ and their antiparticles are presented in Table 6.3 for minimum bias p+p collisions at $\sqrt{s} = 200$ GeV.

p+p	T [MeV]	$\langle p_T \rangle$ [GeV/c]	Yields (dN/dy)
$\Sigma^*(1385)^{\pm}$	$319 \pm 6 \pm 16$	$1.02 \pm 0.02 \pm 0.07$	$(10.7 \pm 0.4 \pm 1.4)10^{-3}$
$\overline{\Sigma^*}(1385)^{\pm}$	$316 \pm 9 \pm 16$	$1.01 \pm 0.01 \pm 0.06$	$(8.9 \pm 0.4 \pm 1.2)10^{-3}$

Table 6.3: Inverse slope T, $\langle p_T \rangle$ and yield obtained from the exponential fits of the p_T spectra in Figure 6.1 for minimum bias p+p collisions. The statistical and systematic uncertainties are included.

The raw and corrected p_T integrated ratios of $\frac{\overline{\Xi}^+}{\Xi^-}$ and $\frac{\overline{\Sigma^*}(1385)}{\Sigma^*(1385)}$ are presented in Table 6.4. The corrected ratio of Ξ^- from topological identification is consistent with the raw ratio of Ξ^- from HCT [44]. Since the integrated raw and corrected ratios of $\Sigma^*(1385)$ are in agreement, the absorption correction of antiparticles is negligible for these ratios.

Table 6.4: The raw and corrected ratios of $\frac{\overline{\Xi}^+}{\Xi^-}$ and $\frac{\overline{\Sigma^*}(1385)}{\Sigma^*(1385)}$ in minimum bias p+p collisions.

Particle	Raw Ratio	Corrected Ratio
$\frac{\overline{\Xi}^+}{\Xi^-}$	0.99 ± 0.06	1.17 ± 0.35
$\frac{\overline{\Sigma^*}(1385)}{\Sigma^*(1385)}$	0.84 ± 0.11	0.83 ± 0.17

6.2 Au+Au Results for $\Sigma^*(1385)$

The mass and width fit parameters of the Gaussian and Breit-Wigner distributions of Ξ^-, $\Sigma^*(1385)$ and their antiparticles are presented in Table 6.5 for the 0-5% most central Au+Au collisions. Both mass and width are in agreement with the known PDG values, within their statistical and systematic uncertainties and with our detector resolution [39].

Table 6.5: Mass and width fit parameters of Ξ^-, $\Sigma^*(1385)$ and their antiparticles from the 0-5% most central Au+Au collisions including statistical and systematic errors for p_T and rapidity y given.

Particle	m [MeV/c^2]	Γ [MeV/c^2]	p_T [GeV/c]	$\lvert\mathbf{y}\rvert$
Ξ^-	$1320 \pm 1 \pm 1$	$4 \pm 1 \pm 1$	$0.25 - 4.00$	≤ 0.75
$\bar{\Xi}^+$	$1320 \pm 1 \pm 1$	$5 \pm 1 \pm 1$	$0.25 - 4.00$	≤ 0.75
Σ^*	$1375 \pm 5 \pm 3$	$43 \pm 5 \pm 6$	$0.25 - 4.00$	≤ 0.75
$\bar{\Sigma}^*$	$1380 \pm 4 \pm 3$	$28 \pm 11 \pm 6$	$0.25 - 4.00$	≤ 0.75

To extract the signal in individual $\mathrm{p_T}$ plots, $\Sigma^*(1385)$ and $\overline{\Sigma^*}(1385)$ were added to gain statistics in the 0-5% most central Au+Au collisions. The individual $\mathrm{p_T}$ and rapidity plots of $\Sigma^*(1385) + \overline{\Sigma^*}(1385)$ are presented in Appendix B. Since the width of the Breit-Wigner peak is in agreement with the PDG value for the $\mathrm{p_T}$ summed signal presented in Table 6.5, the width is fixed to 38 MeV/c^2 for each $\mathrm{p_T}$ and y plot. Table 6.6 presents the mass parameter for the $\Sigma^*(1385)$+$\overline{\Sigma^*}(1385)$ Breit-Wigner fit for the individual $\mathrm{p_T}$ and y plots.

Table 6.6: The mass and the width of the Breit-Wigner fit of the $\Sigma^*(1385)$+$\overline{\Sigma^*}(1385)$ from the 0-5% most central Au+Au collisions at mid rapidity $|y| < 0.75$, including only statistical errors for the $\mathrm{p_T}$ range given.

p_T [GeV/c]	$\Sigma^*(1385)$+$\overline{\Sigma^*}(1385)$ [MeV/c^2]
0.5–1.25	1375 ± 7
1.25–1.75	1370 ± 7
1.75–2.25	1383 ± 4
2.25–2.75	1378 ± 5
2.75–3.50	1393 ± 8

Since the signals of $\Sigma^*(1385)$ and $\overline{\Sigma^*}(1385)$ cannot be constructed individually for each $\mathrm{p_T}$ range due to limited statistics, the momentum spectra cannot be corrected separately for particles and antiparticles. However the $\mathrm{p_T}$ integrated ratios of $\frac{\bar{\Xi}^+}{\Xi^-}$ and $\frac{\overline{\Sigma^*}(1385)}{\Sigma^*(1385)}$ can be calculated via the raw yields of the $\mathrm{p_T}$ integrated signals. These raw ratios are 0.87 ± 0.18 for $\Sigma^*(1385)$ and 0.87 ± 0.10 for Ξ^-. The corrected ratio of $\frac{\bar{\Xi}^+}{\Xi^-} = 0.85 \pm 0.05$ from topologically identified Ξ^- is consistent with this raw ratio [45]. The differences between the efficiencies of antiparticles to particles should be negligible and the $\Sigma^*(1385)$ ratio should be close to the corrected value when statistics are available.

The corrected and normalized to unit rapidity $\mathrm{m_T} - \mathrm{m_0}$ spectra are presented in Figure 6.2 for the $\Sigma^*(1385)$+$\overline{\Sigma^*}(1385)$ in the 0-5% most central Au+Au collisions at $\sqrt{s_{\mathrm{NN}}}$=200 GeV. The error bars correspond to both statistical and bin-by-bin varying systematic uncertainties. The dashed curve in Figure 6.2 is the exponential fit, given in Equation 6.1, to the data.

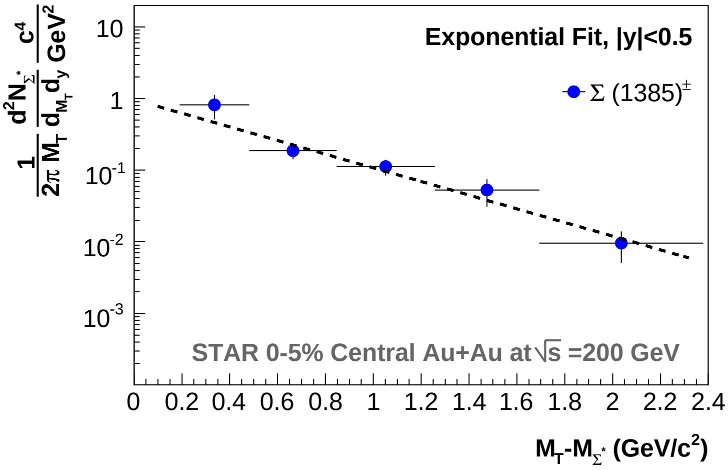

Figure 6.2: Corrected $\mathrm{m_T} - \mathrm{m_0}$ spectra normalized to unit rapidity for the $\Sigma^*(1385)$ added with $\overline{\Sigma^*}(1385)$ in the 0-5% most central Au+Au collisions at $\sqrt{s_{\mathrm{NN}}}$=200 GeV. Statistical and bin by bin varying systematic errors are included.

The inverse slope parameter of the exponential fit function, the $\langle p_T \rangle$, and the yield for $\Sigma^*(1385)^{\pm} + \overline{\Sigma^*}(1385)^{\pm}$ are presented in Table 6.7 for 0-5% most central Au+Au collisions at $\sqrt{s_{NN}}$ = 200 GeV. The yield can be normalized with a factor 1.87 to estimate the baryon yield of $\Sigma^*(1385)^{\pm}$, since the ratio of $\overline{\Sigma^*}(1385)/\Sigma^*(1385)$ is 0.87.

0-5% Most Central Au+Au	T [MeV]	$\langle \mathrm{p_T} \rangle$ [GeV/c]	Yields (dN/dy)
$\Sigma^*(1385) + \overline{\Sigma^*}(1385)$	$456 \pm 54 \pm 23$	$1.28 \pm 0.15 \pm 0.09$	$9.35 \pm 1.38 \pm 1.25$

Table 6.7: Temperature T, $\langle p_T \rangle$ and yield obtained from the exponential fit of the p_T spectrum in Figure 6.2 for the $0-5\%$ most central Au+Au collisions. The statistical and systematic uncertainties are included.

6.3 d+Au Results for $\Sigma^*(1385)$

The mass and width fit parameters of the Gaussian and Breit-Wigner distributions of the Ξ^-, $\Sigma^*(1385)$ and their antiparticles are presented in Table 6.8 for minimum bias d+Au collisions. Both mass and width are in agreement with the known PDG values, within statistical and systematic uncertainties and with our detector resolution [39].

Table 6.8: Mass and width fit parameters of Ξ^-, $\Sigma^*(1385)$ and their antiparticles from minimum bias d+Au collisions including statistical and systematic errors for p_{T} and rapidity y given.

Particle	m [MeV/c^2]	Γ [MeV/c^2]	p_{T} [GeV/c]	$\lvert\mathbf{y}\rvert$
Ξ^-	$1320 \pm 1 \pm 1$	$7 \pm 1 \pm 1$	$0.25 - 4.00$	≤ 0.75
$\bar{\Xi}^+$	$1320 \pm 1 \pm 1$	$7 \pm 1 \pm 1$	$0.25 - 4.00$	≤ 0.75
Σ^*	$1374 \pm 2 \pm 3$	$41 \pm 5 \pm 6$	$0.25 - 4.00$	≤ 0.75
$\bar{\Sigma}^*$	$1377 \pm 2 \pm 4$	$40 \pm 6 \pm 6$	$0.25 - 4.00$	≤ 0.75

For each individual $\mathrm{p_T}$ and rapidity range, the invariant mass spectra of $\Sigma^*(1385)$ and $\overline{\Sigma^*}(1385)$ are presented in Appendix B. The 5 free fit parameters of the fit functions with the fixed $\Sigma^*(1385)$ width are determined. Table 6.9 presents the mass parameter for the $\Sigma^*(1385)$ and its antiparticle from Breit-Wigner fits of the individual $\mathrm{p_T}$ and y plots.

Table 6.9: The mass of the Breit-Wigner fit of the $\Sigma^*(1385)$ and their antiparticles from minimum bias d+Au collisions at mid rapidity $|y| < 0.75$, including statistical and systematic errors for the p_{T} given.

p_{T} [GeV/c]	$\Sigma^*(1385)$ [MeV/c^2]	$\overline{\Sigma^*}(1385)$ [MeV/c^2]
0.25–1.00	$1371 \pm 3 \pm 7$	$1376 \pm 4 \pm 7$
1.00–1.25	$1374 \pm 3 \pm 3$	$1377 \pm 2 \pm 3$
1.25–1.50	$1376 \pm 3 \pm 3$	$1380 \pm 2 \pm 3$
1.50–1.75	$1383 \pm 2 \pm 3$	$1368 \pm 4 \pm 3$
1.75–2.00	$1376 \pm 4 \pm 3$	$1381 \pm 4 \pm 3$
2.00–2.25	$1372 \pm 4 \pm 3$	$1382 \pm 3 \pm 3$
2.25–2.50	$1387 \pm 4 \pm 3$	$1378 \pm 3 \pm 3$
2.50–2.75	$1381 \pm 5 \pm 4$	$1405 \pm 7 \pm 4$
2.75–3.50	$1371 \pm 8 \pm 2$	$1391 \pm 5 \pm 2$

Corrected $\mathrm{m_T} - \mathrm{m_0}$ spectra are presented in Figure 6.3 for the $\Sigma^*(1385)$ (closed circles) and $\overline{\Sigma^*}$(1385) (open circles) in minimum bias d+Au collisions at $\sqrt{s_{\mathrm{NN}}}$=200 GeV. The spectra are normalized to $|y| < 0.5$ to extract the yields for unit rapidity. The error bars presented correspond to both statistical and bin-by-bin systematic uncertainties. The dashed curves in Figure 6.3 are from the exponential fits (Equation 6.1) to the data.

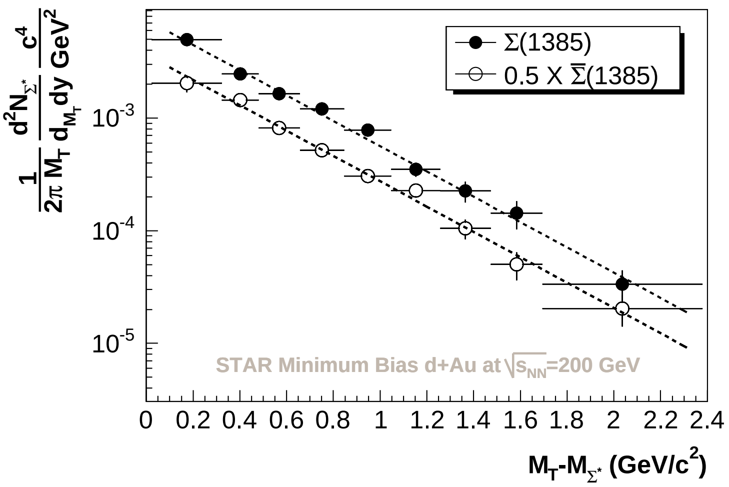

Figure 6.3: The transverse mass spectra for Σ^*(1385), presented as closed circles, and for 0.5× $\overline{\Sigma^*}$(1385), open circles, in minimum bias d+Au collisions at $\sqrt{s_{NN}}$ = 200 GeV. The dashed curves represent the exponential fits to the data.

Inverse slope parameters, the $\langle p_T \rangle$, and the yields for $\Sigma^*(1385)^{\pm}$ and $\overline{\Sigma^*}(1385)^{\pm}$ are presented in Table 6.10 for minimum bias d+Au collisions at $\sqrt{s_{NN}}$ = 200 GeV.

d+Au	T [MeV]	$\langle p_T \rangle$ [GeV/c]	Yields (dN/dy)
Σ^*(1385)	$387 \pm 15 \pm 27$	$1.14 \pm 0.05 \pm 0.08$	$(3.23 \pm 0.15 \pm 0.42) \times 10^{-2}$
$\overline{\Sigma^*}$(1385)	$386 \pm 16 \pm 28$	$1.12 \pm 0.05 \pm 0.08$	$(3.15 \pm 0.15 \pm 0.41) \times 10^{-2}$

Table 6.10: Temperature T, $\langle p_T \rangle$ and yield obtained from the exponential fits of the $m_T - m_0$ spectra in Figure 6.3 for minimum bias d+Au collisions. Both statistical and systematic uncertainties are included in the given values.

The raw and corrected ratios of $\frac{\overline{\Xi}^+}{\Xi^-}$ and $\frac{\overline{\Sigma^*}(1385)}{\Sigma^*(1385)}$ are presented in Table 6.11. The preliminary corrected ratio of Ξ^- from topological identification is in agreement with the raw ratio from HCT [46]. The raw and corrected ratios of $\overline{\Sigma^*}(1385)/\Sigma^*(1385)$are also in agreement within the statistical and systematic uncertainties in d+Au collisions at $\sqrt{s_{\rm NN}} = 200$ GeV.

Table 6.11: The raw and corrected ratios of $\frac{\overline{\Xi}^+}{\Xi^-}$ and $\frac{\overline{\Sigma^*}(1385)}{\Sigma^*(1385)}$ in minimum bias d+Au collisions.

Particle	Raw Ratio	Corrected Ratio
$\frac{\overline{\Xi}^+}{\Xi^-}$	0.86 ± 0.1	0.85 ± 0.09
$\frac{\overline{\Sigma^*}(1385)}{\Sigma^*(1385)}$	0.97 ± 0.12	0.98 ± 0.19

6.4 Nuclear Effects

Nuclear effects on the particle spectra from d+Au collisions are measured by comparison to the p+p spectra via the nuclear modification factor:

$$R_{dAu} = \frac{d^2N^{dAu}/dp_Td\eta}{T_{AA}d^2\sigma^{NN}/dp_Td\eta},$$

where $T_{AA} = \langle N_{bin}\rangle/\sigma^{NN}_{inel}$. N_{bin} is calculated from a Glauber model calculation which accounts for the nuclear collision geometry while σ^{NN} is experimentally determined for the p+p elastic and inelastic collisions.

The nuclear modification factor of the $\Sigma^*(1385)$ in d+Au collisions at $\sqrt{s_{\rm NN}} = 200$ GeV is shown in Figure 6.4-a. There is a $\rm p_T$ dependent increase in the R_{dAu} measurement and a small enhancement over binary scaling for the higher momenta. The enhancement over the binary scaling can be explained by the 'Cronin Effect', a generic term for the experimentally observed broadening of the transverse momentum distributions at intermediate $\rm p_T$ in p+A collisions as compared to p+p collisions [47, 48]. The Cronin Effect can be described by initial multiple parton scattering models. It is expected that the transverse momentum of the parton inside the incoming proton, while traversing the Au nucleus, is broadened due to the multiple scattering of the nucleons of the Au nucleus.

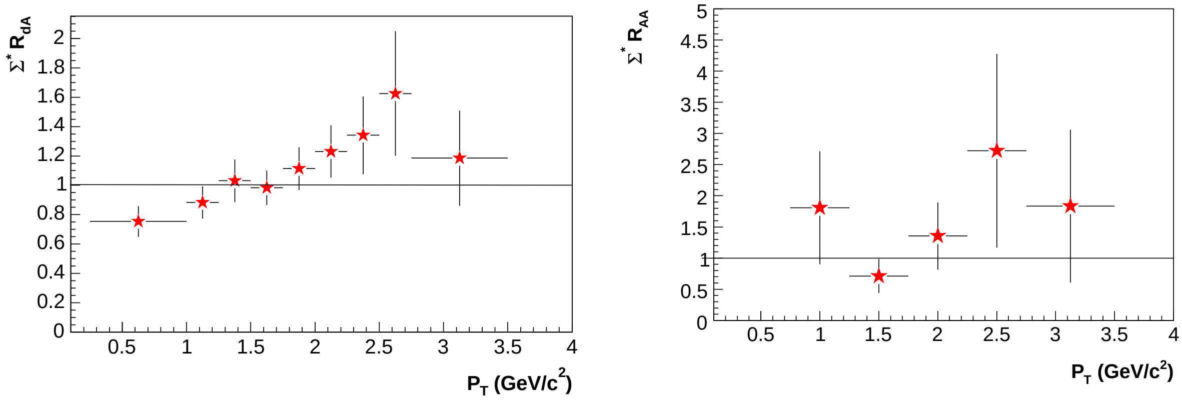

(a) **(b)**

Figure 6.4: The nuclear modification factors **(a)** R_{dAu} and **(b)** R_{AA} for the $\Sigma^*(1385)+\overline{\Sigma}^*(1385)$. For R_{dAu}, the p_T spectrum in minimum bias d+Au collisions is divided by the scaled spectrum in minimum bias p+p collisions at $\sqrt{s_{NN}} = 200$ GeV. For R_{AA}, the p_T spectrum in the 0-5% most central Au+Au collisions is divided by the scaled spectrum in minimum bias p+p collisions at $\sqrt{s_{NN}} = 200$ GeV.

The R_{AA} measurement of the $\Sigma^*(1385)$ is presented in Figure 6.4-b. Due to the limited statistics of the Au+Au collisions from FY02, the R_{AA} measurement of $\Sigma^*(1385)$ is not conclusive. The R_{AA} measurement of $\Sigma^*(1385)$ with more bins and smaller error bars is expected to be performed with the data from FY04 Au+Au collisions with a factor of 10 higher statistics.

Chapter 7

Pentaquark Search

The possible existence of pentaquarks, particles with four quarks and one anti-quark, is an exciting subject in nuclear and particle physics. Experimental evidence for one of the pentaquark states with a narrow width, Θ^+ has been presented by more than ten experiments. However the null observation of the same pentaquark has been shown by a similar number of experiments. The large amount of data recorded by the STAR experiment in elementary p+p and d+Au collisions make it feasible to search for existence of the pentaquark. In this chapter the exotic strange baryon search in STAR at $\sqrt{s_{\rm NN}} = 200$ GeV is presented.

7.1 Pentaquark States

The presence of pentaquarks was predicted by R. L. Jaffe with multiquark bag models [49, 50] and later by D. Diakonov et al. using chiral soliton models of baryons [51]. The pentaquarks in these models form an anti-decuplet which is presented in Figure 7.1.

The observation of what was called a Θ^+ consisting of uudd$\bar{s}$ quarks was announced by SPring-8 researchers in the spring of 2003, and in the same year, the CLAS Experiment at Jefferson Laboratory, the State Scientific Center Institute for Theoretical and Experimental Physics in Moscow (ITEP) and the ELectron Stretcher Accelerator (ELSA) in Bonn reported evidence of the Θ^+ pentaquark in photon-nucleus and kaon-nucleus reactions [52, 53, 54, 55]. Missing mass spectra for the

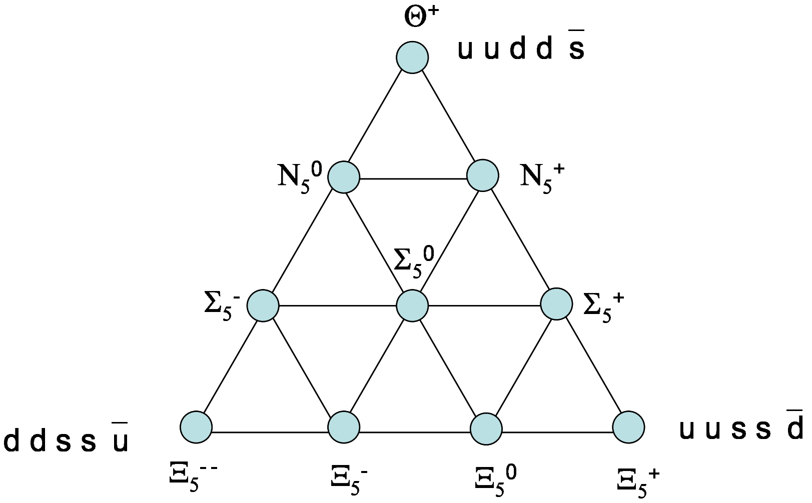

Figure 7.1: Anti-decuplet of pentaquarks as predicted by chiral soliton models.

$\gamma + d \rightarrow K^+ + K^- + X$ reaction measured with the LEPS detector at SPring-8 are shown in Figure 7.2 for the Θ^+ pentaquark and $\Lambda(1520)$ baryonic resonance. Since many of the positive sightings come from data taken with relatively low statistics, the CEBAF Large Acceptance Spectrometer (CLAS) collaboration in Hall B recently repeated some of these experiments with higher statistics. In these higher statistics measurements the previously observed pentaquark signal could not be reproduced, contradicting the earlier (low-statistics) results from CLAS. This suggests that the initial Θ^+ pentaquark observation with CLAS was a statistical fluctuation [56]. Evidence for Ξ_5^{--} and Ξ_5^0 pentaquarks (the bottom members of the anti-decuplet) was shown by NA49 experiment in p+p collisions [57]. Other experiments have searched for the Ξ_5^{--} pentaquark (e.g., the BABAR experiment in $e^+ + e^-$ collisions), but no significant signal was observed [58]. The observation of the Ξ_5 pentaquark will remain controversial until definitive experimental evidence is uncovered. The existence of pentaquarks remains an open question. It is possible that pentaquarks exist but with a very broad width or a smaller-than-expected cross-section.

The high energies and particle densities resulting from collisions at the Relativistic Heavy Ion Collider (RHIC) are expected to create an ideal environment for pentaquark production [59, 60, 61, 62]. There are millions of p+p, d+Au and Au+Au events recorded. The higher number of participants in d+Au collisions results in a higher mean number of charged tracks per collision in comparison to p+p events. Likewise, in Au+Au collisions the mean number of charged tracks are much higher than in d+Au collisions. However, the higher combinatorial backgrounds in Au+Au events, cause low efficiency and acceptance for particle identification. In the pentaquark analysis, only d+Au collisions are used in our search for pentaquarks due to relatively larger statistics.

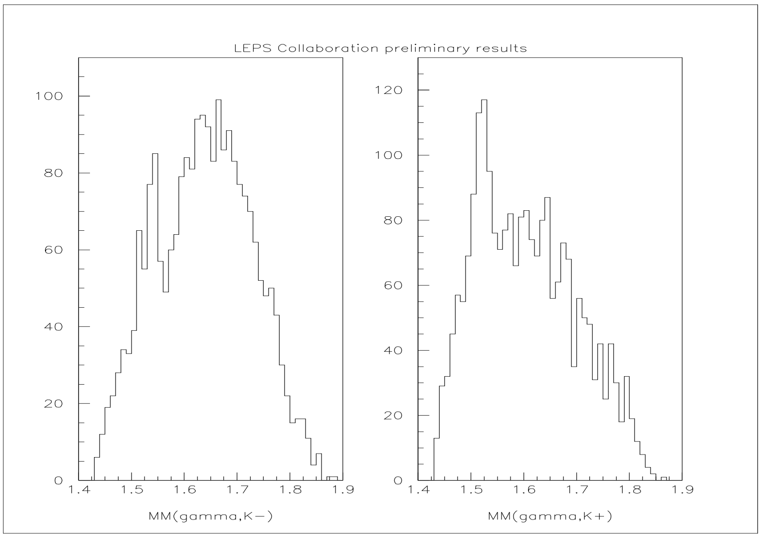

Figure 7.2: Preliminary missing mass spectra for the $\gamma + d \rightarrow K^+ + K^- + X$ reaction measured with the LEPS detector at SPring-8. The Θ^+ peak is seen at about 1.53 GeV on the left and the $\Lambda(1520)$ peak is seen at 1.52 GeV on the right. Plot is taken from [63].

7.2 Feasibility Study

The Θ^+ pentaquark is observed to decay into two channels, n+K and $\mathrm{p} + \mathrm{K}^0_\mathrm{s}$. Since there is no identification of neutrons in the TPC, the $K^0_S + p$ decay channel is used for this search. To study the decay mechanism and to optimize the applied cuts, Monte Carlo simulations are used. For this study, first one Monte Carlo Θ^+ pentaquark is chosen from a thermal exponential distribution with T = 300 MeV in the rapidity interval $|y| < 1.5$. Then it is embedded into a real p+p event with a full TPC simulation. The chosen input width, 10 MeV/c^2, and the input mass, 1.54 GeV/c^2, are consistent with the reported masses and widths of Θ^+ [52, 53, 54]. In Figure 7.3-a, the invariant mass spectrum of the input MC simulated Θ^+ and in Figure 7.3-b the invariant mass spectrum of the reconstructed Θ^+ and the estimated mixed event background are presented.

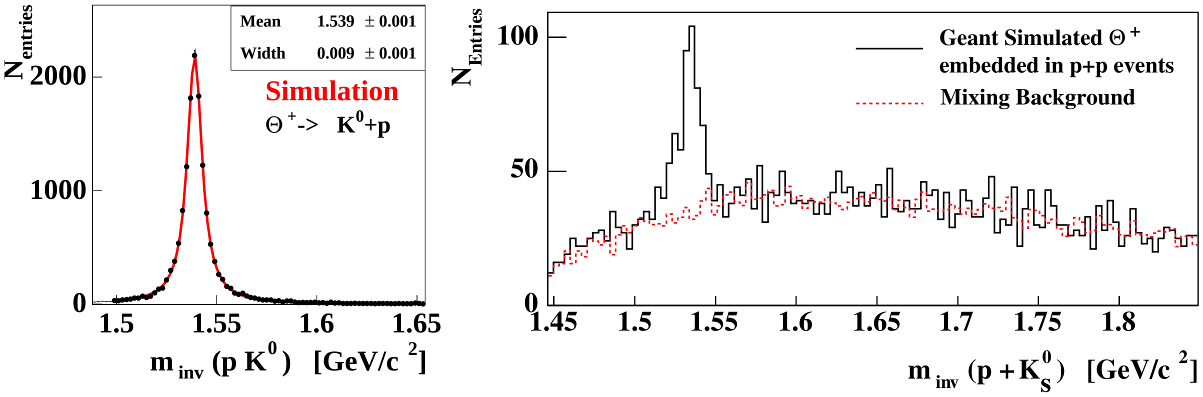

(a) (b)

Figure 7.3: (**a**) Invariant mass spectrum of the Monte Carlo generated input for the Θ^+. (**b**) Invariant mass spectrum of the Monte Carlo simulated Θ^+ embedded in real p+p events with the mixing technique. The black solid histogram is the signal and the red dashed histogram is the mixed event background. The simulated signal can be clearly seen.

We find that $\sim 3\%$ of these Monte Carlo generated Θ^+'s are successfully reconstructed. The reconstructed width and the mass is consistent with the Monte Carlo input. The p_T vs rapidity of the input Θ^+ and those that are then reconstructed in the TPC are shown in Figure 7.4. The TPC acceptance and the efficiency of the particle reconstruction can be calculated from these two histograms as their ratio. As can be seen from Figure 7.4-b, the TPC acceptance is limited to $|y| < 1$. Low efficiencies are found for low p_T particles ($p_T < 0.5$ GeV/c) due to tracking inefficiency and high p_T particles ($p_T > 2$ GeV/c) due to cuts applied to purify the particle identification to minimize the backgrounds.

Using this technique, the decay properties with the simulated tracks such as the

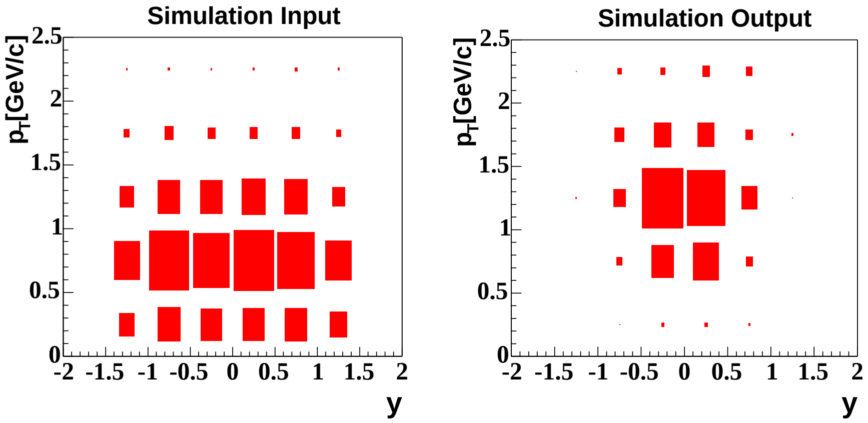

(a) (b)

Figure 7.4: (**a**) The $\mathrm{p_T}$ vs rapidity of the Θ^+ input and (**b**) the reconstructed particle. The TPC acceptance and the particle efficiency for the corresponding simulated particles can be calculated by division of the values in b by a.

momentum distribution of the decay daughters can be studied. In Figure 7.5, the momentum distributions of the K_S^0 on the left and proton on the right are presented. With this study, we can optimize momentum cuts to increase the signal-to-background ratio. Clearly, an optimized cut to improve this ratio is to only accept protons with momentum less than 1 GeV/c. The picture is less clear for K_S^0 mesons, however a momentum cut to reject particles with momentum higher than 1.4 GeV/c can be applied to minimize the contamination of K_S^0 mesons not decaying from Θ^+.

7.3 Θ^+ Pentaquark Search

A topological measurement of pentaquarks is not possible since their lifetimes are short due to their strong decay. Instead, Θ^+ pentaquarks are investigated using the combinatorial invariant mass technique. This is similar to the one that is used for the $\Sigma^*(1385)$ resonance analysis. Three different techniques are used to minimize the backgrounds; HCT, strangeness tagging and a search using kinks.

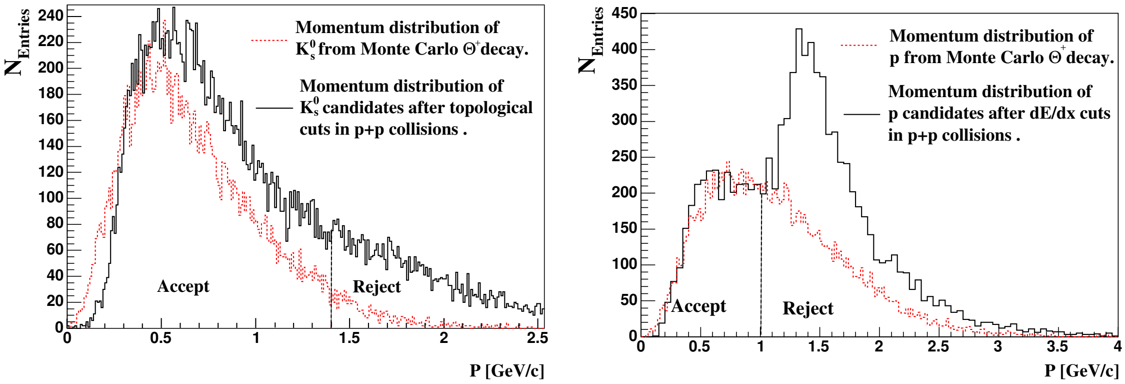

(a) **(b)**

Figure 7.5: **(a)** The K^0_S momentum distribution and **(b)** the proton momentum distribution. Black solid histograms represent accepted K^0_S on the left and accepted p on the right (after the dE/dx cut). Red dashed histograms are of the decay daughters of the Monte Carlo generated Θ^+ for the same number of events.

7.3.1 Searching for the Θ^+ Pentaquark with the HCT

The HCT technique described previously for the $\Sigma^*(1385)$ analysis can be applied directly to the search for pentaquarks. First, event selection is performed; this is similar to the $\Sigma^*(1385)$ analysis case. The only difference is the wider primary vertex position of the accepted events ($|Z| < 100$ cm) in order to maximize the number of events used in this search.

After event selection, the K^0_S mesons are identified via the topological technique in each event as discussed previously in Section 4.3.2. Figure 7.6 shows the invariant mass spectrum of $\pi^+ + \pi^-$ in minimum bias d+Au collisions at $\sqrt{s_{\mathrm{NN}}} = 200$ GeV. The applied cuts on V_0 particles to reconstruct this invariant mass spectrum for K^0_S are presented in Table 7.1. These cuts are selected to maximize the signal-to-background ratio and minimize the backgrounds. The protons are identified with the dE/dx and magnetic field information in the TPC and the applied cuts are presented in Table 7.2.

Figure 7.7-a shows the invariant mass (red curve) and mixed event (black curve) spectra of the K^0_S and p. The rapidity and the transverse momentum of the constructed Θ^+ is required to be $|y| < 1$ and $0.50 < \mathrm{p_T} < 1.25$ GeV/c, respectively. The arrow represents the expected mass of a potential Θ^+ state. There is a population

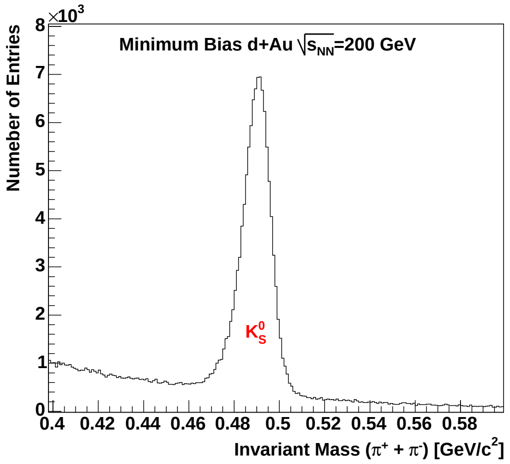

Figure 7.6: Invariant mass spectrum for $K^0_S \rightarrow \pi^- + \pi^+$ with decay topology information in d+Au collisions at $\sqrt{s_{NN}} = 200$ GeV.

Cut Description	Value
DCA Global	< 1.5 [cm]
DCA of positive daughter to primary vertex	> 1 [cm]
DCA of negative daughter to primary vertex	> 1 [cm]
DCA between V_0 and primary vertex	< 0.8 [cm]
DCA between daughters	< 0.9 [cm]
Decay length of V_0	$2.5 < L < 10$ [cm]
Number of hits for positive daughters	> 15
Number of hits for negative daughters	> 15
dE/dx	$3\ \sigma$
Momentum of both π	$0.2 - 0.6$ [GeV/c]

Table 7.1: Applied cuts for K^0_S identification in minimum bias d+Au collisions. V_0 particles are identified as K^0_S if they pass all cuts and the corresponding invariant mass is in the range 0.484-0.51 GeV/c^2.

above the background in the expected mass range, however the significance[1] of the signal ($3.4 \pm 0.9\sigma$) is not sufficiently large to postulate the existence of a Θ^+ signal.

---

[1] The significance of a signal is given as $\widetilde{S} = \frac{S}{\sqrt{S+(1+n)B}}$ where S is the counts in the signal and B the counts in the background. The n represents the normalization factor for the mixed event background.

Cut Description	Value
DCA Global	< 1.5 cm
Momentum [GeV/c]	$0.3 - 1.5$
Transverse Momentum [GeV/c]	$0.3 - 1.5$
Number of Fit Points	> 15
Number of Fit Points / Number of possible hits	> 0.55
dE/dx	$3\ \sigma$

Table 7.2: Cuts applied for p identification in d+Au collisions.

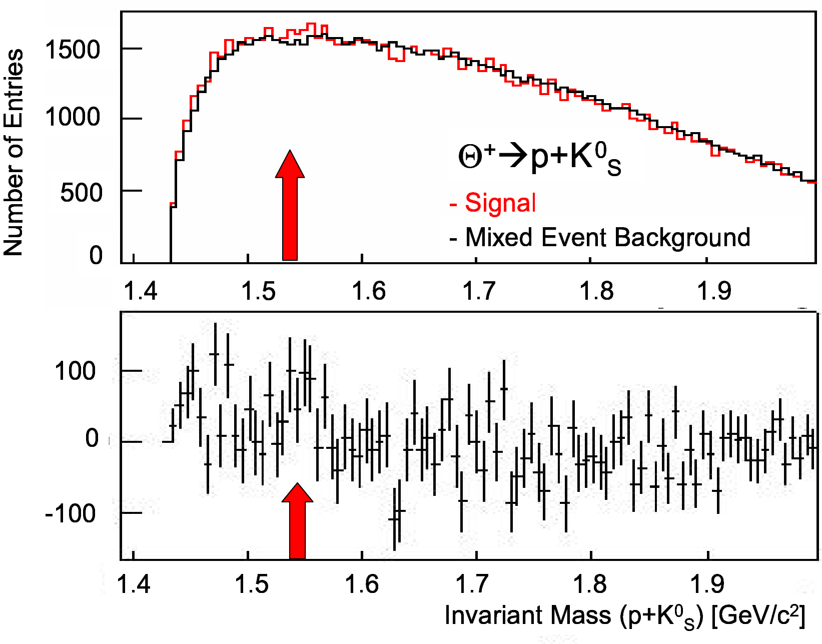

Figure 7.7: **(a)** Invariant mass spectrum before background subtraction (in red) and the mixed event background (in black) **(b)** Invariant mass spectrum after background subtraction for $\mathrm{K^0_S} + \mathrm{p}$ in minimum bias d+Au collisions at $\sqrt{s_{NN}} = 200$ GeV. The rapidity and transverse momentum range of the constructed Θ^+ is $|y| < 1$ and $0.50 < \mathrm{p_T} < 1.25$ GeV/c, respectively. The arrow represents where the postulated Θ^+ state is expected.

7.3.2 Searching for the Θ^+ Pentaquark in Strangeness Conserving Particle Tagging

The initial data presented by the CLAS collaboration on the reaction $\gamma + p \rightarrow \pi^+ + K^- + K^+ + n$ shows a peak at a mass of 2.4 GeV/c^2 when the invariant mass of

$n + K^+ + K^-$ is plotted from the possible Θ^+ candidate events [64]. The Figure 7.8-a shows their invariant mass spectrum for the Θ^+ pentaquark. The corresponding significance of this Θ^+ peak is calculated by the CLAS collaboration as $7.8 \pm 1\sigma$ when significance is defined as $\widetilde{S} = S/\sqrt{B}$. However the value is smaller and is estimated to be $4.5 \pm 0.9\sigma$ when the statistical fluctuations of the apparent signal are taken into account in the significance definition in order to get a conservative estimate of possible errors due to background mis-estimation.

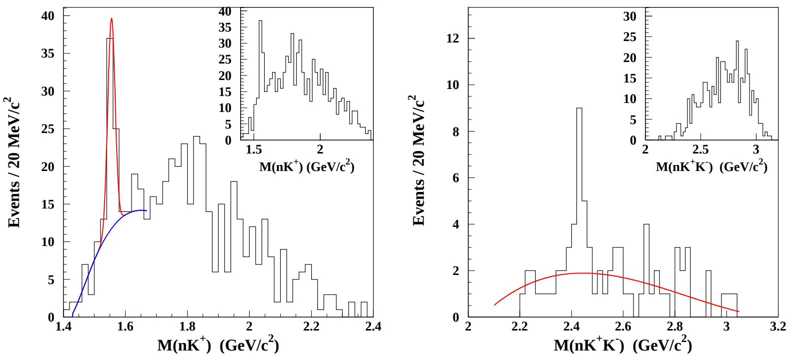

(a) **(b)**

Figure 7.8: **(a)** Invariant mass spectrum for $\Theta^+ \to K^+ + n$ and **(b)** $N^* \to \Theta^+ + K^-$ from the CLAS experiment in the $p + \gamma \to \Theta^+ + K^-$ production channel. Figures are taken from [64].

The significance of the signal observed in Figure 7.8-b from the CLAS experiment is estimated to be $3.0 \pm 0.8\sigma$ with the consideration of statistical fluctuations of the signal. This apparent excess was suggestive of an intermediate baryon state called the N^* resonance. Further evidence for this resonance is suggested in preliminary results from the NA49 experiment in p+p collisions [65].

With the motivation of what has been observed in the CLAS experiment, a strangeness conserving particle, K^- meson, is chosen to initially tag events for further investigation. The d+Au events are selected with a primary vertex requirement $|Z| < \pm 100$ cm along the beam direction. The K^0_S mesons and p baryons are identified with cuts identical to those applied in Table 7.1 and Table 7.2, respectively. Similar to proton identification, negatively charged K mesons are identified using the dE/dx and magnetic field information in the TPC. (See Table 7.3 for the cuts applied on primary tracks.)

Cut Description	Value
DCA Global	< 1.5 cm
Momentum [GeV/c]	$0.1 - 1.2$
Number of Fit Points	> 15
dE/dx	$3\ \sigma$

Table 7.3: Cuts applied for K^- identification in d+Au collisions.

The invariant mass distribution of $K^0_S + p + K^-$ in d+Au collisions is presented in Figure 7.9. A detailed view of a narrow invariant mass range is presented in Figure 7.9-b. There is no visible population above background within the expected hypothetical N^* mass range (2.3−2.5 GeV/c^2). In order to minimize the backgrounds associated with the high charged particle multiplicities in d+Au events, we select a subset of pentaquark decay candidates (K^0_S and p) that form the 2.3 − 2.5 GeV/c^2 mass range of the $K^0_S + p + K^-$ invariant mass distribution (when combined with the K^- meson) and tag these events for the Θ^+ analysis.

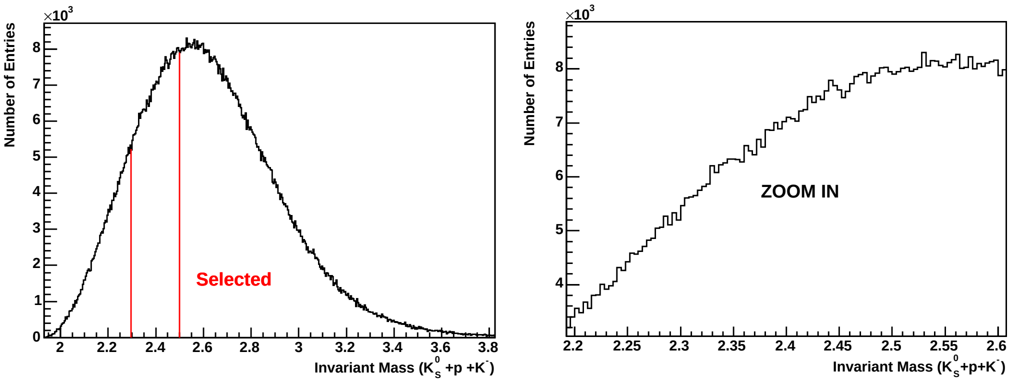

(a) **(b)**

Figure 7.9: **(a)** The invariant mass distribution of $K^0_S + p + K^+$ in d+Au collisions at $\sqrt{s_{\mathrm{NN}}} = 200$ GeV. The red lines represent the selected events in the range 2.3 − 2.5 GeV/c^2. **(b)** A narrow range detailed view of (a). No obvious population above the background is observed in this mass range.

The invariant mass distribution of $K^0_S + p$ from the candidates which pass the strangeness tagging qualifying cut defined above is presented in Figure 7.10. The black curve represents the five-variable polynomial fit to the background. The arrows represent the location of the expected signal. There is no population above the background observed in the mass range reported by the CLAS experiment for a Θ^+ pentaquark.

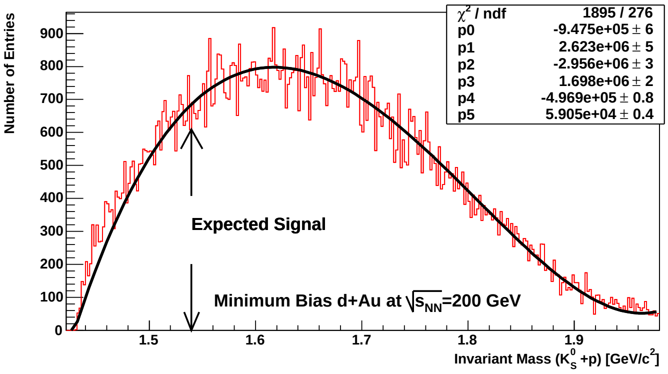

Figure 7.10: The invariant mass distribution of $K^0_S + p$ from selected events which pass the qualifying cuts for strangeness tagging in d+Au collisions at $\sqrt{s_{\rm NN}} = 200$ GeV. The black curve represents a five variable polynomial fit to the background. The arrows represent the location of the expected signal.

7.3.3 Searching for the Θ^+ Pentaquark by Using Kinks in the TPC

The third technique that is used for the search for a Θ^+ pentaquark involves using Kinks that are topologically reconstructed in the TPC. Knee shape tracks, which are called Kinks, form when a charged particle decays into another charged particle (with a momentum change) and a neutral particle (not visible) within the TPC. The main reason to reconstruct Kinks is to identify charged K mesons from their leptonic decay channel ($K^+ \rightarrow \mu^+ + \nu_\mu$). If any of the K mesons produced during heavy ion collisions interact with neutrons in the TPC gas, they may produce a Θ^+ pentaquark through the production channel $K^+ + n \rightarrow \Theta^+ \ \rightarrow K^0_S + p$. A schematic representation of the production of the Θ^+ from a K^+ interaction with a neutron in the TPC is shown in Figure 7.11.

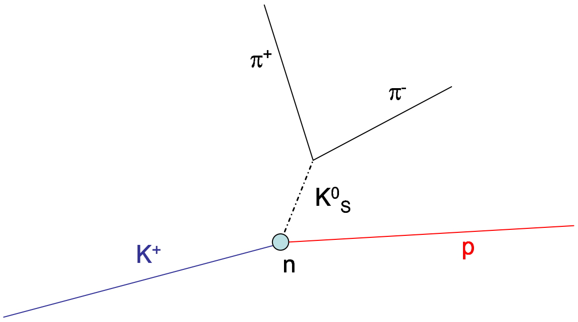

Figure 7.11: A schematic representation of production of Θ^+ from a K^+ interaction with a neutron in the TPC.

Cut Description	Value
DCA Global Mother [cm]	< 1.5
Mother K^+ dE/dx	$5\ \sigma$
Daughter p dE/dx	$5\ \sigma$
Momentum of K^+ [GeV/c]	$0.15 - 1.5$

(a)

Cut Description	Value
DCA Global K^0_S [cm]	< 1.5
DCA of decay tracks [cm]	< 0.9
Decay length of V_0 [cm]	> 2.5
N(hits) for positive	> 10
N(hits) for negative	> 10
dE/dx	$3\ \sigma$

(b)

Table 7.4: **(a)** The applied cuts for identification of mother K^+ and daughter p of Kinks in minimum bias d+Au collisions. **(b)** The applied cuts for K^0_S identification in minimum bias d+Au collisions. V_0 particles are identified as K^0_S if they pass all the cuts described and the corresponding invariant mass is in the range 0.484-0.51 GeV/c^2.

Event selection is performed with the primary vertex requirement $|Z| < 100$ cm for the d+Au events. Selected events are filtered by requiring both V_0 particle and Kink identification. Further cuts as presented in Table 7.4 are applied on Kink mothers and daughters and V_0 particles to identify the K^+, p and K^0_S particles. The applied cuts on V_0 particles are less tight in comparison to the previous studies in order to use all available Kink candidates (See Table 7.1). The invariant mass spectrum of the K^0_S particle is presented in Figure 7.12. Due to less restrictive cuts the signal to background for the K^0_S particle is low (significance $16 \pm 1\sigma$).

The red curve in Figure 7.13-a represents the invariant mass distribution of $K^0_S + p$ from topologically identified K^0_S mesons and the proton candidates of Kink decays.

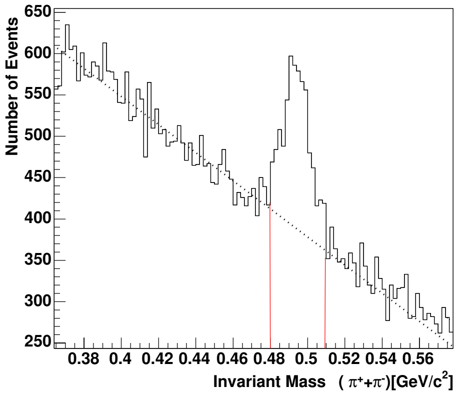

Figure 7.12: Invariant mass spectrum for $K_S^0 \rightarrow \pi^- + \pi^+$ with decay topology information in d+Au collisions at $\sqrt{s_{NN}} = 200$ GeV. The red lines represent the mass range accepted for the K_S^0 candidates (0.484-0.51 GeV/c^2). The dashed line is a linear fit to the background. The cuts applied on V_0 particles to identify K_S^0 candidates are presented in Table 7.4.

The black curve in the invariant mass plot is the five-variable polynomial fit to the mixed event background presented as the black bins. The mixed event background subtracted signal is shown in Figure 7.13-b. The arrows represent the expected location of the Θ^+ signal. A population over the background is present with a significance of 3.5 ± 1.0 in a smaller shifted mass region (~ 1.51 GeV/c^2). However this significance is too low to claim any detection. Spurious signals from noise fluctuations are more likely to occur near the expected mass than at it.

7.4 The Θ^{++} Pentaquark Search

The isospin measurement of the Θ^+ pentaquark can be used to eliminate different models [66]. This measurement can be performed by searching for possible isotensor partners of the Θ^+ pentaquark. For example, if Θ^+ has isospin I = 1, then there should be two other members of the isotriplet, a neutral and a doubly charged state. It is predicted that the doubly charged state, a Θ^{++} pentaquark, would decay into $p+K^+$ [67]. We examined the invariant mass of p+K$^+$ to search for Θ^{++} pentaquarks using the same events of the Θ^+ case.

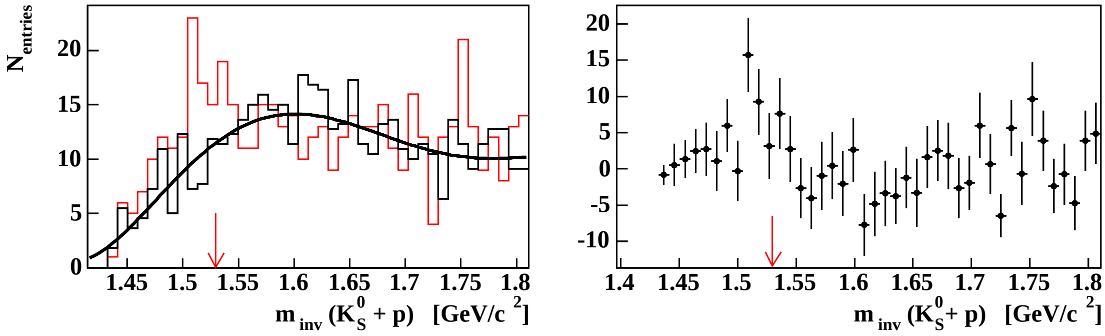

(a) (b)

Figure 7.13: **(a)** The red curve represents the invariant mass distribution of $K_S^0 + p$ from topologically identified K_S^0 mesons and proton candidates from Kink-formed decays in d+Au collisions at $\sqrt{s_{\mathrm{NN}}}$ = 200 GeV. The black curve is the five-variable polynomial fit to the mixed event background presented as the black bins. **(b)** The invariant mass distribution of $K_S^0 + p$ after the mixed event background subtraction. The arrows represent the location of the expected signal.

The d+Au events are selected again by applying two cuts, the reference multiplicity and Z position of the primary vertex. The events are required to be in the range 0-50 for reference multiplicity and $|Z| < 100$ cm to maximize the statistics. Both the dE/dx and the magnetic field information are used to select the decay particles, since the Θ^{++} decays into two charged particles, p and K^+. The protons and K meson tracks are selected to minimize the contamination from π mesons. Table 7.5 presents the cuts applied for the p and K particle identification in d+Au at $\sqrt{s_{\mathrm{NN}}}$ = 200 GeV.

Cut Description	K^+	p
$\lvert\overrightarrow{P}\rvert$ Momentum [GeV/c^2]	0.2 – 0.6	0.3 – 1.5
$\lvert \mathrm{P_T} \rvert$ Momentum [GeV/c^2]	0.2 – 0.6	0.3 – 1.5
Number of Fit Points	> 15	> 15
Number of Fit / Possible Hit Points	> 0.55	> 0.55
dE/dx	2.5 σ	2.5 σ
Input Mass [MeV/c^2]	493	938

Table 7.5: Applied cuts for p and K identification in minimum bias d+Au collisions.

The selected p and K particles with the dE/dx and momentum information are

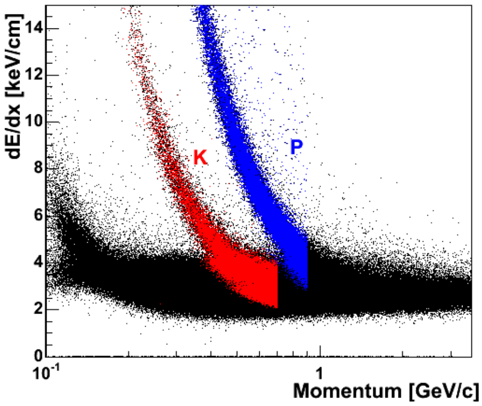

Figure 7.14: The dE/dx distribution of charged particles in the STAR TPC and selected p in blue and K in red bands as a function of momentum from minimum bias d+Au collisions.

presented in Figure 7.14 as blue and red bands, respectively. The p and K are selected using a 2.5 sigma Gaussian distribution around the Bethe-Bloch parametrization to minimize any contamination from adjacent bands.

The invariant mass spectra of the Θ^{++} (red curve) via the combinatorial technique and the mixed event background (black curve) are shown in Figure 7.15-a for minimum bias d+Au collisions at $\sqrt{s_{NN}}$ = 200 GeV. The mixed event background subtracted invariant mass spectrum is presented in Figure 7.15-b. The rapidity and the transverse momentum of the constructed Θ^{++} are $|y| < 1$ and $0.50 < \mathrm{p_T} < 1.25$ GeV/c, respectively. The line represents a linear fit of the correlated background which cannot be described with event mixing. The Gaussian curve represents the population over the background in the mass region where a possible Θ^{++} state is expected.

There is a possibility of measuring anti-pentaquarks at RHIC since the anti-baryon to baryon ratio is approximately one [68]. Given this observation, the Θ^{++} and $\overline{\Theta}^{--}$ candidates can be added to enhance the statistics of this investigation. Figure 7.16 shows the invariant mass spectra of $\mathrm{K^+ + p}$ added to $\mathrm{K^- + \bar{p}}$ for the specified rapidity and $\mathrm{p_T}$ bins. Negatively charged K mesons and $\bar{p}$ are identified with the same cuts as presented in Table 7.5 with the exception of their charge.

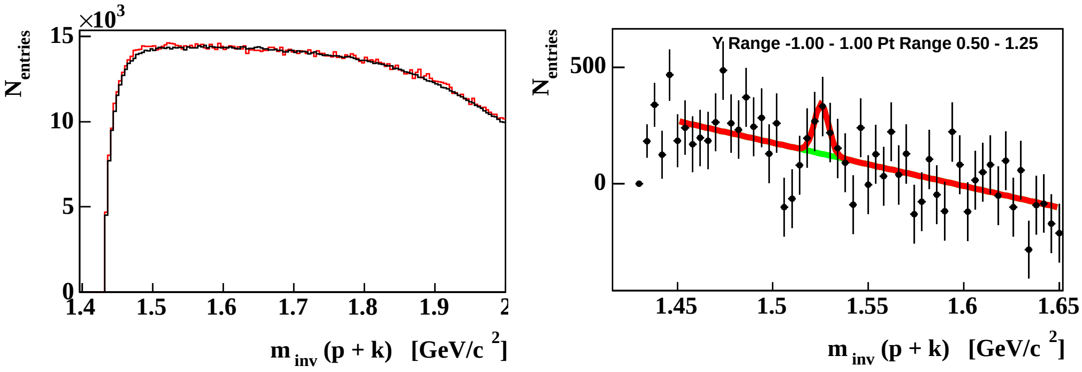

(a) (b)

Figure 7.15: **(a)**Invariant mass spectrum before the background subtraction (in red) and the mixed event background (in black); **(b)** invariant mass spectrum after background subtraction for $\mathrm{K}^+ + \mathrm{p}$ in minimum bias d+Au collisions at $\sqrt{s_{NN}} = 200$ GeV. See text for details.

There is a population above the background in the mass range predicted for the Θ^{++} pentaquark within the $\mathrm{p_T}$ range 0.5-1 GeV/c at mid rapidity. The best significance observed for this signal is 3.8 ± 1.0 for the $|\mathrm{y}| < 1$ and $0.5 < \mathrm{p_T} < 1$ GeV/c range. No signal is observed for the higher range $1 < \mathrm{p_T} < 1.25$ GeV/c.

7.5 Comparison of Θ^{++} and $\Lambda(1520)$ Production

The only difference between the decays products of the well known $\Lambda(1520)$ resonance and that of the Θ^{++} pentaquark is the charge of the K meson decay product. Since the $\Lambda(1520)$ is neutral, it decays into a proton and K^- meson, while the Θ^{++} is predicted to decay into a proton and K^+ meson. A study of the $\Lambda(1520)$ with cuts identical to those applied for the Θ^{++} decay candidates, with the exception of the charge of the K meson, is used to compare the hypothesized Θ^{++} pentaquark signal with the $\Lambda(1520)$ (See Table 7.5).

The invariant mass distributions of the $\Lambda(1520)$ and the mixed event background are presented in Figure 7.17-a. The mixed event background subtracted $\Lambda(1520)$ peak and the correlated leftover background is fit with a Breit-Wigner plus a linear distribution (see Figure 7.17-b).

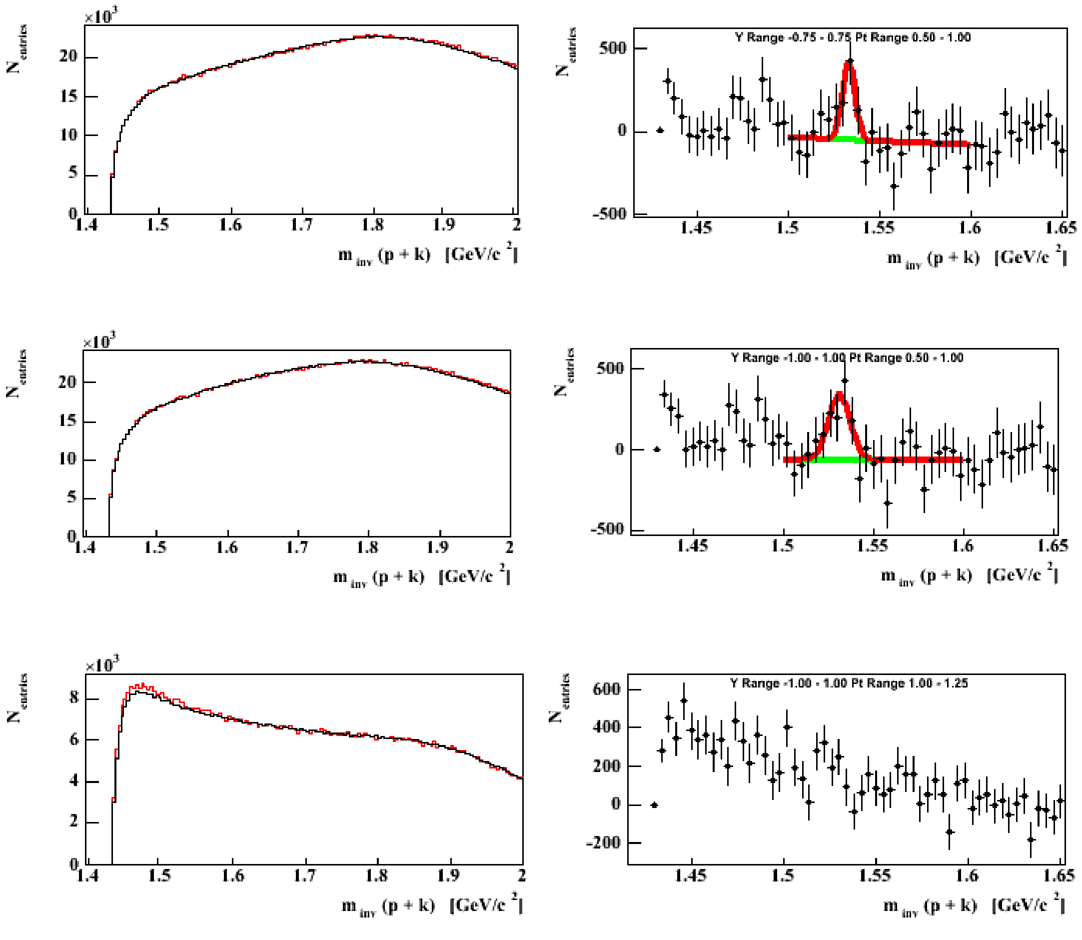

(a) **(b)**

Figure 7.16: Invariant mass spectra for the $(K^+ + p) + (K^- + \bar{p})$ **(a)** before the background subtraction (in red) and the mixed event background (in black); **(b)** after background subtraction in minimum bias d+Au collisions at $\sqrt{s_{NN}} = 200$ GeV for the specified rapidity and p_T bins. A Gaussian curve for the signal is fit to the population over the background in the mass region where a possible Θ^{++} state is expected.

The number of raw $\Lambda(1520)$ resonance counts for the $|y| < 0.75$ and $0.5 < p_T < 1.25$ GeV/c from bin counting is $(0.42 \pm 0.02) \times 10^{-3}$ per event. Since the proton and K meson branching ratio of $\Lambda(1520)$ is only 22.5%, the overall raw yield of the resonance is $(1.86 \pm 0.09) \times 10^{-3}$. In the same y-$p_T$ range the raw yield of the Θ^{++}

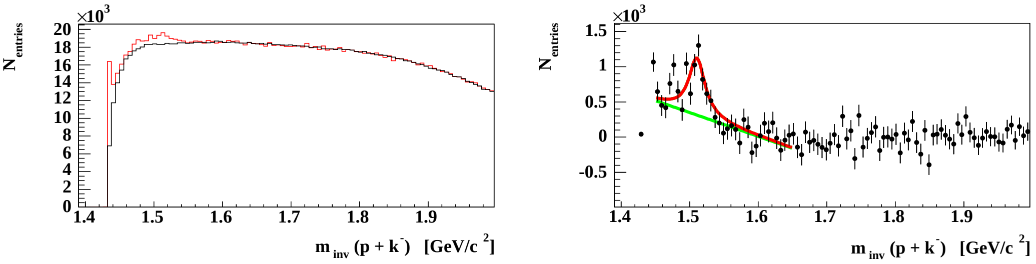

(a) (b)

Figure 7.17: (**a**) Invariant mass spectrum of the $\Lambda(1520)$ (red curve) and mixed event background (black curve) in d+Au collisions. (**b**) Invariant mass spectrum of the $\Lambda(1520)$ after the mixed event background subtraction. A Breit-Wigner plus a line is fit to describe the $\Lambda(1520)$ peak and the background, respectively.

is $(0.07 \pm 0.02) \times 10^{-3}$ per event. If we ignore the difference due to charge efficiency corrections and assume that the branching ratio of $\Theta^{++} \rightarrow p + K^{+}$ is 100% then the ratio of the hypothesized Θ^{++} pentaquark signal to the $\Lambda(1520)$ baryon signal is 0.04 ± 0.01 in d+Au collisions at $\sqrt{s_{\rm NN}} = 200$ GeV.

7.6 Simulation Studies for the Θ^{++} Pentaquark Background

The population above the background in the invariant mass spectrum of the proton and K^{+} meson can be tested with MC simulations for contaminations of the correlated background. The Δ^{++} baryon is the only doubly charged, well established particle in the Particle Data Group [39]. Since a Δ^{++} baryon decays into a proton and a π meson, π mesons from the decays of Δ^{++} baryons that are misidentified as K mesons can cause a background that cannot be subtracted using the mixed event technique.

For each event in this study, one Monte Carlo Δ^{++} is chosen from a thermal exponential distribution with T = 300 MeV in the rapidity interval $\mid y \mid < 1$. Figure 7.18-a presents the MC simulated invariant mass distribution of the Δ^{++} (black curves) and the contribution of the misidentified Δ^{++} decay to the invariant mass spectrum of the Θ^{++} (red curves). A smooth population over the background can be observed in the mass region 1.44 - 1.54 GeV as seen in Figure 7.18-a. The momentum cuts are applied as in the real data, presented in Table 7.5, for the selected protons and K mesons. For a more realistic contribution of the misidentified π mesons since the dE/dx information cannot be simulated properly, specific momentum cuts are applied in the region where the Bethe-Bloch curves for π and K mesons merge. Figure 7.18-b presents the contributions from Δ^{++} decay when the momentum of the decay π is within the merging region ($0.6 < \text{Momentum}_{\pi} < 0.8$ GeV/c). A narrower peak at 1.48 GeV/c^2 is observed which accounts for 0.7% of the simulated input Δ^{++} baryon. This population is consistent with the observation of the background in Figure 7.16 that is represented with a line in the kinematic cut of region. In Figure 7.15, the invariant mass spectrum for the Θ^{++} shows the un-subtracted correlated background in the same mass region at around 1.48 GeV/c^2. When the same cuts are applied described in Table 7.5 for the proton and π meson candidates (K cuts are applied on π), the raw counts of Δ^{++} baryons amount to 0.039 ± 0.003 per event [14]. If we assume no detector resolution effects, then 0.7% of these counts, (i.e.,$(0.27 \pm 0.02) \times 10^{-3}$ per event), populate the invariant mass spectrum of the Θ^{++} with a peak at 1.48 GeV/c^2. While the population around the kinematic cutoff mass region can be explained with misidentified Δ^{++}, the population at the mass 1.54 GeV/c^2 region cannot be described by this Δ^{++} contribution.

7.7 Conclusions

Assuming that the Θ^+ production is $10-100\%$ of the $\Lambda^*(1520)$ in p+p collisions, one can estimate the yield of the Θ^+. The preliminary dN/dy of $\Lambda^*(1520)$ at mid-rapidity is 0.004 per event in p+p collisions [69, 70]. There are 10 Million p+p events available for this analysis and this corresponds to a production of $\sim$ 40000 $\Lambda^*(1520)$, giving a production range of $\sim$ 4000 to $\sim$ 40000 Θ^+'s in these p+p events using the above estimates. As the efficiency of the mixing technique is 3% and the branching ratio of the $\Theta^+ \rightarrow K^0_S + p$ is $\sim$ 25% (assuming that the branching ratios of $\Theta \rightarrow K^0_S + p$ and $\Theta^+ \rightarrow K^+ + N$ are each 50%), 30-300 of the Θ^+'s should be found. The background pairs per event in the 1.54±5 MeV mass range is 3200 [71]. This corresponds to

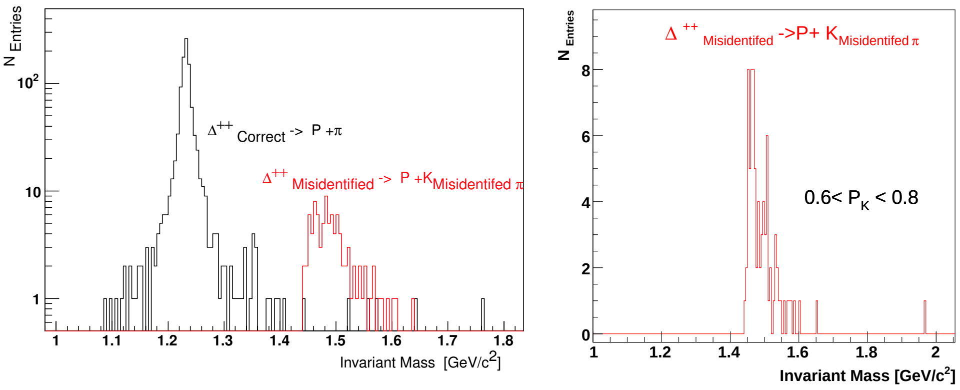

(a) (b)

Figure 7.18: (**a**) The black histogram presents the MC simulated Δ^{++} and the red histogram the misidentified Δ^{++}. (**b**) Contribution of misidentified Δ^{++} from the selected momentum range.

a significance of between 0.25 and 3. Similarly one can repeat the same study for Au+Au and d+Au collisions and correspondingly predict a significance of 2-7 for 1.5 Million Au+Au events and 1-16 for 10 Million d+Au for the predicted production of one Θ^{+} per unit rapidity per collision [59, 60, 61, 62]. To estimate the yield for the d+Au collisions we assume scaling with the number of participants (N_{part}). The mean number of participants in d+Au is 8, in p+p it is 2, and in Au+Au it is 350 for the most central collisions. The lower limit is obtained from p+p scaling while the upper limit is from Au+Au yield estimates. The invariant mass spectra reconstructed with the HCT for the Θ^{+} in d+Au collision events are consistent with our estimations for the significance of the signal given our current statistics.

For both Θ^{+} and Θ^{++} pentaquarks the significance of the population over the background in the best signals do not exceed 4σ. Although this is clearly a matter of opinion, due to spurious signals from noise typically the 5σ standard is used as a rough rule of thumb to define the sensitivity necessary for discovery.

Chapter 8

Conclusions

In this final chapter, the $\Sigma^*(1385)$ measurement results from p+p, d+Au and Au+Au collisions are discussed in comparison to other resonances and strange particles. Thermal model fits are performed to extract the kinematics of the collisions in terms of temperature, chemical potentials and the size of the source.

8.1 Discussion

The $\Sigma^*(1385)$ baryons and anti-baryons are identified in minimum bias p+p and d+Au and the 0-5% most central Au+Au collisions at $\sqrt{s_{\mathrm{NN}}} = 200$ GeV. The $\mathrm{p_T}$ spectra and $\langle p_T \rangle$ are measured in all three collision environments. Table 8.1 summarizes the findings from the corrected spectra of the $\Sigma^*(1385)$. The inverse slope parameters, $\langle p_T \rangle$ and yields of the $\Sigma^*(1385)$ for each collision system are presented with statistical and systematic errors.

Due to the similar strangeness quark content of the Λ and $\Sigma^*(1385)$ baryons, the ratio $\Sigma^*(1385)/\Lambda$ is independent of strangeness enhancement effects. The collision energy dependence of the $\Sigma^*(1385)^{\pm}/\Lambda$ ratios is presented in Figure 8.1. The ratio is constant at ~ 0.25 above 6 GeV center of mass energies in p+p collisions. Since the $\Sigma^*(1385)$ has never been studied with heavy ion collisions previously, the first measurement from Au+Au collisions is presented in this thesis. The $\Sigma^*(1385)^{\pm}/\Lambda$ ratio in Au+Au collisions is the same within errors as that in p+p collisions. No

Table 8.1: Mean $\mathrm{p_T}$ $\langle p_T \rangle$, and yield (dN/dy) from exponential fits to the p_T spectra of $\Sigma^*(1385)$ in minimum bias p+p and d+Au and 0-5% most central Au+Au collisions at $\sqrt{s_{\mathrm{NN}}} = 200$ GeV.

	$\langle \mathrm{p_T} \rangle$ [MeV/c]	dN/dy
$\Sigma^*(1385)^{\pm}$ on min-bias p+p	$1.02 \pm 0.02 \pm 0.07$	$(1.07 \pm 0.04 \pm 0.14) \times 10^{-2}$
$\overline{\Sigma^*}(1385)^{\pm}$ in min-bias p+p	$1.01 \pm 0.01 \pm 0.06$	$(0.90 \pm 0.04 \pm 0.12) \times 10^{-2}$
$\Sigma^*(1385)^{\pm}$ in min-bias d+Au	$1.14 \pm 0.05 \pm 0.08$	$(3.23 \pm 0.15 \pm 0.42) \times 10^{-2}$
$\overline{\Sigma^*}(1385)^{\pm}$ in min-bias d+Au	$1.12 \pm 0.05 \pm 0.08$	$(3.15 \pm 0.15 \pm 0.41) \times 10^{-2}$
$\Sigma^*(1385)^{\pm} + \overline{\Sigma^*}(1385)^{\pm}$ in 0-5% Au+Au	$1.28 \pm 0.15 \pm 0.09$	$9.35 \pm 1.38 \pm 1.25$

suppression or enhancement of the $\Sigma^*(1385)$ with respect to the Λ is observed.

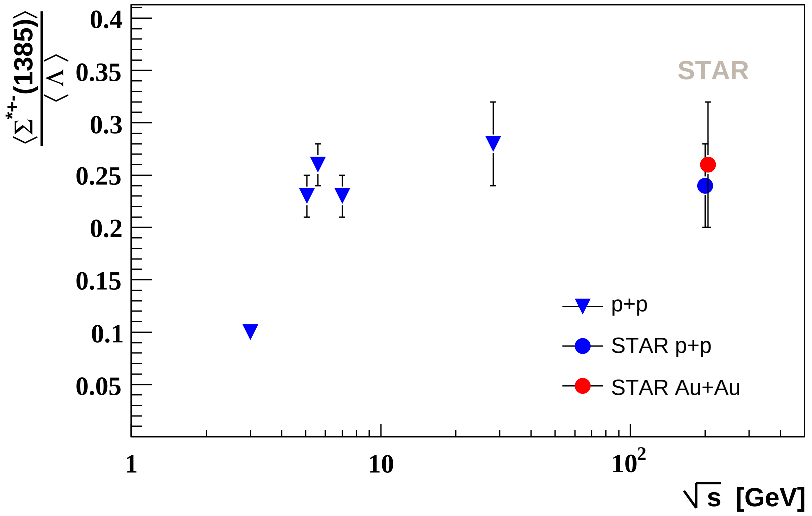

Figure 8.1: The energy dependence of the $\Sigma^*(1385)^{\pm}/\Lambda$ ratios in p+p and Au+Au collisions.

A comparison of the $\langle p_T \rangle$ as a function of particle mass measured in the STAR experiment is presented in Figure 8.2 for p+p and Au+Au collisions at $\sqrt{s_{NN}} = 200$ GeV. The $\langle p_T \rangle$ measurement of the $\Sigma^*(1385)$ extends the $\langle p_T \rangle$ measurements of the STAR experiment into higher mass regions. The triangles represent the short-lived resonances and the circles signify long-lived 'stable' particles. The behavior of $\langle p_T \rangle$ vs. mass for the various particles in p+p and Au+Au collisions is compared to two parameterizations. The black curve is an empirical fit to the ISR π, K, and p data in p+p collisions and the band is a blastwave fit using π, K, and p in STAR for Au+Au collisions [72, 73]. The empirical parametrization for the ISR data at $\sqrt{s} =$ 25 GeV in p+p collisions, can describe the behavior of the lower mass particles, such as π, K, and p, despite the fact that our collision energy is one order of magnitude higher. However, this empirical parametrization does not reproduce the behavior of the higher mass particles in p+p collisions. Similarly, the blastwave parametrization which can describe the lower mass particles ($\sim$ 98% of all the particles observed) in Au+Au collisions, fails to explain the behavior of higher mass particles.

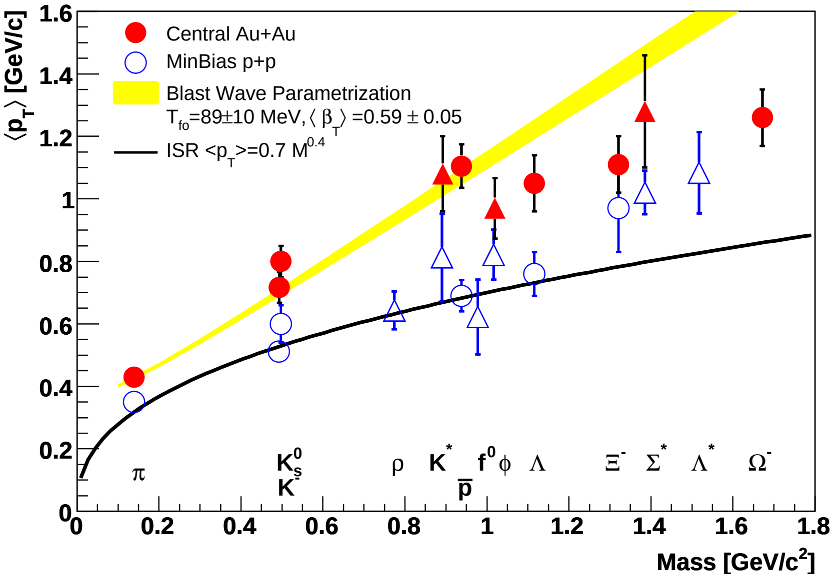

Figure 8.2: The $\langle p_T \rangle$ vs particle mass measured in p+p and Au+Au collisions at $\sqrt{s_{NN}} = 200$ GeV. The black curve represents the ISR parametrization from π, K, and p for $\sqrt{s_{NN}} = 25$ GeV p+p collisions. The yellow band is the blastwave fit using π, K, and p for the central Au+Au collisions.

The heavy particles in p+p and Au+Au collisions show a similar magnitude of $\langle p_T \rangle$. It is expected that resonances with higher transverse momentum are more likely to be reconstructed because of their longer relative lifetimes due to their relativistic velocities. This means they are more likely to decay outside the medium and hence their daughter particles will interact less with the medium in Au+Au collisions. Any loss of low p_T $\Sigma^*(1385)$ baryons will cause an increase in the measured $\langle p_T \rangle$ of the observed p_T spectra for the central Au+Au collisions with respect to p+p collisions. However we do not see any significant increase in the $\langle p_T \rangle$ for the $\Sigma(1385)$ from minimum bias p+p to the most central Au+Au collisions within the statistical and systematic errors.

It is possible that the production of the higher mass particles in p+p collisions is biased towards smaller impact parameter collisions. If the higher mass particles are produced in more violent (mini-jet) p+p collisions compared to lower mass particles, the $\langle p_T \rangle$ for heavy particles in p+p collisions would be larger. It is possible

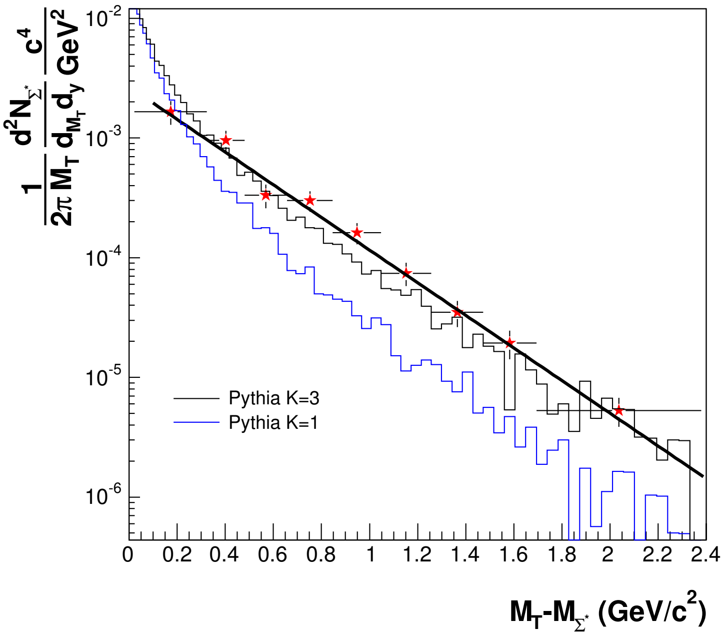

Figure 8.3: Comparison of the $\Sigma^*(1385)$ spectrum with Pythia predictions for two different values of the K factor. See text for details.

to model hard subprocesses, parton showers, beam remnants and underlying events, fragmentation, and decays with Pythia which is a pQCD event simulation model [74]. A comparison of the $\Sigma^*(1385)$ spectrum with a leading order pQCD model, Pythia

6.3, is presented in Figure 8.3. As can be seen in Figure 8.3 it is possible to model the $\Sigma^*(1385)$ spectrum with Pythia with the factor K=3 while the default (K=1) spectrum is too soft.

This K-factor, which represents a simple factorization of next-to-leading order processes (NLO) in the Pythia leading order (LO) calculation, is directly related to the $\mathrm{p_T}$ spectrum. An increase in the K factor implies that larger NLO contributions (mini-jet events) are required to describe the $\Sigma^*(1385)$ production. The high K=3 factor is also needed to describe heavy strange baryons such as the Λ and the Ξ, while the spectra predicted with this high K factor is too hard for the light mesons [75]. In Au+Au collisions there is evidence that heavier particles flow radially with a smaller boost velocity due to their smaller cross section than the lighter mass particles (such as π mesons). These two independent effects in p+p and Au+Au collisions may cause the apparent merging of the $\langle p_T \rangle$ which is corroborated by the $\Sigma^*(1385)$ measurement.

The resonance production also presents an important test of thermal production and microscopic models. The ratio of resonances to their stable particles is insensitive to fugacities and phase space occupancies [7]. For example $\Sigma^*(1385)/\Lambda = (\lambda_s\lambda_u\lambda_u)/(\lambda_s\lambda_u\lambda_d) = \exp(\frac{\mu_u-\mu_d}{T}) = 1$ since $\mu_u \sim \mu_d$. Predictions of a thermal model in comparison to the measured particle ratios in p+p collisions at $\sqrt{s_{\mathrm{NN}}} = 200$ GeV are presented in Figure 8.4. The fit parameters are $T_{ch} = 171 \pm 9$ MeV, $\gamma_s = 0.53 \pm 0.04$ and radius of the source $r = 3.49 \pm 0.97$ fm. The quantum numbers baryon (B) and charge (Q) are fixed to 2 while strangeness (S) is fixed to 0. The short lines represent the thermal model predictions from a canonical calculation performed by Thermus V2.0 for the best overall fit to the ratios presented in Figure 8.4. The closed circles represent the particle ratios measured in p+p collisions. The model accurately describes both the stable particle and resonance ratios in p+p collisions. The 1 σ deviations of the ratios and model predictions are also included in the plot. The deviations do not exceed 2 σ.

Figure 8.5 presents the particle ratios and Thermus V2.0 predictions for the most central Au+Au collisions at $\sqrt{s_{\mathrm{NN}}} = 200$ GeV. The measured ratios are used to predict the free parameters by using a grand canonical approach. The fit parameters are $T_{ch} = 168 \pm 6$ MeV, $\gamma_s = 0.92 \pm 0.06$, $\mu_B = (4.52 \pm 0.98) \times 10^{-2}$, $\mu_S = (2.23 \pm$

0.74) × 10^{-2}, $\mu_Q = (-2.05 \pm 0.77) \times 10^{-2}$, and $r = 15 \pm 10$ fm. The model describes the stable particle ratios within a deviation of 1 σ. Except for the $\Lambda(1520)/\Lambda$ ratio, the other resonances ratios measured (ϕ/K^*, $\Sigma^*(1385)/\Lambda$) are within a 1 σ error of the model fits. Regeneration and re-scattering are not included in this thermal model which might explain why the experimental values differ from the statistical model calculations for the $\Lambda(1520)/\Lambda$ ratio. It is expected that there should be no re-scattering and regeneration affects on the ϕ meson due to its long life time. Since the model predicts the ratios for $\Sigma^*(1385)$ and K^* correctly the re-scattering is equilibrated with the regeneration affects.

In Au+Au collisions the free fit parameter corresponding to strangeness saturation, γ_s , is higher than in p+p collisions while T is the same within the errors. In

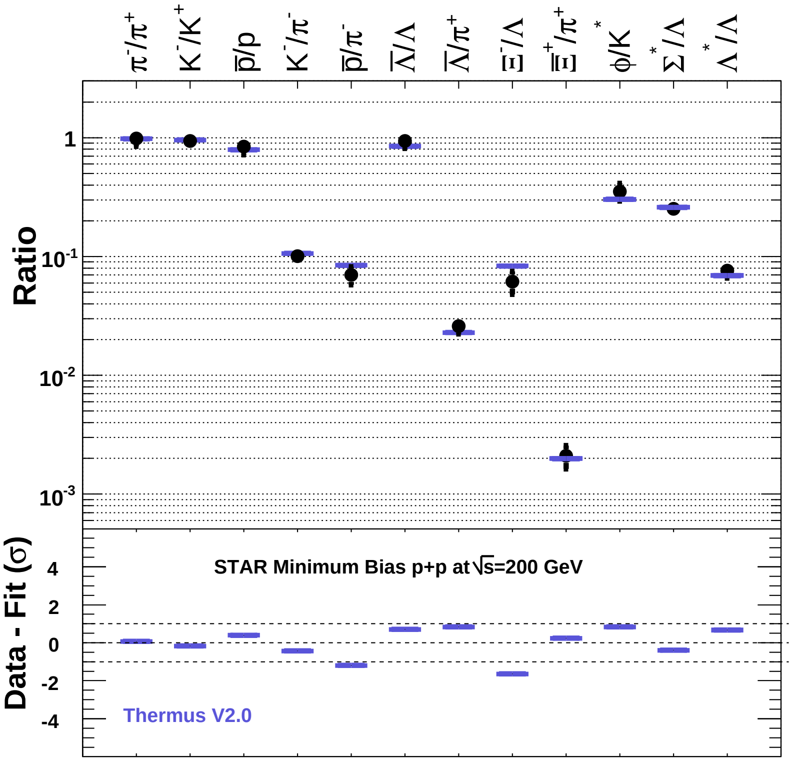

Figure 8.4: Particle ratios in $\sqrt{s_{NN}}$ = 200 GeV p+p collisions in comparison to canonical thermal model predictions (short lines) from Thermus V2.0 [76]. The fit parameters are $T_{ch} = 171 \pm 9$ MeV, $\gamma_s = 0.53 \pm 0.04$ and $r = 3.49 \pm 0.97$ fm. B and Q are fixed to 2 while S is fixed to 0. See text for details.

Figure 2.2-a, the energy and system size dependence of the measured K/π ratios were presented. An enhancement is observed in the K/π ratios in central Au+Au collisions relative to elementary collisions implying an increase in strangeness production resulting in larger values of γ_s. The higher γ_s in Au+Au relative to p+p collisions is in agreement with the K/π ratio observations. Due to this increase of strangeness production when a comparison is made between p+p and Au+Au collisions, particle ratios are selected such that μ_s cancels out (e.g., $\Sigma^*(1385)/\Lambda$ ratio). The small value of the chemical potential, μ_B, can be explained by the proximity of the measured $\overline{\Sigma^*}(1385)/\Sigma^*(1385)$ ratios to unity and it reflects the near zero net baryon number at mid-rapidity of Au+Au collisions.

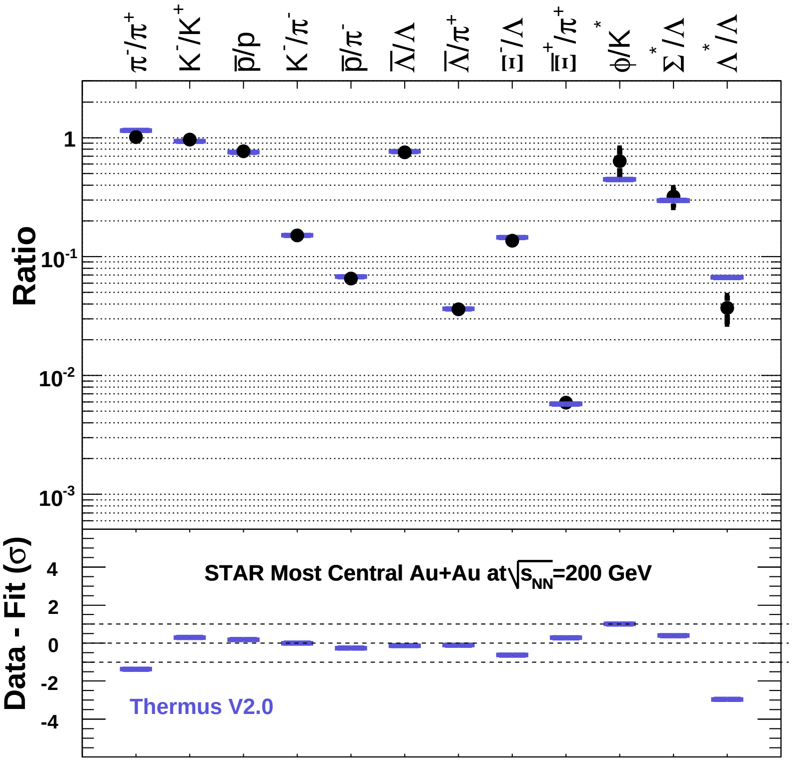

Figure 8.5: Particle ratios in the $\sqrt{s_{NN}}$ = 200 GeV most central Au+Au collisions in comparison to a grand canonical thermal model predictions (short lines) from Thermus V2.0 [76]. The fit parameters are $T_{ch} = 168 \pm 6$ MeV, $\gamma_s = 0.92 \pm 0.06$, $\mu_B = (4.52 \pm 0.98) \times 10^{-2}$, $\mu_S = (2.23 \pm 0.74) \times 10^{-2}$, $\mu_Q = (-2.05 \pm 0.77) \times 10^{-2}$, and $r = 15 \pm 10$ fm. See text for details.

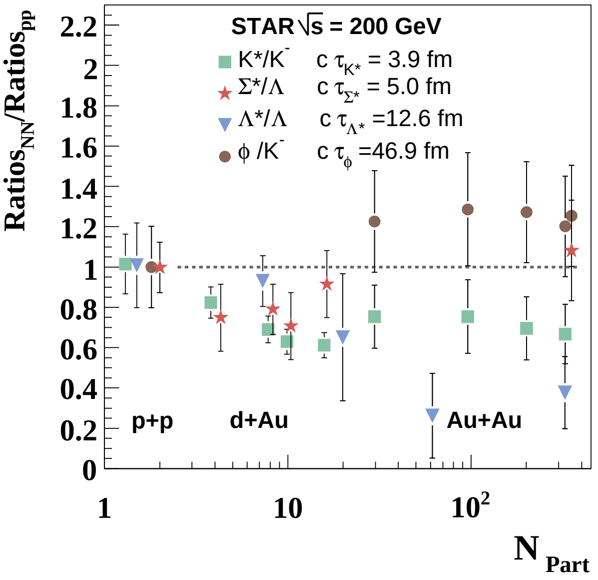

Figure 8.6: Resonance to stable particle ratios of ϕ/K^-, K*(892)/K$^-$, $\Sigma(1385)/\Lambda$ and $\Lambda(1520)/\Lambda$ in d+Au and Au+Au collisions normalized by their ratios in p+p collisions at $\sqrt{s_{\mathrm{NN}}} = 200$ GeV. Statistical and systematic errors are included.

Figure 8.6 shows the ratio of strange resonances to their corresponding stable particles normalized to measured values in p+p. The $\Sigma(1385)/\Lambda$ ratio is independent within errors of system size (represented by N_{Part}) at 200 GeV and is consistent with lower energy p+p values. The other resonance ratios, such as K*/K and $\Lambda(1520)/\Lambda$, behave differently and exhibit a slight suppression in Au+Au collisions, independent of centrality. Due to their short lifetimes, the re-scattering of resonance decay products during the time between chemical and thermal freeze-out is expected to cause a loss of signal. While the observed suppression of K*/K and $\Lambda(1520)/\Lambda$ corroborates the re-scattering picture, the lack of suppression of the $\Sigma(1385)/\Lambda$ ratio implies a recovery mechanism such as regeneration (e.g. $\Lambda + \pi \rightarrow \Sigma(1385)$). The total interaction cross-sections with π increases from K to p to π respectively [39]. This implies that re-scattering of the K* decaying into π and K in the medium should be higher than that of the $\Lambda(1520)$ decaying into K and p. The shorter lifetime of the K* also enhances the re-scattering probability of its decay particles. In this scenario, assuming that the time span between chemical and thermal freeze-out is non-zero, the regeneration cross-section of the K* must be larger than that of the $\Lambda(1520)$ due to the observed smaller suppression of the K* ratios.

A comparison between measured resonance ratios may yield an estimation of the lifetime of the fireball. The degree of re-scattering is dependent not only on the lifetime of the resonances but also on the duration between the chemical and thermal freeze-outs. Since the extracted temperatures of the fireballs are the same within errors for the p+p and Au+Au collisions from the THERMUS V2.0 thermal model, the ratio of resonances in p+p collisions must be same as those in Au+Au collisions at chemical freeze-out. The lifetime between chemical and thermal freeze-out can be extracted with

$$(\frac{Resonance}{StableParticle})_{kinetic} = (\frac{Resonance}{StableParticle})_{chemical} \times e^{-\Delta t/\tau} \tag{8.1}$$

for τ the lifetime of the resonance, under the assumption that all resonances that decay before kinetic freeze-out are lost and there is no regeneration mechanism. The measurements of the resonance ratios are presented in Table 8.2 for K^*, $\Sigma^*(1385)$ and $\Lambda(1520)$ in minimum bias p+p and the most central Au+Au collisions at $\sqrt{s_{\rm NN}} = 200$ GeV. The lifetimes can be extracted as $\Delta t = 2 \pm 1\ fm/c$ from K^* and $\Delta t = 12 \pm 6\ fm/c$ from $\Lambda(1520)$ by using Equation 8.1 and Table 8.2. Since no suppression is observed for $\Sigma^*(1385)$ in Au+Au with respect to p+p collisions the Δt is consistent with 0 fm/c and the sudden freeze-out picture.

Table 8.2: The resonance ratios for K^*/K^-, $\Sigma^*(1385)/\Lambda$ and $\Lambda(1520)\Lambda$ from feed-down corrected Λ yields in p+p and Au+Au collisions at $\sqrt{s_{\rm NN}} = 200$ GeV. K^* and $\Lambda(1520)$ ratios are from [11] and [77], respectively.

Particle	min-bias p+p	Central Au+Au
K^*/K	0.35 ± 0.06	0.23 ± 0.06
$\Sigma^*(1385)^{\pm}/\Lambda$	0.29 ± 0.05	0.30 ± 0.06
$\Lambda(1520)/\Lambda$	0.09 ± 0.02	0.04 ± 0.02

Thermal model predictions of the dependence of the lifetime and freeze-out temperature of the source on the resonance ratios are presented for $\Sigma^*(1385)/\Lambda$ and $\Lambda(1520)/\Lambda$ ratio in Figure 8.7-a, and for K^*/K and $\Lambda(1520)/\Lambda$ in Figure 8.7-b [7].

The experimentally observed K^*/K^- ratio with green and $\Lambda(1520)/\Lambda$ ratios with blue lines are included in the plots. Since the spin degeneracy is small, the $\Sigma^*(1385)^{\pm 0}/\Lambda$ ratio (red lines) can be calculated as 0.45 ± 0.09. Assuming no regeneration only re-scattering and a chemical freeze-out temperature of 168 MeV (extracted from THERMUS V2.0 for the Au+Au collisions), it is possible to estimate lower limits for the time spans between chemical and thermal freeze-out. These are $\Delta\tau > 3$ fm/c from the K^*/K and $\Delta\tau > 10$ fm/c from the Λ^*/Λ. The $\Sigma(1385)/\Lambda$ ratio is consistent with $\Delta\tau = 0$ fm/c. A simple extraction of these life spans using Equation 8.1 is equivalent with these from Figure 8.7. It is possible that different particles freeze-out at different temperatures. For such a sequential freeze-out picture the time span between chemical and thermal freeze-out is valid for only that specific particle.

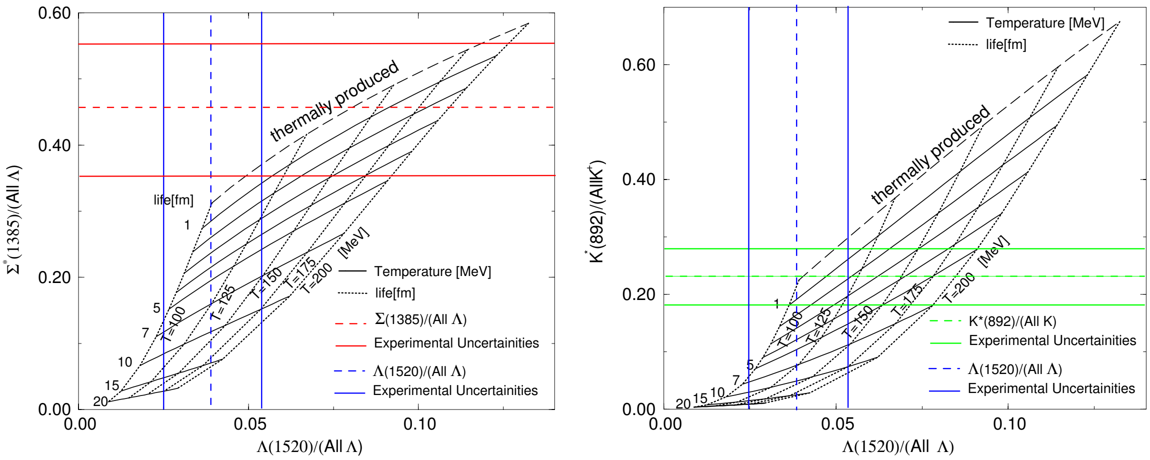

(a) **(b)**

Figure 8.7: Curves of the lifetime and T dependence for **(a)** $\Sigma^*(1385)/\Lambda$ versus $\Lambda(1520)/\Lambda$, and **(b)** K^*/K versus $\Lambda(1520)/\Lambda$ from [7]. The measurements of the ratios and their uncertainties, $\Sigma^*(1385)/\Lambda$ with red lines, $\Lambda(1520)/\Lambda$ with blue lines and K^*/K with green lines, are included.

If the time between the chemical and thermal freeze-outs is small (smaller than the lifetime of the resonance), re-scattering of the decay products of resonances should be negligible. In a sudden freeze-out case, it is still possible to explain the observed suppression of the $\Lambda(1520)/\Lambda$ as due to a high partial wave component of the $\Lambda(1520)$, without a re-scattering and regeneration picture. Even though the valence quarks of the $\Lambda(1520)$ are in an $\mathrm{L} = 1^{-}$ state, it must decay through a relative momentum $\mathrm{L} = 2$ process in order to conserve isospin [32]. While the number of channels that the $\Lambda(1520)$ can decay into is reduced due to isospin conservation, the high relative angular momentum and threshold suppress the decay phase space.

Resonance to stable particle ratios can be used to test microscopic (UrQMD) models that include re-scattering and regeneration. The UrQMD model prediction in Figure 8.8 shows the collision energy dependence of the $\Sigma^{*}(1385)/\Lambda$ ratios for Au+Au collisions. A comparison to experimentally measured ratios can be made with Figure 8.1. The measured $\Sigma^{*}(1385)/\Lambda$ ratio in the $0-5\%$ most central Au+Au collisions is below the UrQMD prediction at $\sqrt{s_{NN}} = 200$ GeV. Since the $\pi + \Lambda$ cross sections are not experimentally available, UrQMD implements the $\pi + p$ cross sections instead, to estimate the regeneration cross section of the $\Sigma^{*}(1385)$. The difference between the predicted and the experimental ratio can be due to these differences in the cross sections used in UrQMD for the regeneration of $\Sigma^{*}(1385)$ or due to a predicted shorter lifetime of the initial fireball. However it is also important to note that the Λ yields predicted by UrQMD calculations are also 50% less than the experimental values. This model must be revised in light of these measurements.

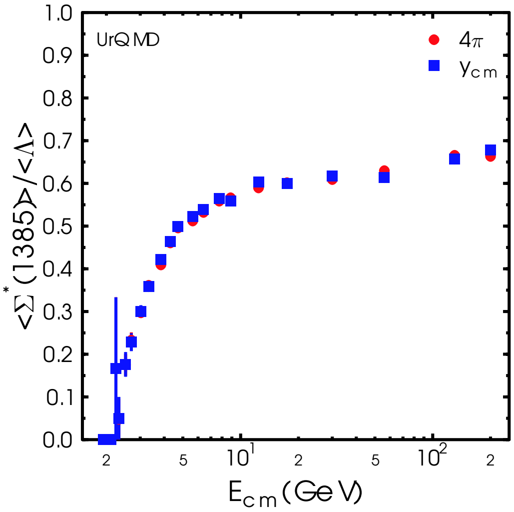

Figure 8.8: Collision energy dependence of the $\Sigma^{\pm 0}(1385)/\Lambda$ ratios for Au+Au collisions predicted by the microscopic model UrQMD. Plot from M. Bleicher [78].

8.2 Nuclear Effects

The nuclear modification factor (see Section 2.3 for definitions) for the $\Sigma^*(1385)$ in comparison to other mesons and baryons in d+Au collisions can be found in Figure 8.9. The R_{dAu} measurements, for mesons on the left and for baryons on the right, follow participant scaling at low momenta. Baryons show a greater enhancement over binary scaling for the higher momenta than do mesons. The $\Sigma^*(1385)$ baryon follows a similar trend as the other strange baryons, Λ and Ξ. The enhancement over binary scaling can be explained by the Cronin effect which is a generic term for the experimentally observed broadening of the transverse momentum distributions at intermediate $\mathrm{p_T}$ in p+A collisions as compared to p+p collisions. It is surprising that the ρ measurement shows no enhancement above the binary collisions and even falls below π meson, while the other resonances and their stable particles show no clear difference in their R_{dAu}.

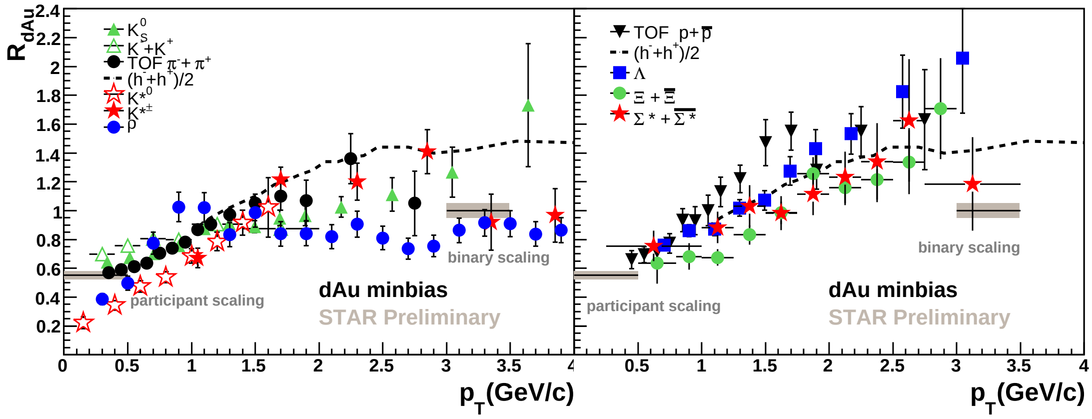

Figure 8.9: Nuclear Modification factors for the $\Sigma^*(1385)$ in comparison to other mesons on the left and baryons on the right in d+Au collisions.

The nuclear modification factors of Ξ, Λ, p, Φ, K_S^0, and $(\mathrm{h}^+ + \mathrm{h}^-)/2$ for the 0-5% most central Au+Au collisions can be found in Figure 8.10. There are distinct differences between the R_{dAu} and the R_{AA} measurements for all particles. There is an enhancement in the mid $\mathrm{p_T}$ region above binary scaling for the p, $(\mathrm{h}^+ + \mathrm{h}^-)/2$, Ξ and Λ baryons. The observed enhancement of strange baryons compared to protons in the intermediate p_T must be due to canonical suppression of strangeness in p+p collisions. The smaller value of γ_s in p+p collisions and the observed increase in Au+Au collisions supports the picture of canonical suppression of the strangeness in p+p collisions. It is important to compare the observed ordering with the nuclear modification factors of baryonic resonance measurements of the same quark content but with different masses to distinguish species and mass dependent effects. Due to the limited statistics available in FY02 for Au+Au collisions, the R_{AA} measurement of the $\Sigma^*(1385)$ has large error bars (of the order of 2) hence it is not included in this plot. The R_{AA} measurement of the $\Sigma^*(1385)$ with smaller error bars and more bins with a factor of 10 higher statistics is expected with the data from FY04 Au+Au collisions.

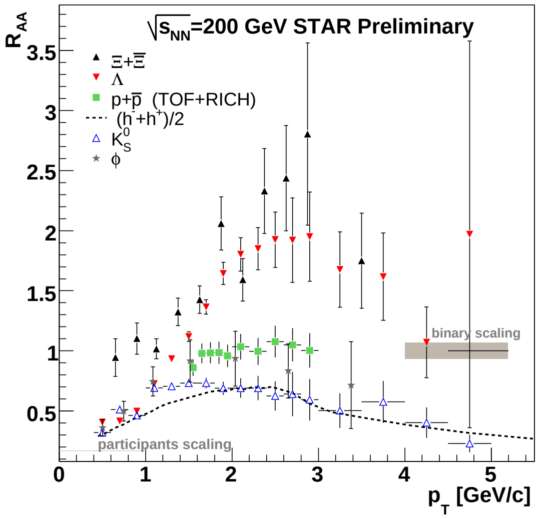

Figure 8.10: Nuclear Modification factor from the 0-5% most central Au+Au divided by normalized minimum bias p+p collisions.

8.3 Conclusions

The identification techniques of the $\Sigma^*(1385)$ baryon and anti-baryon and the corrected momentum spectra, yields and $\langle p_T \rangle$ from identified $\Sigma^*(1385)$ are reported in p+p d+Au and Au+Au collisions at $\sqrt{s_{\rm NN}}$ = 200 GeV. When the $\Sigma^*(1385)$ yields are compared with the Λ baryon yield, to cancel effects of strangeness suppression in p+p collisions, no significant suppression due to re-scattering or enhancement due to regeneration effects is observed. This picture is consistent with a sudden freeze-out picture where the time between chemical and thermal freeze-out is negligible.

The existence of the pentaquarks, Θ^{+} and Θ^{++}, was investigated in d+Au collisions using various techniques. The results for the Θ^{+} and Θ^{++} pentaquarks exhibit significances of the measured population above background that do not exceed 4σ. Although clearly a matter of opinion, due to spurious signals from noise, typically a 5σ significance standard is used, as rough rule of thumb, to define the sensitivity required for discovery. Hence the significance of the signal in our measurements is insufficient to claim discovery.

8.4 Future Directions

These measurements will be improved significantly with the higher statistics available in the Au+Au run of FY04. A factor of 10 increase in the statistics make it feasible to perform a study of the centrality dependence of the $\Sigma^{*}(1385)$ measurement. This is essential to be able to measure the nuclear modification factors from Au+Au collisions and investigate further whether the dependence observed in R_{AA} is due to strangeness or mass ordering.

The most recent run at RHIC concentrated on studying matter in less dense, smaller systems i.e., Cu+Cu, over a range of energies in order to separate various physics contributions. This data set will probe a regime of greater density than p+p and d+Au but below that of the current high density Au+Au collisions. Since jets are the predominant form of particle production in p+p and a larger density is involved but no QGP is expected in d+Au this enables analyses over a wide but well sampled range of nuclear density and provides key input for critical tests of current theories.

Appendix A

Kinematic Variables

Some kinetic variables such as transverse momentum, rapidity and pseudorapidity are used to simplify the discussions for all reference frames in relativistic heavy ion collisions. In this Appendix A these essential terminologies will be introduced. Details on light cone variables can be found elsewhere [80].

The coordinate system is defined so that x and y are the azimuthal components of the particles and z is the beam direction. The transverse momentum of a particle is therefore defined as

$$p_T = \sqrt{p_x^2 + p_y^2}. \tag{A.1}$$

Similarly the transverse mass, $\mathrm{m_T}$, for a particle with mass m_0 is defined as

$$\mathrm{m_T} = \sqrt{{m_0}^2 + \mathrm{p_T}^2}. \tag{A.2}$$

The rapidity, y, is a dimensionless quantity and is related to the forward momentum of a particle. The rapidity variable is frequently used in heavy ion physics due to its additive property under Lorentz transformations along the beam direction and is defined as

$$y = \frac{1}{2}\ln(\frac{E + p_z}{E - p_z}), \tag{A.3}$$

where E is the particle energy.

Pseudorapidity, η, is another convenient variable to characterize the detected particles for experiments that only measure the angle of the detected particle relative to the beam axis. Pseudorapidity is defined as

$$\eta = -\ln[\tan(\theta/2)] \tag{A.4}$$

where θ is the angle between the particle momentum $\overrightarrow{p}$ and the beam axis. It can be also written in terms of momentum as

$$\eta = \frac{1}{2}\ln(\frac{|p| + p_z}{|p| - p_z}). \tag{A.5}$$

When the pseudorapidity variable in the form of Equation A.5 is compared to the rapidity variable in the form of Equation A.3, it can be seen that they coincide for $|p| \sim E$, i.e when the momentum is large.

Appendix B

Invariant Mass Spectra of the $\Sigma^*(1385)$

The individual invariant mass spectra for the specified p_T bins of $\Sigma^*(1385)$ in p+p, Au+Au and d+Au collisions at $\sqrt{s_{NN}} = 200$ GeV. The raw counts of the signals are extracted from bin counting and later corrected as discussed in Chapter 5 to measure the total production yields.

Figure B.1 shows the first 3 p_T bins of the $\Sigma^*(1385)$ invariant mass spectra before and after mixed-event background subtraction. While the rapidity coverage of the $\Sigma^*(1385)$ is $|y| < 0.75$ for all plots in Figure B.1, the p_T ranges are 0.25-1, 1-1.25, 1.25-1.5 GeV/c starting from the top figure down to the bottom one.

Figure B.2 shows the next 3 p_T bins of the $\Sigma^*(1385)$ invariant mass spectra before and after mixed-event background subtraction. The rapidity coverage of the $\Sigma^*(1385)$ is $|y| < 0.75$ for all plots in Figure B.2 and the p_T ranges are 1.5-1.75, 1.75-2, 2-2.25 GeV/c starting from the top figure down to the bottom one.

Figure B.3 shows the last 3 p_T bins of the $\Sigma^*(1385)$ invariant mass spectra before and after mixed-event background subtraction. The rapidity coverage of the $\Sigma^*(1385)$ is $|y| < 0.75$ for all plots in Figure B.3 and the p_T ranges are 2.25-2.5, 2.5-2.75, 2.75-3.5 GeV/c starting from the top figure down to the bottom one.

The $\overline{\Sigma^*}(1385)$ invariant mass spectra for the same p_T cut ranges as the $\Sigma^*(1385)$ in the rapidity range $|y| < 0.75$ are presented in Figures B.4, B.5 and B.6.

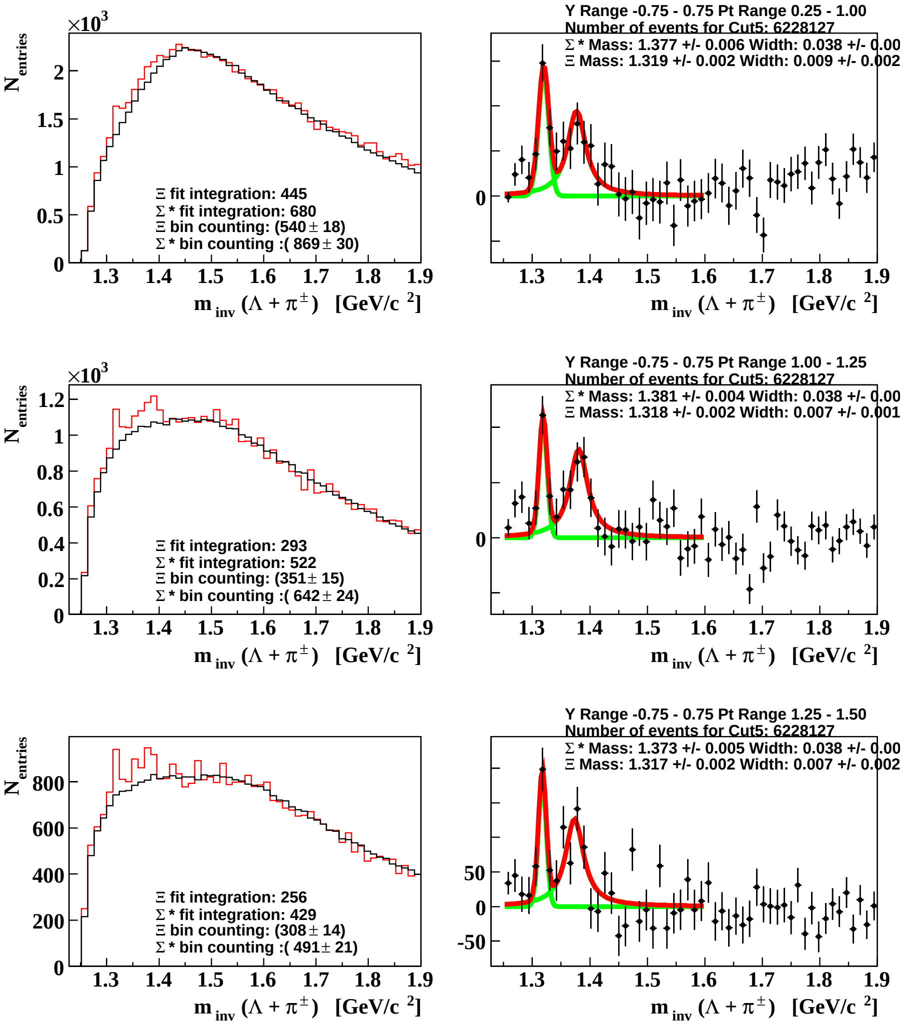

(a) **(b)**

Figure B.1: The individual invariant mass spectra for the specific p_T bins of $\Sigma^*(1385)$ (**a**) before the mixed event background subtraction and (**b**) after the mixed event background subtraction in minimum bias p+p collisions. A Gaussian for Ξ and Breit-Wigner for the $\Sigma^*(1385)$ are fit to the background subtracted spectra.

Due to the limited statistics the $\Sigma^*(1385)$ and $\overline{\Sigma^*}(1385)$ invariant mass histograms are added to improve the significance of the $\Sigma^*(1385)$ mass peaks in the 0-5% most central Au+Au collisions. Figure B.7 and Figure B.8 shows the 5 p_T bins of $\Sigma^*(1385)$ invariant mass spectra before and after mixed-event background subtraction. The rapidity coverage of the $\Sigma^*(1385)$ is $|y| < 0.75$ for all histograms in Figure B.7 and

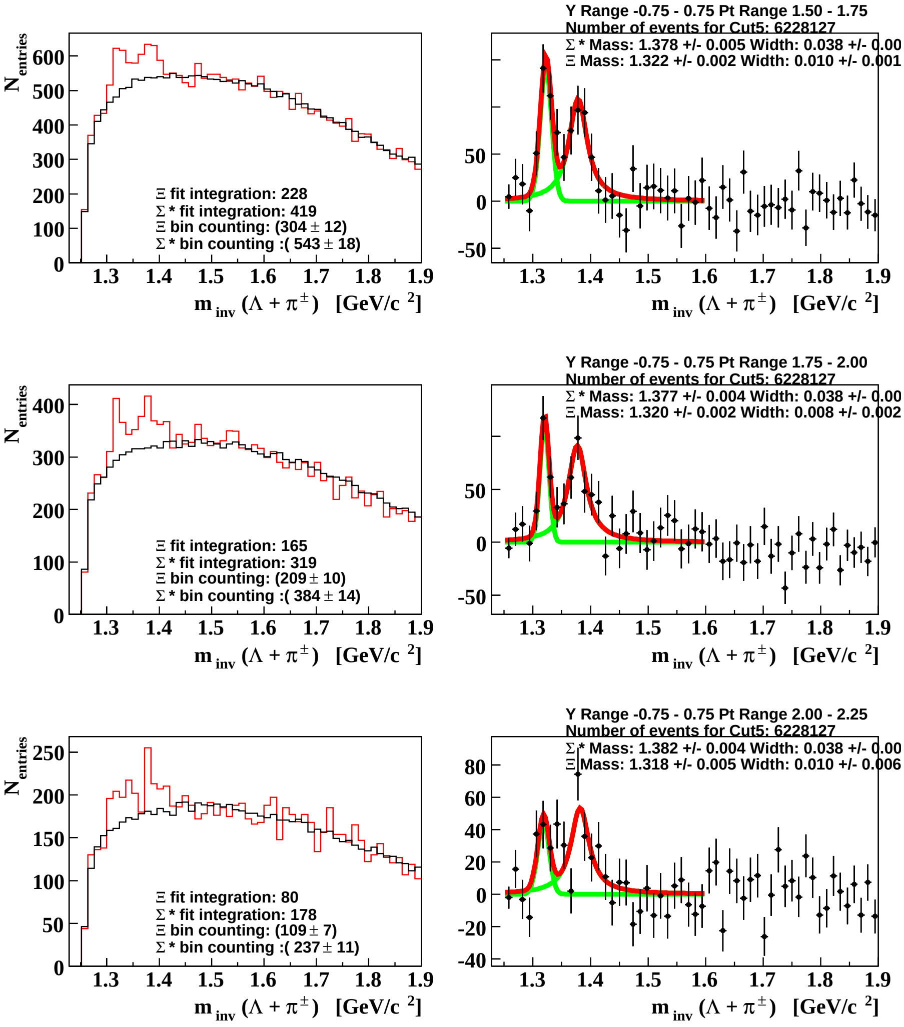

(a) (b)

Figure B.2: The individual invariant mass spectra for the specific p_T bins of $\Sigma^*(1385)$ (**a**) before the mixed event background subtraction and (**b**) after the mixed event background subtraction in minimum bias p+p collisions. A Gaussian for Ξ and Breit-Wigner for the $\Sigma^*(1385)$ are fit to the background subtracted spectra.

Figure B.8 and the p_T ranges are 0.5-1.25, 1.25-1.75, 1.75-2.25, 2.25-2.75 and 2.75-3.50 GeV/c starting from the top figure down to the bottom one.

Figure B.9 shows the first 3 p_T bins of the $\Sigma^*(1385)$ invariant mass spectra before and after mixed-event background subtraction for the minimum bias d+Au collisions. While the rapidity coverage of the $\Sigma^*(1385)$ is $|y| < 0.75$ for all plots in Figure B.9,

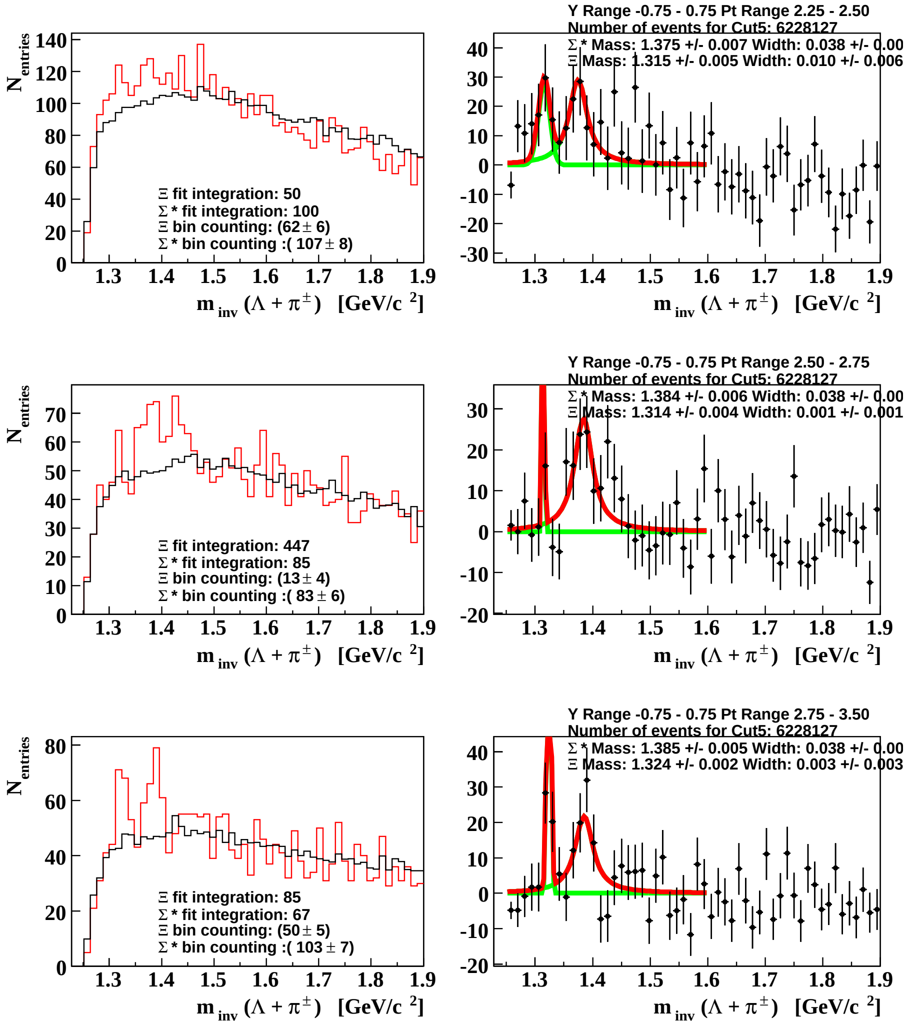

(a) (b)

Figure B.3: The individual invariant mass spectra for the specific p_T bins of $\Sigma^*(1385)$ (**a**) before the mixed event background subtraction and (**b**) after the mixed event background subtraction in minimum bias p+p collisions. A Gaussian for Ξ and Breit-Wigner for the $\Sigma^*(1385)$ are fit to the background subtracted spectra.

the p_T ranges are 0.25-1, 1-1.25, 1.25-1.5 GeV/c starting from the top figure down to the bottom one.

Figure B.10 shows the next 3 p_T bins of the $\Sigma^*(1385)$ invariant mass spectra before and after mixed-event background subtraction for the minimum bias d+Au collisions. The rapidity coverage of the $\Sigma^*(1385)$ is $|y| < 0.75$ for all plots in Figure B.10 and

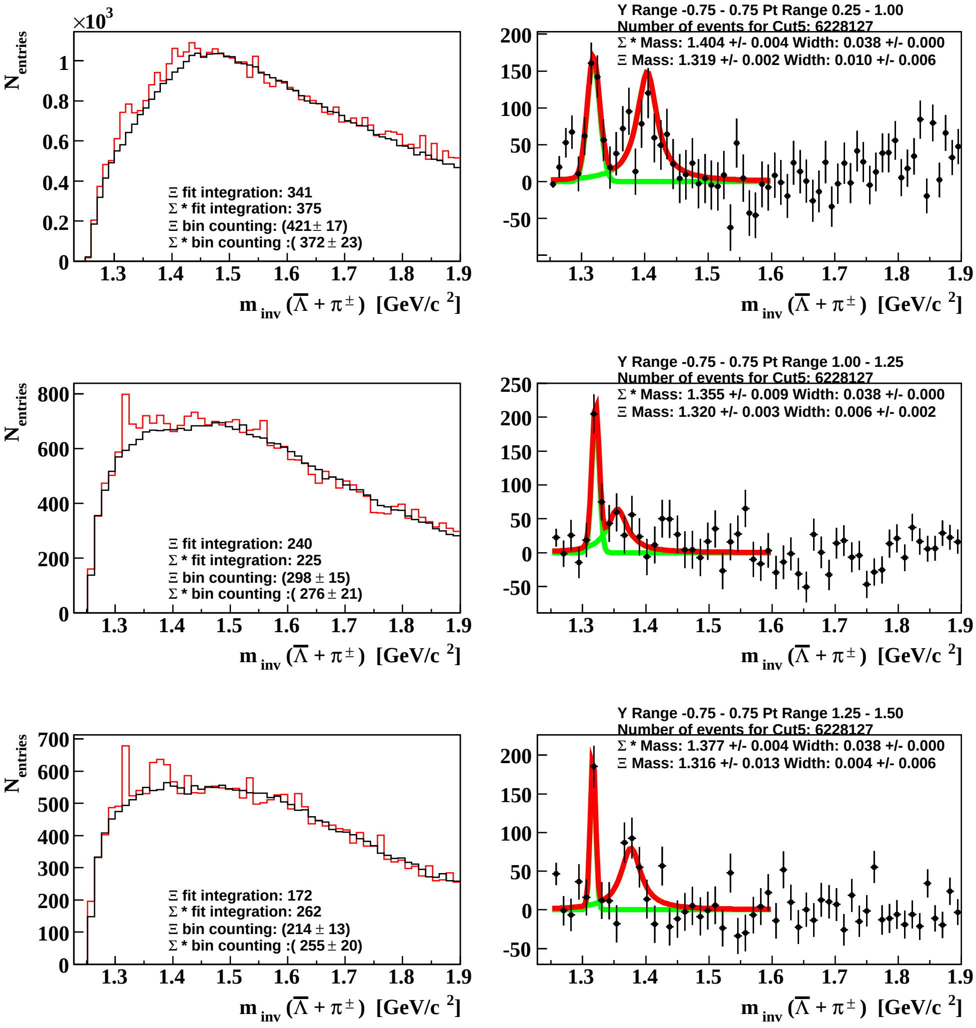

(**a**) (**b**)

Figure B.4: The individual invariant mass spectra for the specific p_T bins of $\overline{\Sigma^*}(1385)$ (**a**) before the mixed event background subtraction and (**b**) after the mixed event background subtraction in minimum bias p+p collisions. A Gaussian for $\bar{\Xi}$, and Breit-Wigner for the $\overline{\Sigma^*}(1385)$ are fit to the background subtracted spectra.

the p_T ranges are 1.5-1.75, 1.75-2, 2-2.25 GeV/c starting from the top figure down to the bottom one.

Figure B.11 shows the last 3 p_T bins of the $\Sigma^*(1385)$ invariant mass spectra before and after mixed-event background subtraction for the minimum bias d+Au collisions. The rapidity coverage of the $\Sigma^*(1385)$ is $|y| < 0.75$ for all plots in Figure B.11 and

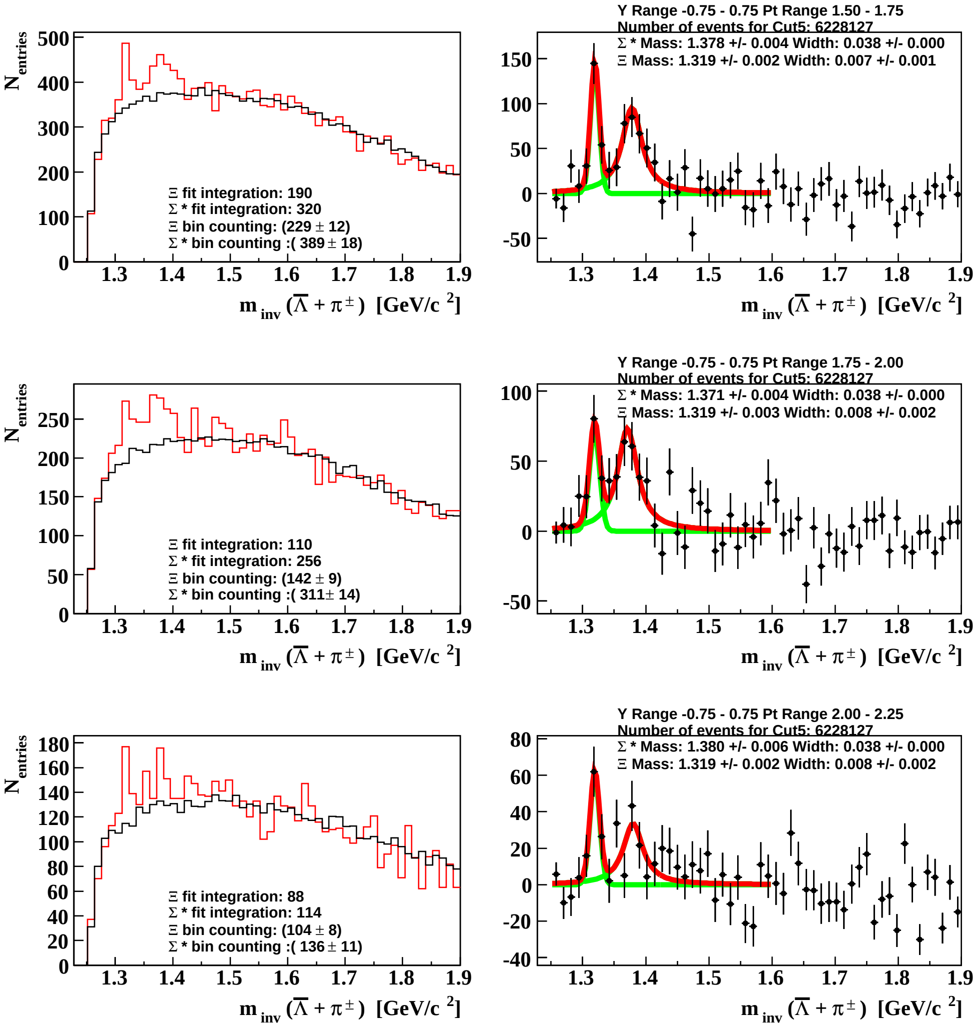

(a) (b)

Figure B.5: The individual invariant mass spectra for the specific p_T bins for $\overline{\Sigma^*}(1385)$ p_T (**a**) before the mixed event background subtraction and (**b**) after the mixed event background subtraction in minimum bias p+p collisions. A Gaussian for $\bar{\Xi}$, and Breit-Wigner for the $\overline{\Sigma^*}(1385)$ are fit to the background subtracted spectra.

the $\mathrm{p_T}$ ranges are 2.25-2.5, 2.5-2.75, 2.75-3.5 GeV/c starting from the top figure down to the bottom one.

The $\overline{\Sigma^*}(1385)$ invariant mass spectra for the same $\mathrm{p_T}$ cut ranges as the $\Sigma^*(1385)$ in the rapidity range $|y| < 0.75$ for the minimum bias d+Au collisions are presented

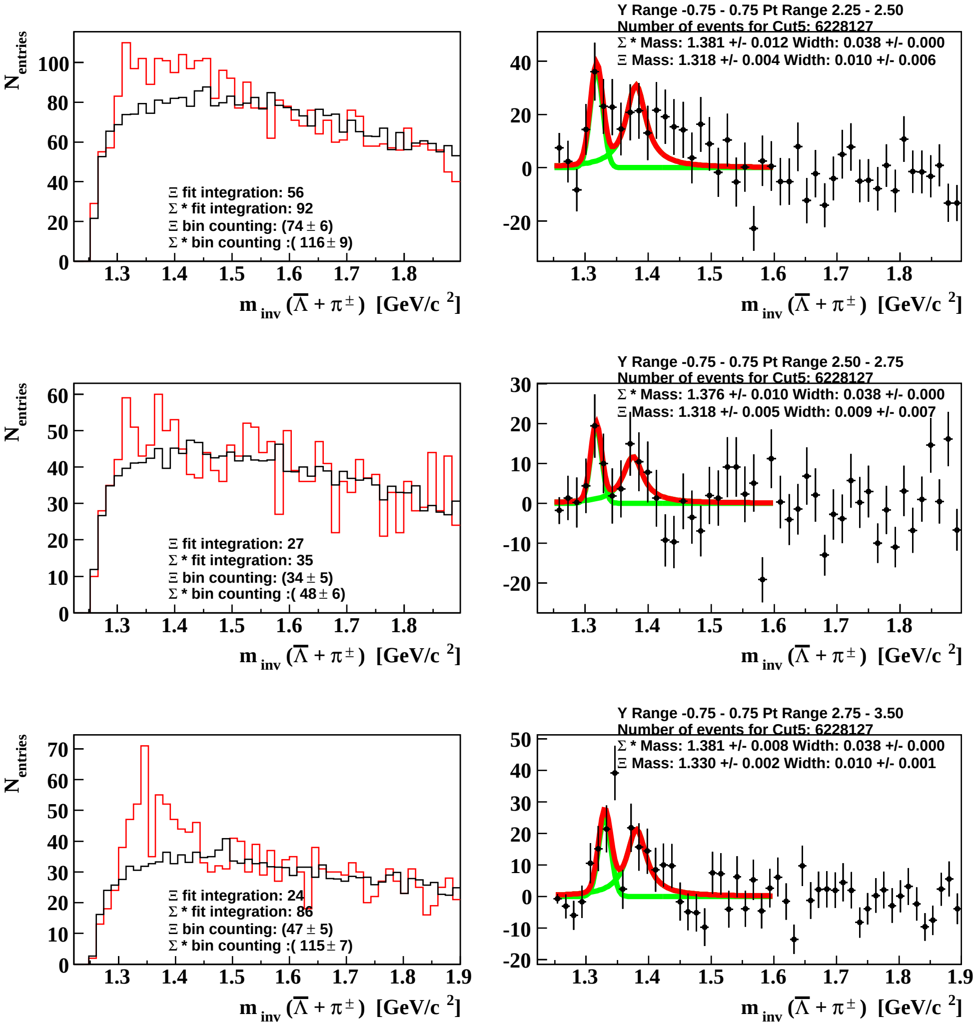

(a) (b)

Figure B.6: The individual invariant mass spectra for the specific p_T bins of $\overline{\Sigma^*}(1385)$ (**a**) before the mixed event background subtraction and (**b**) after the mixed event background subtraction in minimum bias p+p collisions. A Gaussian for $\bar{\Xi}$ and Breit-Wigner for the $\overline{\Sigma^*}(1385)$ are fit to the background subtracted invariant mass spectra.

in Figures B.12, B.13 and B.14.

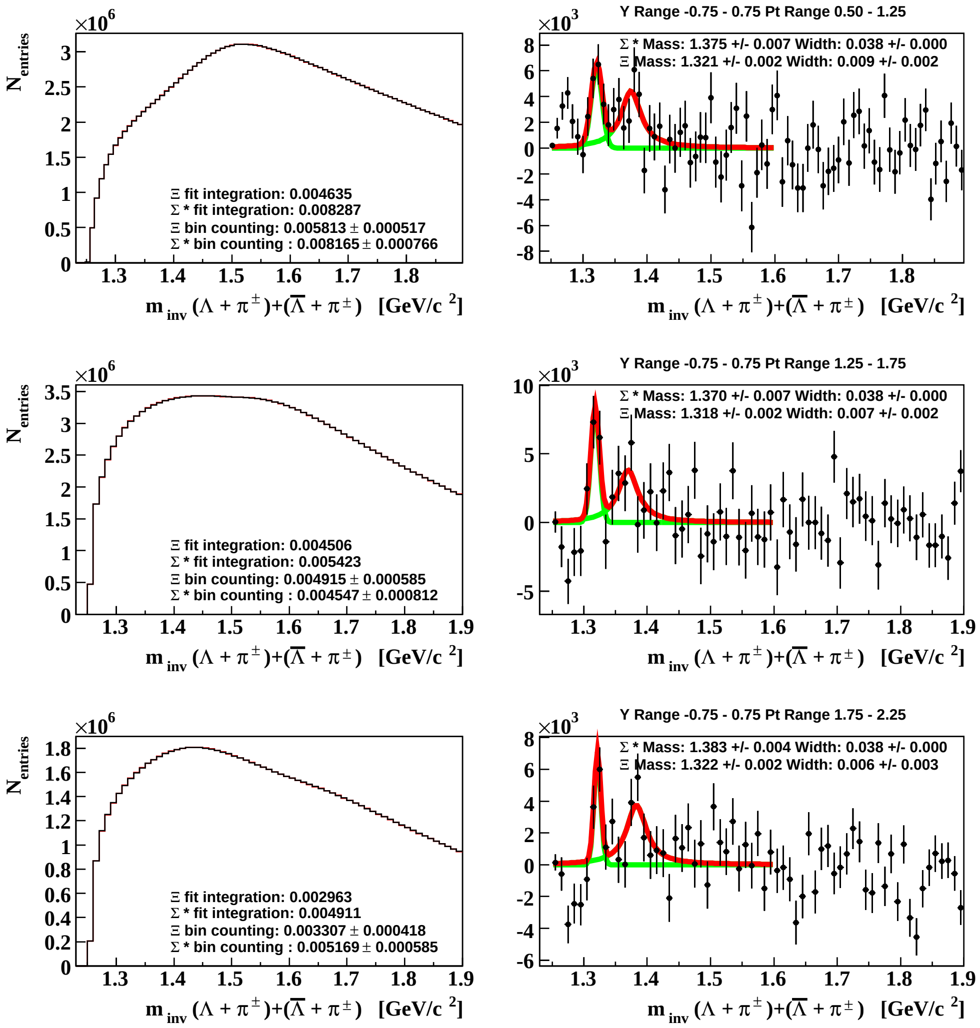

Figure B.7: Invariant Mass spectra for the $\Sigma^*(1385)$ for each p_T bin before and after mixed event background subtraction in the 0-5% most central Au+Au collisions. A Gaussian for Ξ and a Breit-Wigner for the $\Sigma^*(1385)$ are fit to the background subtracted spectra.

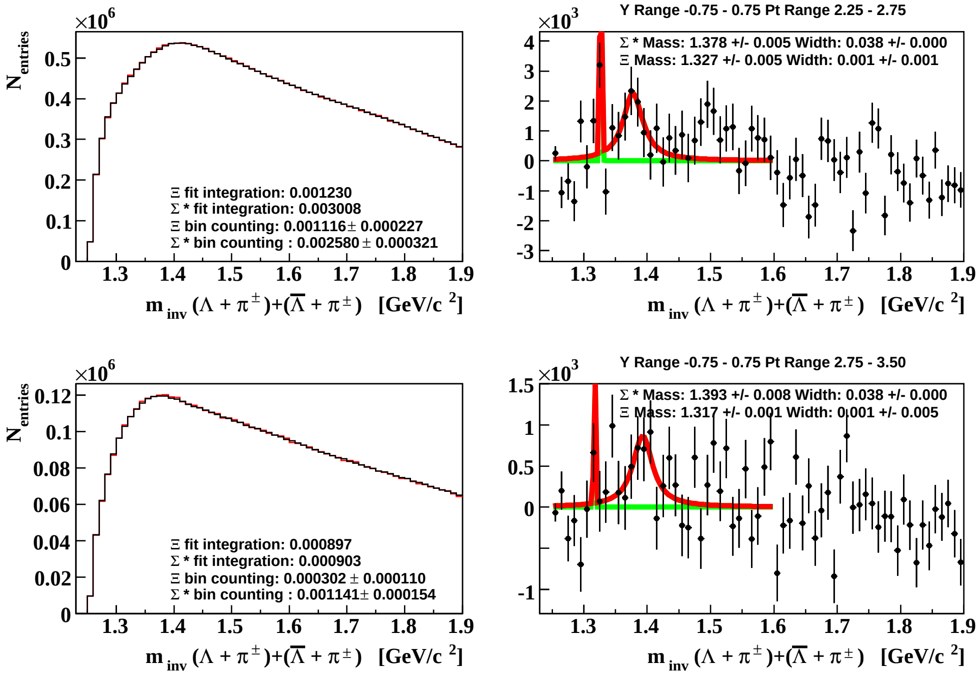

Figure B.8: Invariant Mass spectra for the $\Sigma^*(1385)$ for each p_T bin before and after mixed event background subtraction in the 0-5% most central Au+Au collisions. A Gaussian for Ξ and a Breit-Wigner for the $\Sigma^*(1385)$ are fit to the background subtracted spectra.

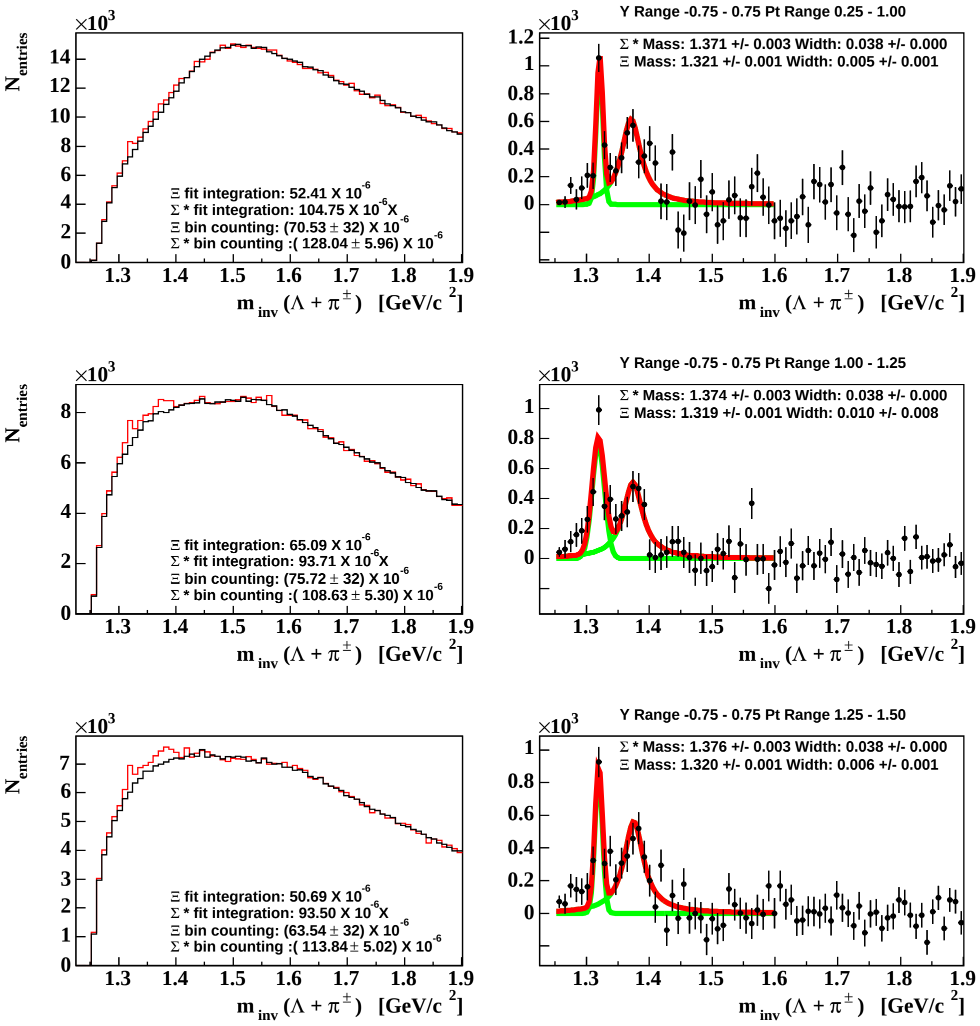

(a) **(b)**

Figure B.9: The individual invariant mass spectra for the specific p_T bins for the $\Sigma^*(1385)$ in minimum bias d+Au collisions at $\sqrt{s_{\rm NN}} = 200$ GeV (**a**) before the mixed event background subtraction and (**b**) after the mixed event background subtraction. A Gaussian for Ξ and a Breit-Wigner for the $\Sigma^*(1385)$ are fit to the background subtracted spectra. The raw yields for $\Sigma^*(1385)$ and Ξ from bin counting and integration from the fits are presented in the inset of each invariant mass plot.

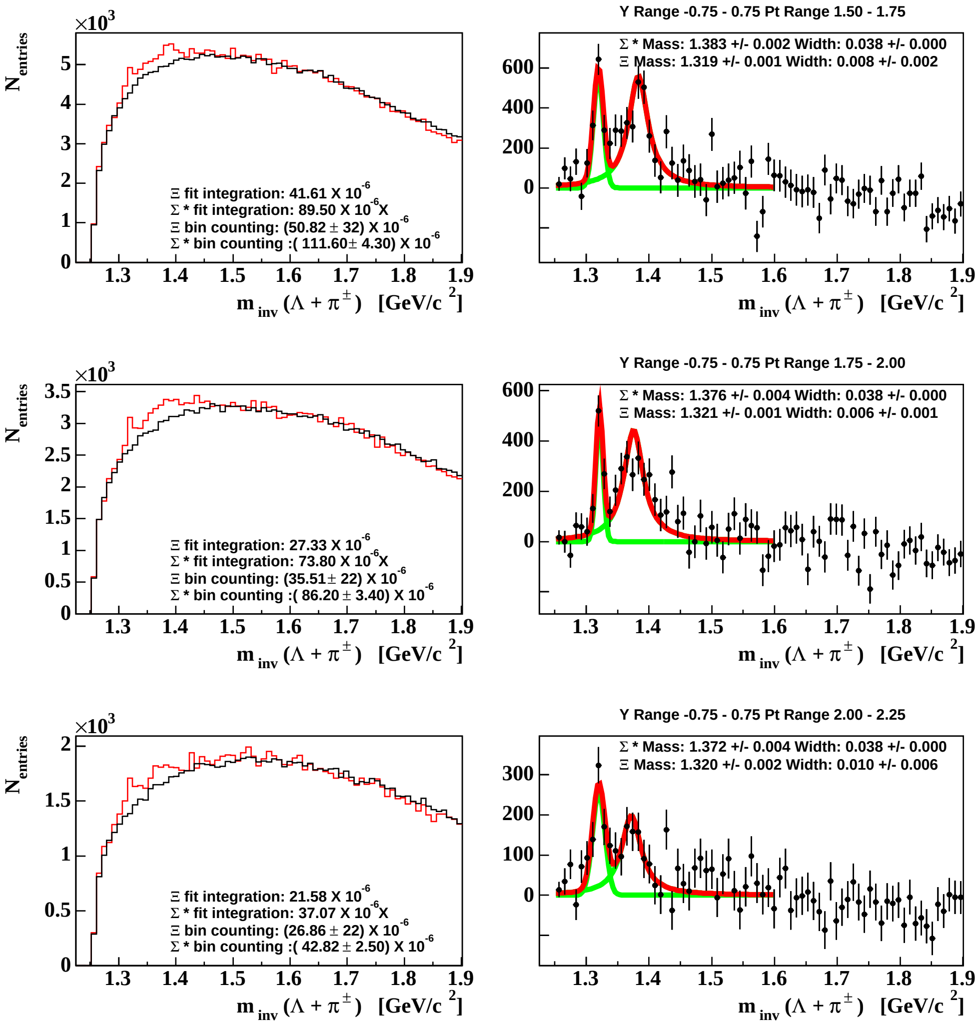

(a) (b)

Figure B.10: The individual invariant mass spectra for the specific p_T bins for the $\Sigma^*(1385)$ in minimum bias d+Au collisions at $\sqrt{s_{\mathrm{NN}}} = 200$ GeV (**a**) before the mixed event background subtraction and (**b**) after the mixed event background subtraction. A Gaussian for Ξ and a Breit-Wigner for the $\Sigma^*(1385)$ are fit to the background subtracted spectra. The raw yields for $\Sigma^*(1385)$ and Ξ from bin counting and integration from the fits are presented in the inset of each invariant mass plot.

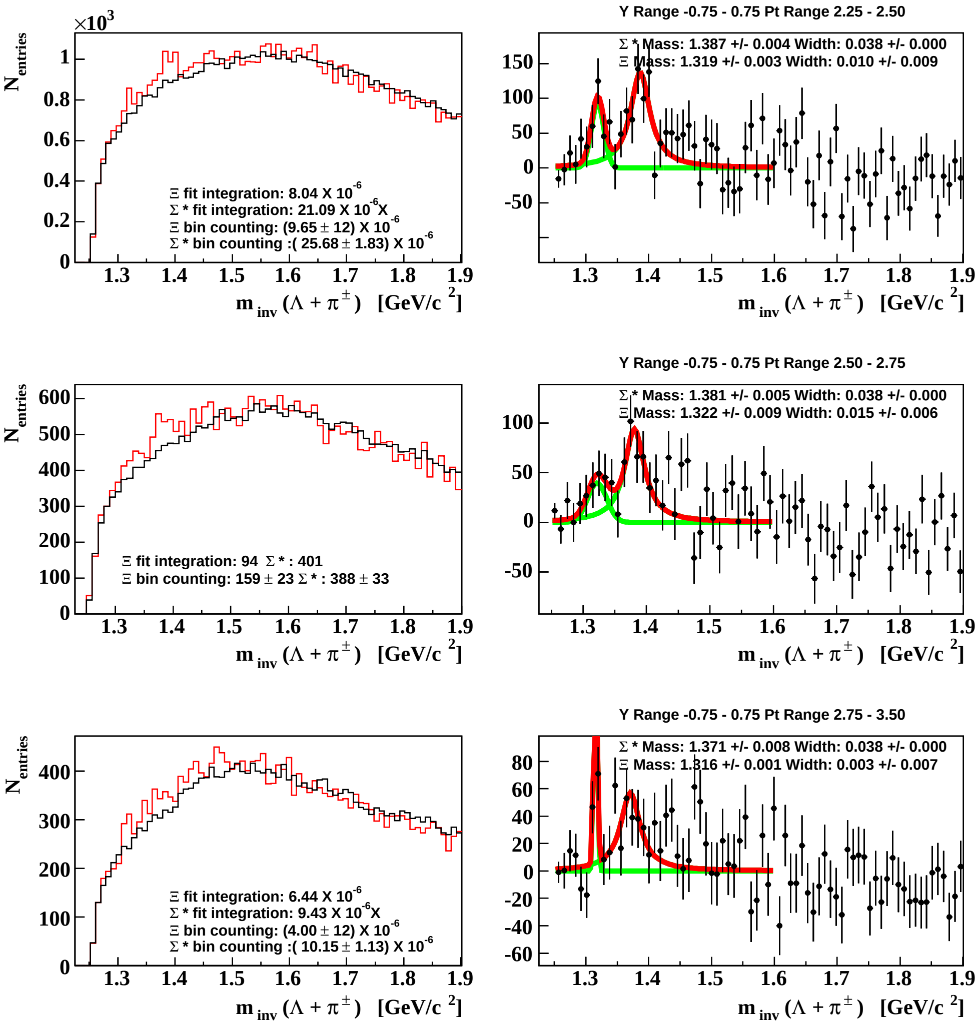

(a) (b)

Figure B.11: The individual invariant mass spectra for the specific p_T bins for the $\Sigma^*(1385)$ in minimum bias d+Au collisions at $\sqrt{s_{\rm NN}} = 200$ GeV (**a**) before the mixed event background subtraction and (**b**) after the mixed event background subtraction. A Gaussian for Ξ and a Breit-Wigner for the $\Sigma^*(1385)$ are fit to the background subtracted spectra. The raw yields for $\Sigma^*(1385)$ and Ξ from bin counting and integration from the fits are presented in the inset of each invariant mass plot.

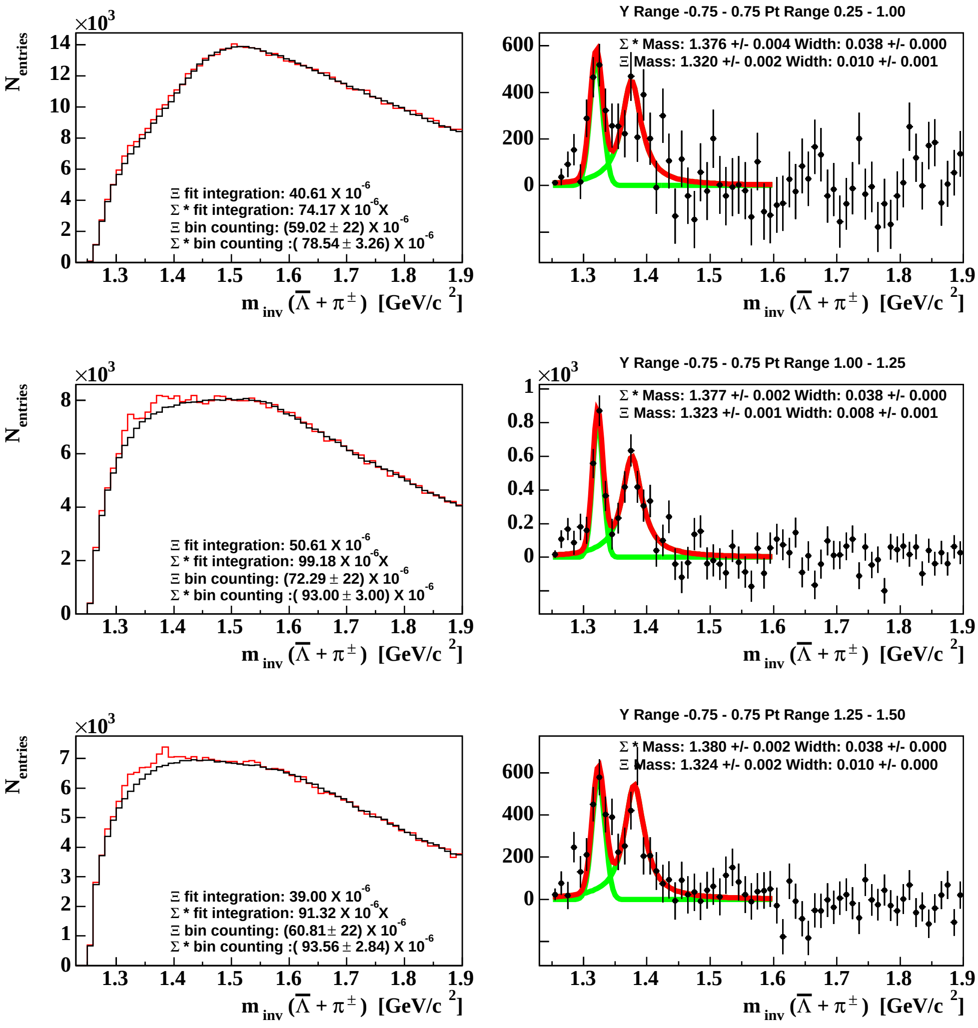

(a) (b)

Figure B.12: The individual invariant mass spectra for the specific p_T bins for the $\overline{\Sigma^*}(1385)$ in minimum bias d+Au collisions at $\sqrt{s_{\rm NN}} = 200$ GeV (**a**) before the mixed event background subtraction and (**b**) after the mixed event background subtraction. A Gaussian for $\bar{\Xi}$ and a Breit-Wigner for the $\overline{\Sigma^*}(1385)$ are fit to the background subtracted spectra. The raw yields for $\overline{\Sigma^*}(1385)$ and $\bar{\Xi}$ from bin counting and integration from the fits are presented in the inset of each invariant mass plot.

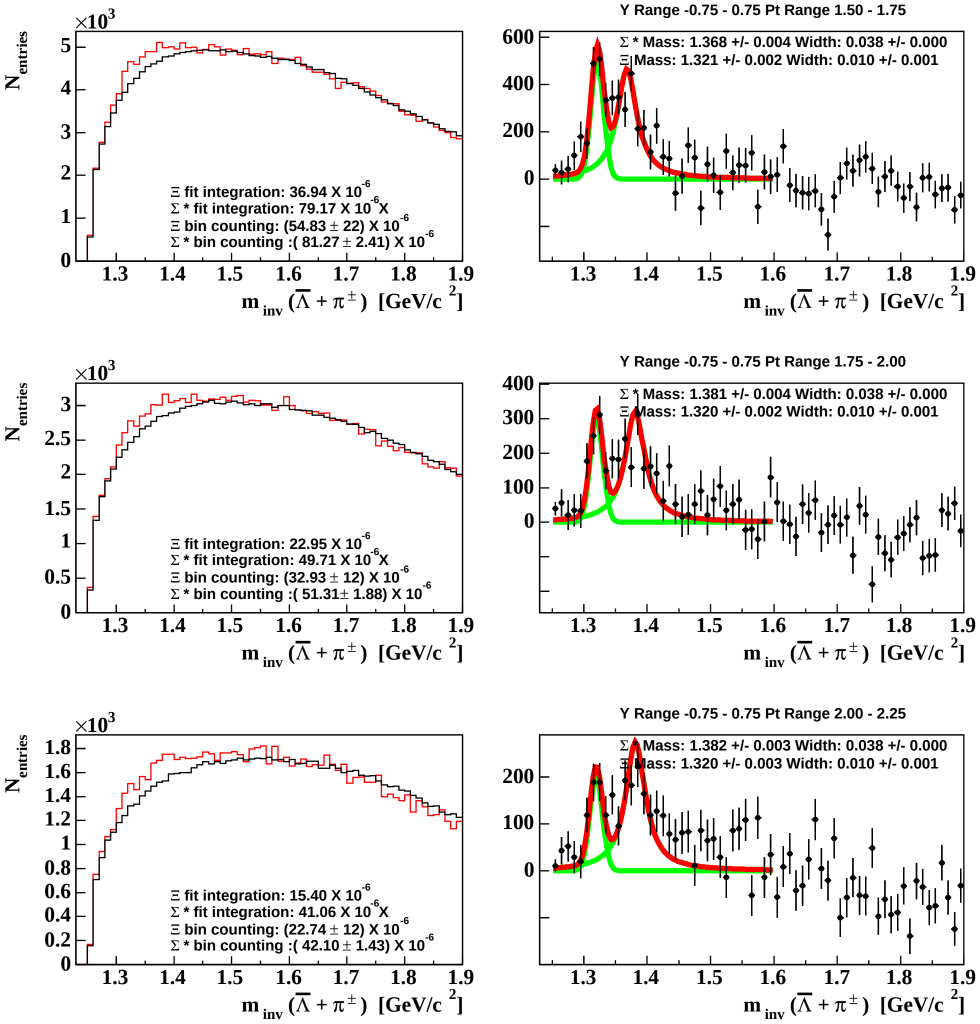

(a) **(b)**

Figure B.13: The invariant mass spectra for the individual p_T bins for the $\overline{\Sigma^*}(1385)$ in minimum bias d+Au collisions at $\sqrt{s_{\mathrm{NN}}} = 200$ GeV before the mixed event background subtraction and (**b**) after the mixed event background subtraction. A Gaussian for $\bar{\Xi}$ and a Breit-Wigner for the $\overline{\Sigma^*}(1385)$ are fit to the background subtracted spectra. The raw yields for $\overline{\Sigma^*}(1385)$ and $\bar{\Xi}$ from bin counting and integration from the fits are presented in the inset of each invariant mass plot.

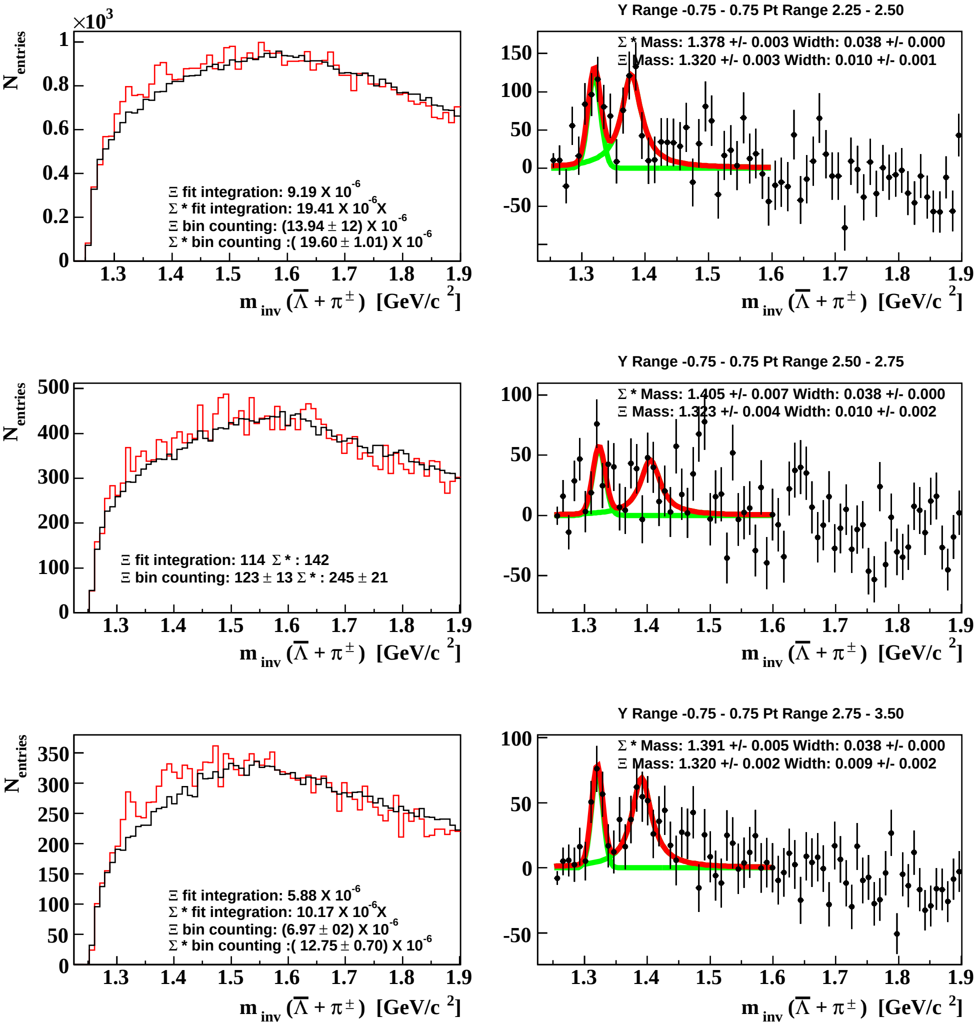

(a) (b)

Figure B.14: The invariant mass spectra for the individual p_T bins for the $\overline{\Sigma^*}(1385)$ in minimum bias d+Au collisions at $\sqrt{s_{\rm NN}} = 200$ GeV before the mixed event background subtraction and (**b**) after the mixed event background subtraction. A Gaussian for $\bar{\Xi}$ and a Breit-Wigner for the $\overline{\Sigma^*}(1385)$ are fit to the background subtracted spectra. The raw yields for $\overline{\Sigma^*}(1385)$ and $\bar{\Xi}$ from bin counting and integration from the fits are presented in the inset of each invariant mass plot.

Appendix C

Systematic Uncertainty

The systematic uncertainties are estimated by varying the applied cuts, the choice of background normalization range, and the bin widths in each invariant mass histogram. The estimation of the systematic uncertainties of masses, widths, raw counts of the invariant mass peaks, $\langle p_T \rangle$, T, and yields from the exponential fits are discussed.

C.1 Estimation of Systematic Uncertainty of the Mass and Width

The applied cuts that are presented in Table 4.3 and Table 4.2 for π and Λ are varied 12 times to determine the systematic uncertainties. The dE/dx selection of the $\pi_{Bacheleor}$ and its accepted momentum are varied to estimate the background contamination which cannot be corrected for using the simulation.

The raw invariant mass spectra for all $\mathrm{p_T}$ ranges after the background subtraction are fit with Gaussian and Breit-Wigner distributions for the Ξ and $\Sigma^*(1385)$ mass peaks, respectively. Figure C.1-a shows the variation of the mass parameters of the Gaussian distributions of Ξ. The mass parameters from Breit-Wigner distributions of $\Sigma^*(1385)$ are presented in Figure C.1-b. A second variation regarding the size of the bins in each invariant mass histogram is applied and the extracted mass parameters are included in these histograms. The mean and the RMS, which are included in the plots, are the estimated mass and the systematic uncertainty, respectively, for each particle.

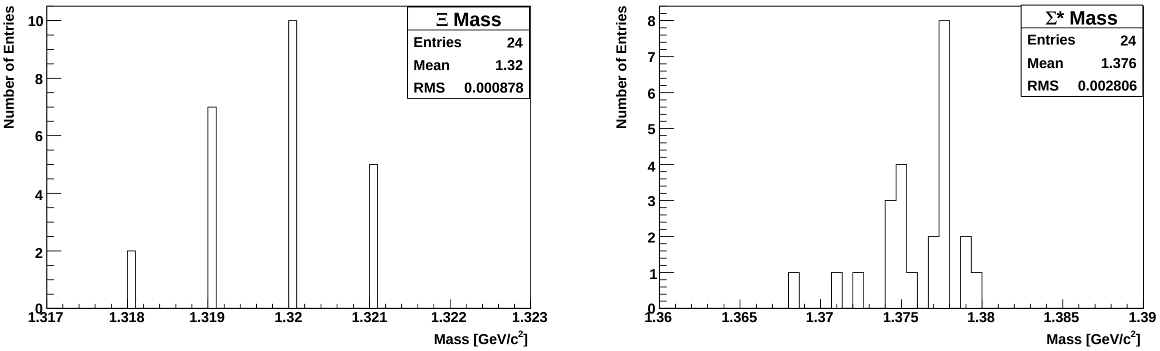

(a) **(b)**

Figure C.1: The number of counts versus the extracted mass from (**a**) the Gaussian distribution of Ξ and (**b**) the Breit-Wigner distribution of $\Sigma^*(1385)$.

For each cut set and two variations of bin width, the width of the Gaussian and Breit-Wigner distributions are shown in Figure C.2-a and Figure C.2-b for Ξ and $\Sigma^*(1385)$ particles, respectively.

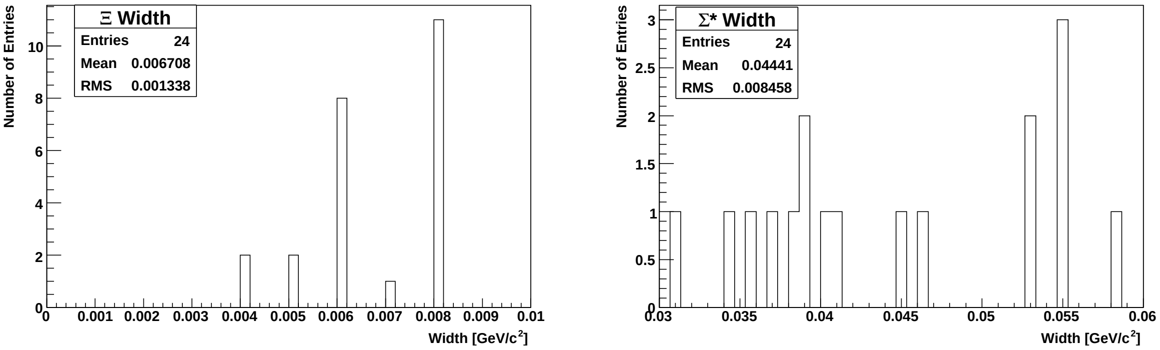

(a) **(b)**

Figure C.2: The number of counts versus the extracted width from (**a**) the Gaussian distribution of Ξ and (**b**) the Breit-Wigner distribution of $\Sigma^*(1385)$.

C.2 Estimation of Systematic Uncertainty of the Raw Ratios

A similar study with the variation of cuts is done for identification of the $\overline{\Sigma^*}(1385)$. However, this time only 4 different cut sets are used. The width, mass of the $\overline{\Sigma^*}(1385)$, and the percentage systematic uncertainty are the same as $\Sigma^*(1385)$ within errors. The antiparticle to particle raw ratios which are measured from the bin counts under the invariant mass peaks are studied with the variation of cuts and the bin widths. The number of entries corresponding to the number of cut variations versus the calculated ratio of antiparticles to particles for the Ξ and the $\Sigma^*(1385)$ are presented in Figure C.3-a and Figure C.3-b, respectively. The RMS and mean values of the ratios are presented in the insets of each plot.

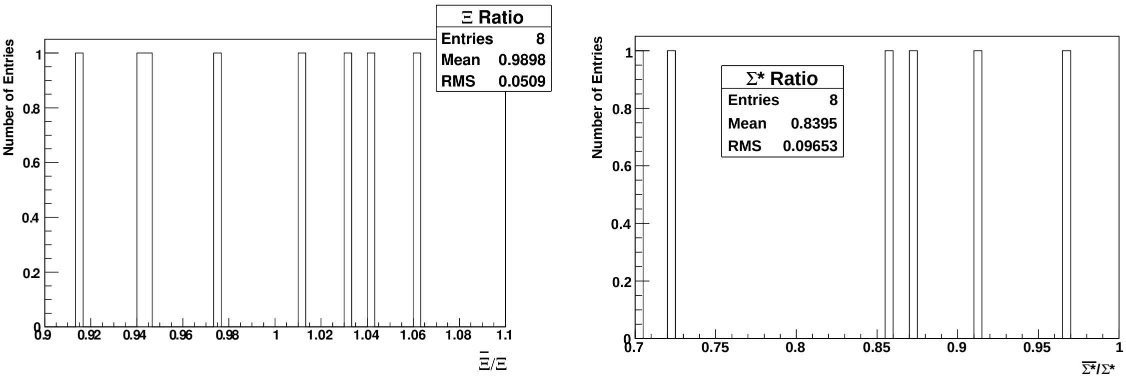

(a) **(b)**

Figure C.3: The number of entries versus the calculated ratio of antiparticles to particles for **(a)** Ξ and **(b)** $\Sigma^*(1385)$. The RMS and mean values of the ratios are presented in the insets of each plot.

C.3 Estimation of Systematic Uncertainty of Corrected Yields and $\langle p_T \rangle$

The $\overline{\Sigma^*}(1385)^{\pm}$ are corrected with the embedding of $\overline{\Sigma^*}(1385)^{+}$ and $\overline{\Sigma^*}(1385)^{-}$ separately. Due to the differences in the iteration to find the central point of the bin in exponential functions, the yields are extracted from $\mathrm{p_T}$ and $\mathrm{m_T} - m_0$ dependence separately and both are included in the plots. Figure C.4-a presents the number of entries vs. corrected yields of $\Sigma^*(1385)$ from the various cut sets.

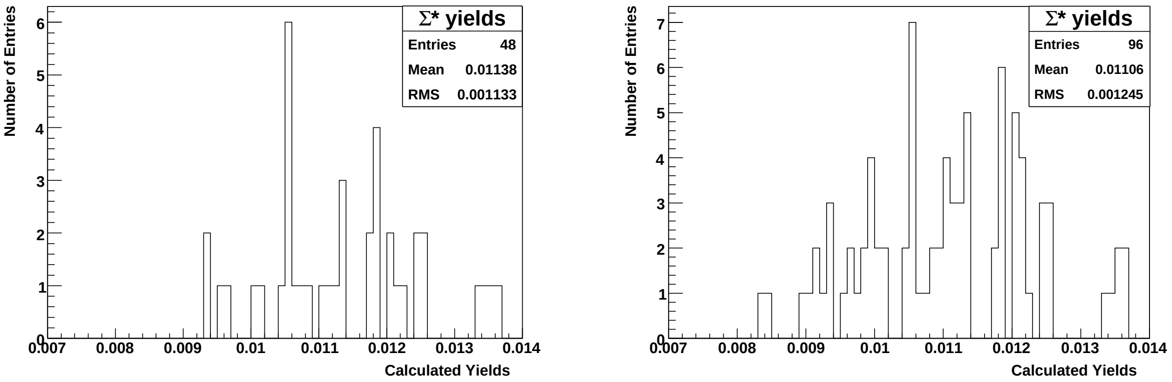

(a) (b)

Figure C.4: **(a)** The number of entries vs. corrected yields of the $\Sigma^*(1385)$ from variation of cut sets, correction factors and iteration of the central point of the corrected bins in exponential distributions. **(b)** The number of entries vs. corrected yields with the variation of the bin width included. The RMS and mean values are presented in the insets of each plot.

The bin width of each $\mathrm{p_T}$ dependent invariant mass spectrum is also varied. Figure C.4-b presents the histogram of the number of entries vs. corrected yields with the variation of the bin widths. For extraction of yields the background normalization range is also varied. Figure C.5-a is the histogram with the background normalization range variation instead of the bin widths and Figure C.5-b is for all variations. The RMS and mean values in Figure C.5 are for the estimated uncertainty of the yield and the yield of $\Sigma^*(1385)$ in minimum bias p+p collisions.

Similar to what is done for the corrected yields the systematic uncertainty for T is extracted from the variations of cuts, applied correction factors (i.e, the $\Sigma^*(1385)^-$ and $\Sigma^*(1385)^+$ embedding), the iterations of the center of each bin, the normalization range of the background subtraction, and the size of each bin of the invariant mass histograms. Figure C.6-a, Figure C.7-a and Figure C.8-a are for the number of entries versus the inverse slope parameter from exponential fits. The number of entries vs.

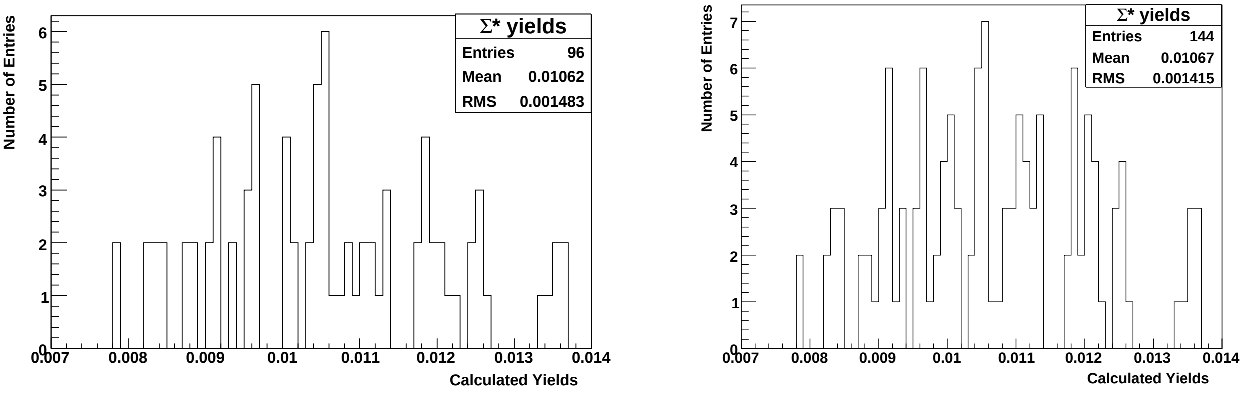

(a) (b)

Figure C.5: **(a)** The number of entries vs. corrected yields of $\Sigma^*(1385)$ from variation of cut sets, correction factors, iteration of the central points of the corrected bins in exponential distributions and the background normalization regions. **(b)** The number of entries vs. corrected yields with all variations; cuts, correction factors, iteration, bin width and the background normalization region. The RMS and mean values are presented in the insets of each plot.

$\langle p_T \rangle$ calculated from exponential fit functions of $\Sigma^*(1385)$ from various cut sets and correction factors are presented in Figure C.6-b, Figure C.7-b and Figure C.8-b.

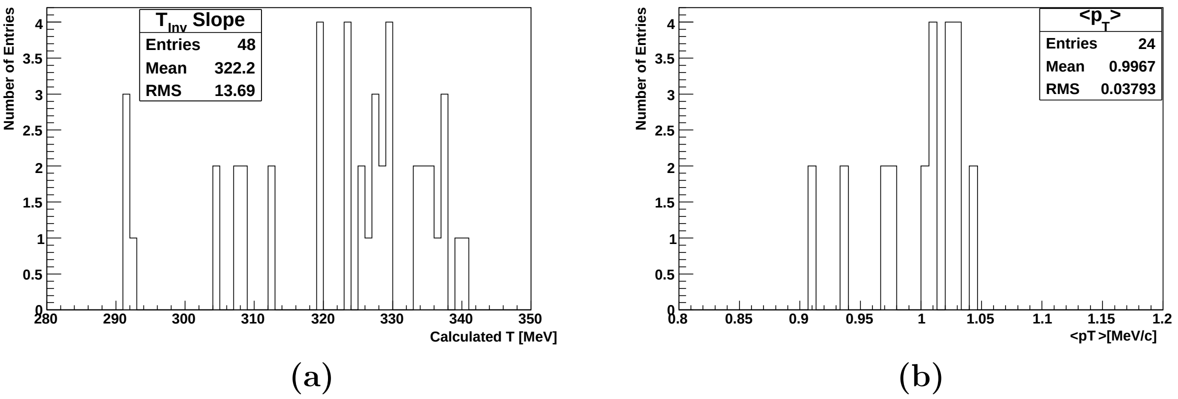

(a) (b)

Figure C.6: **(a)** The number of entries vs. (T), inverse slope parameter from exponential fits of $\Sigma^*(1385)$, from various cut sets and correction factors; **(b)** the number of entries vs $\langle p_T \rangle$ calculated from the fit functions for the cut and correction factor variations. The RMS and mean values are presented in the insets of the plots.

The Figure C.6 histograms are filled with the values that are extracted from the variations of cuts, applied correction factors (i.e, the $\Sigma^*(1385)^-$ and $\Sigma^*(1385)^+$ embedding) for $\langle p_T \rangle$ and also with the iterations of the center of each bin for T.

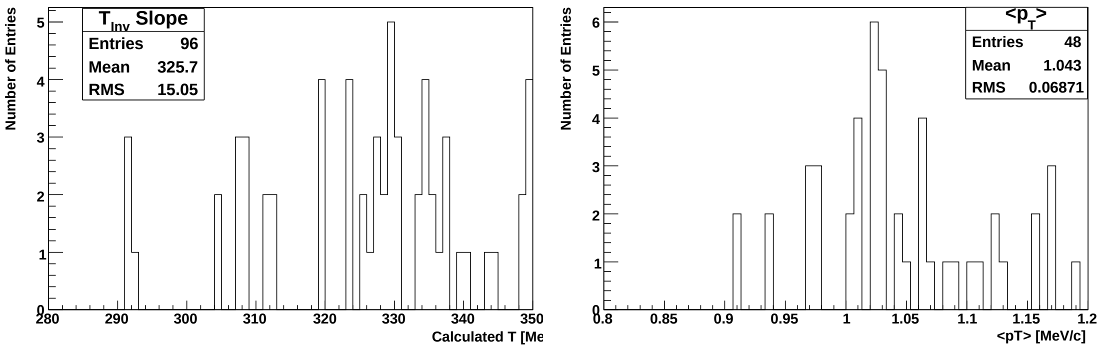

(a) **(b)**

Figure C.7: **(a)** The number of entries vs. (T), inverse slope parameter from exponential fits of $\Sigma^*(1385)$, from various cut sets and correction factors; **(b)** the number of entries vs $\langle p_T \rangle$ calculated from the fit functions for the cut and correction factor variations. The RMS and mean values are presented in the insets of the plots.

The Figure C.7 histograms are filled with the values that are extracted from the variations of cuts described for Figure C.6 and also the variations of the normalization for the background range.

The Figure C.8 histograms are filled with the values that are extracted from the variations of cuts described for Figure C.7 and also from variations of bin widths of the invariant mass histograms. The RMS and mean values, that are presented in the insets of the Figure C.8-a and Figure C.8-b, are for the T and $\langle p_T \rangle$ and their systematic uncertainties.

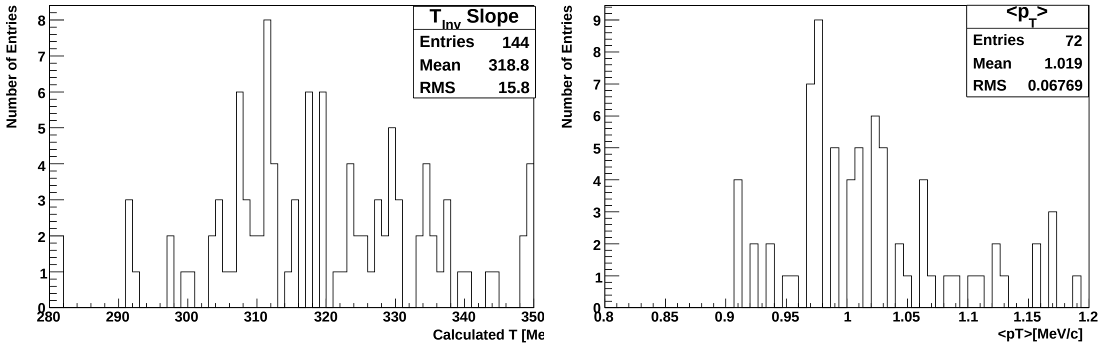

(a) **(b)**

Figure C.8: **(a)** The number of entries vs. (T), inverse slope parameter from exponential fits of $\Sigma^*(1385)$, from various cut sets and correction factors; **(b)** the number of entries vs $\langle p_T \rangle$ calculated from the fit functions for the cut and correction factor variations. The RMS and mean values are presented in the insets of the plots.

Appendix D

Acronyms

AGS Alternating Gradient Synchrotron.

BRAHMS Broad Range Hadron Magnetic Spectrometers Experiment at RHIC. It is designed to measure hadronic particles inclusively over a wide range of pseudorapidity and $\mathrm{p_T}$ ($0 < \eta < 4$, $\mathrm{p_T} < 30$ GeV).

BBC Beam Beam Counter. The BBCs are scintillating tiles used to trigger on charged particle multiplicity in the forward rapidity region.

BEMC Barrel Electromagnetic Calorimeter. The BEMC provides electromagnetic calorimetry in the mid-rapidity region.

BNL Brookhaven National Laboratory.

CERN Centre Européen pour la Recherche Nucleaire. European Organization for Nuclear Research.

CM Central Membrane. The high voltage membrane which separates the TPC into two tracking volumes. It is located at $Z = 0$ of the TPC and is perpendicular to the beam line. It is operated at 28 kV.

CTB Central Trigger Barrel. The CTB is made of scintillating tiles and is used to trigger on charged particle multiplicity.

DAQ Data Acquisition System.

DCA Distance of Closest Approach.

EEMC Endcap Electromagnetic Calorimeter. The EEMC provides electromagnetic calorimetry in the forward-rapidity region.

FEE Front End Electronics.

FPD Forward Pion Detector. The FPD is a prototype for the endcap electromagnetic calorimeter.

FTPC Forward Time Projection Chamber. The FTPC provides charged particle tracking in the forward and backward rapidity region.

GEANT GEometry ANd Tracking. GEANT is a world standard used primarily to simulate the passage of particles through matter. GEANT is used both within and beyond particle physics, including many applications in medical physics.

HCT Hybrid Combinatorial Technique. For $\Sigma^*(1385)$ identification first the Λ is topologically identified, then all possible π are combined with the Λ to produce an invariant mass spectra for $\Sigma^*(1385)$. Similar to TPM, a mixed event-technique is used to estimate the uncorrelated background. Λ from one event is combined with π from the other similar event.

IFC Inner Field Cage. The IFC of the STAR TPC.

MC Monte Carlo.

MWPC Multi Wire Proportional Counter. The MWPC is part of the TPC readout system.

PHENIX Pioneering High Energy Nuclear Experiment. The detectors of PHENIX are designed to observe photon and dilepton pairs to identify vector mesons and investigate their properties.

PHOBOS Modular Array for RHIC Spectra (MARS) The original experiment MARS was not approved, the slightly revised experiment PHOBOS (one of the moons of MARS) was approved. The silicon based detector setup of PHOBOS is designed with the aim to study particles to investigate the global event structure within the full pseudorapidity range ($-5.4 < \eta < 5.4$).

PMT Photo Multiplier Tube.

pQCD Perturbative Quantum Chromo Dynamics. pQCD is a perturbative field theory solution to QCD.

QCD Quantum Chromo-Dynamics. QCD is the theory of strongly interacting particles.

QGP Quark Gluon Plasma. The minimal definition of a QGP is a deconfined medium where color charges flow freely.

Ref Mult Reference multiplicity defines the number of charged tracks. To be counted in the reference multiplicity a track must pass the following cuts; $|\eta| \leq 0.5$, number of Fit Points ≥ 10, and distance of closest approach to the primary vertex < 3 cm.

RHI Relativistic Heavy Ion.

RHIC Relativistic Heavy Ion Collider.

SSD Silicon Strip Detector. The fourth layer of SVT, to increase the tracking precision for the primary and secondary verticies.

significance The significance of a signal is given as $\widetilde{S} = \frac{S}{\sqrt{S+(1+n)B}}$ where S is the counts in the signal and B the counts in the background. The n represents the normalization factor for the mixed event background.

STAR Solenoidal Tracker At RHIC.

SVT Silicon Vertex Tracker. The SVT provides high precision tracking information close to the interaction point.

TOF Time of Flight detector. TOF primarily used to identify charged particles in the intermediate momentum region. In STAR, the system provides velocity information for reconstructed tracks that extends the hadronic particle identification capabilities of STAR.

TPC Time Projection Chamber. The TPC is STAR's main tracking detector.

TPM Three Particle Combinatorial Method. All possible decay daughters of $\Sigma^*(1385)$ are combined to calculate the invariant mass distribution of $\Sigma^*(1385)$. A mixed event-technique, where no correlations are possible, is used to estimate the background.

ZDC Zero Degree Calorimeter. A ZDC primarily detects neutrons that are remnants of the beam break-up.

Bibliography

[1] J. W. Harris and B. Muller, *The search for the quark-gluon plasma*, Ann. Rev. Nucl. Part. Sci. **46**, 71 (1996), hep-ph/9602235.

[2] P. Braun-Munzinger, *Chemical equilibration and the hadron-QGP phase transition*, Nucl. Phys. **A681**, 119 (2001), nucl-ex/0007021.

[3] K. Rajagopal and F. Wilczek, *The condensed matter physics of QCD*, (2000), hep-ph/0011333.

[4] F. Karsch, *Lattice results on QCD thermodynamics*, Nucl. Phys. **A698**, 199 (2002), hep-ph/0103314.

[5] H. L. Anderson, E. Fermi, E. A. Long, and D. E. Nagle, *Total Cross-Sections of Positive Pions in Hydrogen*, Phys. Rev. **85**, 936 (1952).

[6] M. Alston *et al.*, *Resonance in the* Λ *and* π *system*, Phys. Rev. Lett. **5**, 520 (1960).

[7] G. Torrieri and J. Rafelski, *Strange hadron resonances as a signature of freeze-out dynamics*, Phys. Lett. **B509**, 239 (2001), hep-ph/0103149.

[8] M. Bleicher and J. Aichelin, *Strange resonance production: Probing chemical and thermal freeze-out in relativistic heavy ion collisions*, Phys. Lett. **B530**, 81 (2002), hep-ph/0201123.

[9] J. Adams *et al.* (STAR Collaboration), ρ^0 *production and possible modification in Au+Au and p+p collisions at* $\sqrt{s_{\rm NN}} = 200$ *GeV*, Phys. Rev. Lett. **92**, 092301 (2004), nucl-ex/0307023.

[10] H. Zhang, $K^*(892)$ *Resonance Production in Au+Au and p+p Collisions at* $\sqrt{s_{\rm NN}} = 200$ *GeV at the Relativistic Heavy Ion Collider*, PhD thesis, Yale University, May 2004.

[11] J. Adams *et al.* (STAR Collaboration), *K*(892) resonance production in Au+Au and p+p collisions at* $\sqrt{s_{\rm NN}} = 200$ *GeV at STAR*, Phys. Rev. **C71**, 064902 (2005), nucl-ex/0412019.

[12] P. Fachini, *Resonance production*, J. Phys. **G30**, S735 (2004), nucl-ex/0403026.

[13] J. Adams *et al.* (STAR Collaboration), *Phi meson production in Au+Au and p+p collisions at* $\sqrt{s_{\rm NN}} = 200$ *GeV*, Phys. Lett. **B612**, 181 (2005), nucl-ex/0406003.

[14] A. Tai, *Private Communications.*

[15] L. Gaudichet, *Production de* $\Lambda(1520)$ *dans les collisions p+p et Au+Au à* $\sqrt{s_{\rm NN}} = 200$ *GeV dans l'expérience STAR au RHIC*, PhD thesis, Univesit é De Nantes, Oct 2003.

[16] C. Markert (STAR Collaboration), *Strange resonance production in p+p and Au+Au collisions at RHIC energies*, J. Phys. **G30**, S1313 (2004), nucl-ex/0404003.

[17] R. Witt (STAR Collaboration), *Measurements of multistrange baryon resonances in STAR at RHIC*, J. Phys. **G31**, S163 (2005).

[18] J. Rafelski and B. Muller, *Strangeness production in the quark gluon plasma*, Phys. Rev. Lett. **48**, 1066 (1982).

[19] A. Wroblewski, *On the strange quark suppression factor in high-energy collisions*, Acta Phys. Polon. **B16**, 379 (1985).

[20] G. Bocquet *et al.*, *A Study of particle ratios and strangeness suppression in p anti-p collisions at* $\sqrt{s} = 630$ *GeV with UA1*, Phys. Lett. **B366**, 447 (1996).

[21] C. Adler *et al.* (STAR Collaboration), *Kaon production and kaon to pion ratio in Au+Au collisions at* $\sqrt{\mathrm{s_{NN}}} = 130$ *GeV*, Phys. Lett. **B595**, 143 (2004), nucl-ex/0206008.

[22] J. L. Bailly *et al.* (EHS-RCBC Collaboration), *Strangeness and diquark suppression factors in 360-GeV/c p+p interactions*, Phys. Lett. **B195**, 609 (1987).

[23] L. Ahle *et al.* (E-802 Collaboration), *Centrality dependence of kaon yields in* Si + A *and Au+Au collisions at the AGS*, Phys. Rev. **C60**, 044904 (1999), nucl-ex/9903009.

[24] C. Hohne (NA49 Collaboration), *Strangeness production in nuclear collisions: Recent results from experiment NA49*, Nucl. Phys. **A661**, 485 (1999).

[25] S. Salur (STAR Collaboration), *System and energy dependence of strangeness production with STAR*, (2005), nucl-ex/0509036.

[26] M. Gyulassy and M. Plumer, *Jet quenching as a probe of dense matter*, Nucl. Phys. **A527**, 641 (1991).

[27] R. J. Glauber, *Cross-sections in deuterium at high-energies*, Phys. Rev. **100**, 242 (1955).

[28] K. Redlich and A. Tounsi, *Strangeness enhancement and energy dependence in heavy ion collisions*, Eur. Phys. J. **C24**, 589 (2002), hep-ph/0111261.

[29] R. Hagedorn, *Multiplicities,* $\mathrm{p_T}$ *distributions and the expected hadron to quark gluon phase transition*, Riv. Nuovo Cim. **6N10**, 1 (1984).

[30] P. Braun-Munzinger, K. Redlich, and J. Stachel, *Particle production in heavy ion collisions*, (2003), nucl-th/0304013.

[31] J. Rafelski, *Strange anti-baryons from quark gluon plasma*, Phys. Lett. **B262**, 333 (1991).

[32] G. Torrieri, *Statistical hadronization phenomenology in heavy ion collisions at SPS and RHIC energies*, (2004), nucl-th/0405026.

[33] J. Rafelski and J. Letessier, *Testing limits of statistical hadronization*, Nucl. Phys. **A715**, 98 (2003), nucl-th/0209084.

[34] J. Adams *et al.* (STAR Collaboration), *Experimental and theoretical challenges in the search for the quark gluon plasma: The STAR collaboration's critical assessment of the evidence from RHIC collisions*, Nucl. Phys. **A757**, 102 (2005), nucl-ex/0501009.

[35] F. Bergsma *et al.*, *The STAR detector magnet subsystem*, Nuclear Instruments and Methods in Physics Research **A 499**, 633 (2003).

[36] M. Anderson *et al.*, *The STAR time projection chamber: a unique tool for studying high multiplicity events at RHIC*, Nuclear Instruments and Methods in Physics Research **A 499**, 659 (2003).

[37] M. Anderson *et al.*, *A readout system for the STAR time projection chamber*, Nuclear Instruments and Methods in Physics Research **A 499**, 679 (2003).

[38] C. Adler *et al.*, *The RHIC zero-degree calorimeters*, Nuclear Instruments and Methods in Physics Research **A 499**, 433 (2003).

[39] S. Eidelman *et al.* (Particle Data Group Collaboration), *Review of particle physics*, Phys. Lett. **B592**, 1 (2004).

[40] J. D. Jackson, *Remarks on the phenomenological analysis of resonances*, Nuovo Cim. **34**, 1644 (1964).

[41] LBL NEWS Magazine **6**, 94 (1981).

[42] J. Gans, *Inclusive Charged Hadron* $\mathrm{p_T}$ *Spectra at* $\sqrt{s_{\mathrm{NN}}} = 200$ *GeVfor p+p and d+Au Collisions at the Relativistic Heavy Ion Collider*, PhD thesis, Yale University, December 2004.

[43] O. Barrannikova, *Vertex Reconstruction Efficiency*, (2003).

[44] J. Adams *et al.* (STAR Collaboration), *Strange Particle Production in p+p Collisions at* $\sqrt{s_{\mathrm{NN}}} = 200$ *GeV.*, (in preperation).

[45] J. Adams *et al.*, *Scaling Properties of Hyperon Production in Au+Au Collisions at* $\sqrt{s_{\mathrm{NN}}} = 200$ *GeV*.

[46] R. Witt, *Private Communications.*

[47] J. W. Cronin *et al.*, *Production of hadrons with large transverse momentum at 200 GeV and 300 GeV*, Phys. Rev. Lett. **31**, 1426 (1973).

[48] J. W. Cronin *et al.*, *Production of hadrons with large transverse momentum at 200 GeV, 300 GeV, and 400 GeV*, Phys. Rev. **D11**, 3105 (1975).

[49] R. L. Jaffe, *Multi-Quark Hadrons. 2. Methods*, Phys. Rev. **D15**, 281 (1977).

[50] R. L. Jaffe and F. Wilczek, *Diquarks and exotic spectroscopy*, Phys. Rev. Lett. **91**, 232003 (2003), hep-ph/0307341.

[51] D. Diakonov, V. Petrov, and M. V. Polyakov, *Exotic anti-decuplet of baryons: Prediction from chiral solitons*, Z. Phys. **A359**, 305 (1997), hep-ph/9703373.

[52] T. Nakano *et al.* (LEPS Collaboration), *Observation of* $S = +1$ *baryon resonance in photo-production from neutron*, Phys. Rev. Lett. **91**, 012002 (2003), hep-ex/0301020.

[53] S. Stepanyan *et al.* (CLAS Collaboration), *Observation of an exotic* $S = +1$ *baryon in exclusive photoproduction from the deuteron*, Phys. Rev. Lett. **91**, 252001 (2003), hep-ex/0307018.

[54] V. V. Barmin *et al.* (DIANA Collaboration), *Observation of a baryon resonance with positive strangeness in* K^+ *collisions with Xe nuclei*, Phys. Atom. Nucl. **66**, 1715 (2003), hep-ex/0304040.

[55] J. Barth *et al.* (SAPHIR Collaboration), *Observation of the positive-strangeness pentaquark* Θ^+ *in photoproduction with the SAPHIR detector at ELSA*, Phys. Lett. **B572**, 127 (2003), hep-ex/0307083.

[56] M. Battaglieri *et al.* (the CLAS Collaboration), *Search for* Θ^+ *pentaquark in high statistics measurement of* $\gamma+p \rightarrow \bar{K}^0+K^++n$ *at CLAS*, (2005), hep-ex/0510061.

[57] C. Alt *et al.* (NA49 Collaboration), *Observation of an exotic S = -2, Q = -2 baryon resonance in proton proton collisions at the CERN SPS*, Phys. Rev. Lett. **92**, 042003 (2004), hep-ex/0310014.

[58] T. Berger-Hryn'ova (BABAR Collaboration), *Searches for pentaquark baryons at BaBar*, (2005), hep-ex/0510044.

[59] L. W. Chen, V. Greco, C. M. Ko, S. H. Lee, and W. Liu, *Pentaquark baryon production at the Relativistic Heavy Ion Collider*, Phys. Lett. **B601**, 34 (2004), nucl-th/0308006.

[60] W. Liu and C. M. Ko, *Cross sections for pentaquark baryon production from protons in reactions induced by hadrons and photons*, Phys. Rev. **C68**, 045203 (2003), nucl-th/0308034.

[61] J. Letessier, G. Torrieri, S. Steinke, and J. Rafelski, *Strange pentaquark hadrons in statistical hadronization*, Phys. Rev. **C68**, 061901 (2003), hep-ph/0310188.

[62] J. Randrup, *Production of the exotic Theta baryon in relativistic nuclear collisions*, Phys. Rev. **C68**, 031903 (2003), nucl-th/0307042.

[63] K. Hicks, *Experimental outlook for the pentaquark*, Int. J. Mod. Phys. **A20**, 219 (2005), hep-ph/0408001.

[64] V. Kubarovsky *et al.* (CLAS Collaboration), *Observation of an exotic baryon with S = +1 in photoproduction from the proton*, Phys. Rev. Lett. **92**, 032001 (2004), hep-ex/0311046.

[65] D. Barna *et al.* (NA49 Collaboration), *Search for the Θ^+ pentaquark in the NA49 experiment in p+p collisions*, NA49 Note **294** (2003).

[66] M. Oka, *Theoretical overview of the pentaquark baryons*, Prog. Theor. Phys. **112**, 1 (2004), hep-ph/0406211.

[67] S. Capstick, P. R. Page, and W. Roberts, *Interpretation of the Θ^+ as an isotensor resonance with weakly decaying partners*, Phys. Lett. **B570**, 185 (2003), hep-ph/0307019.

[68] J. Adams *et al.* (STAR Collaboration), *Identified particle distributions in p+p and Au+Au collisions at* $\sqrt{s_{\rm NN}} = 200$ *GeV*, Phys. Rev. Lett. **92**, 112301 (2004), nucl-ex/0310004.

[69] L. Gaudichet (STAR Collaboration), $\Lambda(1520)$ *and* $\Sigma(1385)$ *resonance production in Au+Au and p+p collisions at RHIC (*$\sqrt{s_{\rm NN}} = 200$ *GeV)*, J. Phys. **G30**, S549 (2004), nucl-ex/0307013.

[70] C. Markert (STAR Collaboration), *Resonance production in STAR*, Heavy Ion Phys. **21**, 171 (2004), nucl-ex/0308029.

[71] S. Salur (STAR Collaboration), *Pentaquark search in relativistic heavy ion collisions with STAR*, (2004), nucl-ex/0403009.

[72] M. Bourquin and J. M. Gaillard, *A simple phenomenological description of hadron production*, Nucl. Phys. **B114**, 334 (1976).

[73] J. Adams *et al.* (STAR Collaboration), *Multi-strange baryon production in Au Au collisions at* $\sqrt{s_{\rm NN}}$*=130 GeV*, Phys. Rev. Lett. **92**, 182301 (2004), nucl-ex/0307024.

[74] T. Sjostrand, L. Lonnblad, S. Mrenna, and P. Skands, *PYTHIA 6.3: Physics and manual*, (2003), hep-ph/0308153.

[75] M. T. Heinz, *Strange and multi-strange particle production in* $p + p$ *collisions at* $\sqrt{s_{\rm NN}} = 200$ *GeV in STAR*, (2005), nucl-ex/0505025.

[76] S. Wheaton and J. Cleymans, *THERMUS, A thermal model package for ROOT*, (2004), hep-ph/0407174.

[77] C. Markert, *Private Communications.*

[78] M. Bleicher, *Probing hadronization and freeze-out with multiple strange hadrons and strange resonances*, Nucl. Phys. **A715**, 85 (2003), hep-ph/0212378.

[79] J. Adams *et al.* (STAR Collaboration), *Pion interferometry in Au + Au collisions at* $\sqrt{s_{\rm NN}} = 200$ *GeV*, Phys. Rev. **C71**, 044906 (2005), nucl-ex/0411036.

[80] C.-Y. Wong, *Introduction to High-Energy Heavy-Ion Collisions* (World Scientific, 1994).

Index